ILLINOIS CENTER FOR TRANSPORTATION

CIVIL ENGINEERING STUDIES
Illinois Center for Transportation Series No. 21-010
UILU-ENG-2021-2010
ISSN: 0197-9191

Truck Platooning on Flexible Pavements in Illinois

Prepared By
Imad L. Al-Qadi
Egemen Okte
Aravind Ramakrishnan
Qingwen Zhou
Watheq Sayeh
University of Illinois at Urbana-Champaign

Research Report No. FHWA-ICT-21-010

A report of the findings of

ICT PROJECT R27-203
Truck Platooning on Illinois Pavements

https://doi.org/10.36501/0197-9191/21-010

Illinois Center for Transportation

May 2021

TECHNICAL REPORT DOCUMENTATION PAGE

1. Report No.	2. Government Accession No.	3. Recipient's Catalog No.
FHWA-ICT-21-010	N/A	N/A

4. Title and Subtitle	5. Report Date
Truck Platooning on Flexible Pavements in Illinois	May 2021
	6. Performing Organization Code N/A

7. Authors	8. Performing Organization Report No.
Imad L. Al-Qadi (https://orcid.org/0000-0002-5824-103X), Egemen Okte, Aravind Ramakrishnan, Qingwen Zhou, Watheq Sayeh	ICT-21-010 UILU-2021-2010

9. Performing Organization Name and Address	10. Work Unit No.
Illinois Center for Transportation Department of Civil and Environmental Engineering University of Illinois at Urbana-Champaign 205 North Mathews Avenue, MC-250 Urbana, IL 61801	N/A
	11. Contract or Grant No. R27-203

12. Sponsoring Agency Name and Address	13. Type of Report and Period Covered
Illinois Department of Transportation (SPR) Bureau of Research 126 East Ash Street Springfield, IL 62704	Final Report 6/1/19–5/31/21
	14. Sponsoring Agency Code

15. Supplementary Notes

Conducted in cooperation with the U.S. Department of Transportation, Federal Highway Administration.

https://doi.org/10.36501/0197-9191/21-010

16. Abstract

Truck platoons have many benefits over traditional truck mobility. Truck platoons have the potential to improve safety and reduce fuel consumption between 5% and 15%, based on platoon configuration. In Illinois, trucks carry more than 50% of freight tonnage and constitute 25% of the traffic on interstates. Therefore, expected fuel savings would be significant for trucks. Deployment of truck platoons within interstate highways may have a direct effect on flexible pavement performance, as the time between consecutive axle loads (i.e., resting time) is expected to decrease significantly. Moreover, platoons could potentially accelerate pavement damage accumulation due to trucks' channelized position, decreasing pavement service life and increasing maintenance and rehabilitation costs. The main objective of this project was to quantify the effects of truck platoons on pavements and to provide guidelines to control corresponding potential pavement damage. Finite-element models were utilized to quantify the impact of rest period on pavement damage. Recovered and accumulated strains were predicted by fitting exponential functions to the calculated strain profiles. The results suggested that strain accumulation was negligible at a truck spacing greater that 10 ft. A new methodology to control pavement damage due to truck platoons was introduced. The method optimizes trucks' lateral positions on the pavements, and an increase in pavement service life could be achieved if all platoons follow this optimization method. Life cycle assessment and life cycle cost analysis were conducted for fully autonomous, human-driven, and mixed-traffic regimes. For example, for an analysis period of 45 years, channelized truck platoons could save life cycle costs and environmental impacts by 28% and 21% compared with human-driven trucks, respectively. Furthermore, optimum truck platoon configuration could reduce life cycle costs and environmental impacts by 48% and 36%, respectively, compared with human-driven trucks. In contrast, channelized traffic could increase pavement roughness, increasing fuel consumption by 15%, even though platooning vehicles still benefit from reduction in air drag forces. Given that truck platoons are expected to be connected only in the first phase, no actions are required by the agency. However, in the second phase when truck platoons are also expected to be autonomous, a protocol for driving trends should be established per the recommendation of this study.

17. Key Words	18. Distribution Statement
Truck Platooning, Platoons, Platoonable Segments, Resting Period, Fuel Consumption, Pavement Damage, Life Cycle Cost, Global Warming	No restrictions. This document is available through the National Technical Information Service, Springfield, VA 22161.

19. Security Classif. (of this report)	20. Security Classif. (of this page)	21. No. of Pages	22. Price
Unclassified	Unclassified	73 + appendix	N/A

ACKNOWLEDGMENT, DISCLAIMER, MANUFACTURERS' NAMES

This publication is based on the results of **ICT-R27-203: Truck Platooning on Illinois Pavements**. ICT-R27-203 was conducted in cooperation with the Illinois Center for Transportation; the Illinois Department of Transportation; and the U.S. Department of Transportation, Federal Highway Administration.

Members of the Technical Review Panel (TRP) were the following:

- Brian Hill, TRP Co-chair, Illinois Department of Transportation
- Charles Wienrank, TRP Co-chair, Illinois Department of Transportation
- Dennis Bachman, Federal Highway Administration
- Autumn Bizon, Freight Management Inc.
- Linda Blisset, Illinois Trucking Association
- Kevin Burke, Illinois Asphalt Pavement Association
- Anabelle Huff, Illinois Department of Transportation
- Geno Koehler, Illinois Department of Transportation
- LaDonna Rowden, Illinois Department of Transportation
- Laura Shanley, Illinois Department of Transportation
- Megan Swanson, Illinois Department of Transportation

The contents of this report reflect the view of the authors, who are responsible for the facts and the accuracy of the data presented herein. The contents do not necessarily reflect the official views or policies of the Illinois Center for Transportation, the Illinois Department of Transportation, or the Federal Highway Administration. This report does not constitute a standard, specification, or regulation.

TABLE OF CONTENTS

LIST OF FIGURES

LIST OF TABLES

CHAPTER 1: INTRODUCTION

INTRODUCTION

Most of the United States' freight, $38.5 billion of cargo, is carried daily on US roads, making up 66% of the total goods carried (Bureau of Transportation Statistics, 2020). This number is projected to increase to 51.5 million tons by 2040. Because trucks are the heaviest vehicle type used on pavements, they are the most damaging to the roads. To keep up with the mobility demand by people and goods, transportation officials continuously invest in transportation infrastructure. In 2018, the federal government invested $110 billion in nondefense physical capital. Nearly three-fifths of that amount, or $64 billion, was for transportation, 92% of which was granted to local and state governments (Campbell, 2018). The State of Illinois allocated $11.5 billion for their highway infrastructure between the years 2019–2024, 33% of which is needed for routine maintenance of road networks (IDOT, 2018).

Currently, the number of trucks on the road are primarily controlled by the number of truck drivers. There is a deficit of nearly 61,000 truck drivers in the United States as of 2019 (Costello & Suarez, 2019). However, with the advent of connected and autonomous vehicles (CAVs), this shortage could be addressed in spite of the increasing demands on trucks. Connected and autonomous trucks (CATs) are expected to penetrate the market in 2022 with an increasing level of autonomy each of the following years (Chottani et al., 2018).

In addition to the increase in number, CAVs present additional opportunities for pavement structures. CATs could form platoons to save fuel by reducing their air drag. McAuliffe et al. (2018) showed that platoons would reduce fuel consumption by 5%–15%. The two most important parameters that control platoon fuel savings are truck spacing and relative position on a lane (Zhang et al., 2020). Both parameters are important in pavement design. Truck spacing affects the response of flexible pavements (Zeiada et al., 2018), whereas the trucks' relative position affects channelization of traffic (Siddharthan et al., 2017). When planning CATs, both parameters should be considered in pavement design and distress prediction as well as the subsequent user fees.

OBJECTIVES

As truck platooning is transitioning from a concept to reality, transportation agencies should prepare by being well informed about the effects of truck platoons on pavements. Therefore, the main objective of this study was to quantify the effects of CAT platoons on flexible pavements (rigid and composite pavements were not considered) and to develop recommendations on the trade-off between CAT platoon fuel consumption and accelerated pavement damage. To meet this objective, several tasks were performed. The tasks were completed in the following order:

1. Determine platoonable sections of Illinois truck routes and extract their section geometries.
2. Determine the safe, minimum truck spacing by considering flexible pavement damage and traffic congestion.

3. Determine flexible pavement damage as a function of trucks' lateral positions, spacing, and number of trucks in a platoon.

4. Determine the optimum platoon design to minimize fuel consumption and damage.

5. Determine the impact of platoons on environment and costs using life cycle assessment and life cycle cost analysis, respectively.

The first part of this study (Al-Qadi et al., 2021) focused on the determination of Illinois' platoonable sections, while the second part of the study, reported herein, focused on the remaining tasks provided above. Traffic safety considerations were not specifically included in this research study.

IMPACT OF TRUCK PLATOONS ON PAVEMENT PERFORMANCE

Platooning allows CATs to follow each other at a much closer distance compared to human-driven trucks. Moreover, vehicles wander less because of CATs' precise lane-keeping technology. The truck's close spacing changes the rest period between axle-load applications, where lateral position changes the channelization of traffic. A detailed description of these phenomena on pavement damage are provided in the first part of the study (Al-Qadi et al., 2021). A summary is provided below.

Impact of Rest Period on Pavement Performance

The rest period between trucks affects flexible pavement responses. If the response is non-recoverable, the flexible pavement may develop distresses such as fatigue cracking and permanent deformation (rutting). In the case of fatigue cracking, asphalt concrete (hot-mix asphalt [HMA]) can self-heal microcracks when no load is present. It also exhibits viscoelastic recovery in between load applications. Shen et al. (2013) showed that while healing occurs in a matter of hours, viscoelastic recovery may happen in a matter of seconds. However, both are important factors when considering pavement fatigue behavior. Laboratory test results showed that introducing a rest period to HMA samples could increase both fatigue life and HMA modulus (Daniel et al., 2001). Beranek and Carpenter (2009) developed a logarithmic relationship between rest period and number of repetitions to failure using laboratory test results. However, the test results were generalized to field conditions using mechanistic models or laboratory-to-field correlations.

Similarly, for rutting, researchers looked at the impact of various loading patterns (load period to rest period ratio). Increasing the rest period reduced HMA permanent deformation (Nejad et al., 2016; Motevalizadeh et al., 2018). However, during the development of a stress sweep permanent deformation test, Kim and Kim (2017) found that decreasing rest period past a certain threshold would reduce permanent deformation. They theorized that this behavior could be due to HMA hardening and concluded that the relationship between permanent deformation and rest period was more complicated than initially hypothesized.

In addition, the impact of rest period on pavement performance is coupled by the shape of load pulses. To understand this coupled relationship, Underwood and Zeiada (2014) compared block-rest and pulse-rest loading patterns and found that even when the magnitudes of the loads were similar, the shape of the loading pulse had a significant impact on HMA response. Because CAV loading

patterns are different than lab-designed loading patterns, correlations between lab and field measurements may vary significantly depending on the type of lab test. Currently, there is no pavement design framework that considers the impact of rest period or the shape of the loading pulse. To consider complex loading patterns, finite-element (FE) models should be utilized in conjunction with laboratory data in lieu of the currently used layered elastic pavement response method.

Impact of Lateral Position on Pavement Performance

Pavement responses and damage are known to be affected by channelized traffic. Using Virginia Smart Road data, Al-Qadi and Nassar (2003) investigated pavement responses under various factors such as stress state, material, healing, and wander. Assuming a normal traffic distribution, they developed a shift factor for vehicle wander. Later, Wu and Harvey (2008) subjected pavement sections to channelized and non-channelized traffic using a heavy vehicle simulator at 6 mph. They found that by varying the wheel position at a range of 15 in, they could reduce the permanent deformation by one-quarter after 3,000 load repetitions. These results were later confirmed by Zhou et al. (2018), who looked at the impact of CAVs on hydroplaning and pavement performance using the Texas Mechanistic-Empirical Flexible Design System (Zhou et al., 2019). They found that without wander, CAVs can increase rut depth by 30% and decrease fatigue life by 20%.

Currently, there are a few methodologies that incorporate vehicle wander in pavement design. For fatigue, AASHTOWare Pavement ME Design (PMED) distributes traffic equally onto five lateral positions, which are selected based on the mean and standard deviation of wheel wander. A second methodology considers traffic as a distribution and uses Monte Carlo simulation to compute a cumulative distribution function (CDF) for pavement responses (Siddharthan et al., 2017). The CDF is divided into five equal segments. Using PMED transfer functions, the damage is computed utilizing the average of CDF responses. Finally, Wander 2D is another custom approach that uses the lateral positions of the trucks as an explicit input in PMED to compute pavement damage accumulation (Gungor et al., 2020, Al-Qadi et al., 2020). Wander 2D uses curve fitting to consider pavement damage as a continuous function and then utilizes Chebyshev polynomials to approximate the complex damage functions.

CHAPTER 2: IMPACT OF REST PERIOD ON PAVEMENT PERFORMANCE

Currently, many pavements in the United States are designed based on the AASHTOWare PMED computer program, which utilizes linear elastic theory for modelling the pavements. In PMED, pavement responses are the main component of the design framework and are used in transfer functions to predict pavement distresses. One of the important factors that affect pavement responses is loading. Traffic loading is comprised of different patterns of loading times, axle loading configurations, and resting periods. Therefore, pavement should be modelled as a combination of various pulses with different loading times and resting periods to simulate traffic composition. *Rest period* is defined as the interval between the applications of two consecutive loads. Each loading cycle contains loading time and resting time before the application of another loading cycle. In the context of platooning, rest period is the time interval between the load application of the front truck's rear axle and the following truck's steering axle.

The studies mentioned in the first phase of this study (Al-Qadi et al., 2021) highlighted the influence of loading time and rest period duration through a small-domain experimental setup to understand the behavior of HMA material. To the best of the authors' knowledge, only one study had attempted to simulate actual field loading in an experimental procedure (Mansourkhaki et al., 2014). Therefore, the implication of realistic traffic loading (including rest period and loading time) on a pavement warrants a full structural analysis. Hence, a 3D FE pavement model that simulates closer to actual conditions can be utilized.

EFFECT OF TANDEM AXLE

The rear (tandem) and steering (single) axles need to be modeled to understand the effect of rest period on pavement performance. However, to understand strain accumulation and recovery as compared to that of a single axle, the influence of tandem-axle configuration on HMA pavement responses needs to be analyzed. For a viscoelastic material, strain accumulation and recovery are critical to computing damage such as number of cycles to fatigue cracking failure and rutting. The outcome would provide insight regarding the truck platoon design speed and spacing that cause channelized traffic and utilize relatively small spacing between trucks.

Three-dimensional Pavement Model

The existing PMED pavement model has several shortcomings: (i) pavement is modelled as being linear elastic axisymmetric; (ii) uniform static loading over a circular contact area is applied; and (iii) simplified layer interactions, using distributed springs, are assumed. For this study, the 3D FE pavement model developed over the past two decades by Al-Qadi and coworkers was used to overcome the PMED shortcomings discussed previously (Al-Qadi & Yoo, 2007; Elseifit et al., 2006; Hernandez et al., 2016; Yoo & Al-Qadi, 2007; Yoo et al., 2006).

In this study, a model was developed to simulate appropriate material behavior in conjunction with loading conditions in the field. Hot-mix asphalt is a viscoelastic (VE) material; hence, its properties are

functions of loading time and temperature. If the HMA layer is thin (less than 4 in), then the granular base is taken as a stress-hardening material, while the subgrade is taken as a stress-softening material. The actual tire loading is applied through nonuniform 3D contact stresses on the pavement model.

In addition to the above considerations, the mesh of an FE model is usually optimized such that, with a minimum number of elements, accurate results could be obtained. Overall, the 3D FE model developed was proven to be effective in incorporating complex properties like material behavior and nonuniform tire loading considered herein. However, a few improvements could be implemented to address the following: (i) one loading cycle is typically used in the analysis (attempts were made to overcome the computationally expensive approach by Yoo and Al-Qadi [2007]); and (ii) no damage mechanisms are included (cracking, healing, or permanent deformation). In addition, half-axle loading is usually considered, either as a single wide-based tire (WBT) or a dual-tire assembly (DTA); hence, no potential interaction between two consecutive loads is considered.

Building upon the existing model, a tandem-axle configuration was employed in this study to analyze the influence of spacing or rest period on pavement responses. The loading scenario corresponded to the class 9 vehicle type, per Federal Highway Administration (FHWA) guidelines. A class 9 vehicle is a five-axle, single-trailer truck commonly used in transporting goods within the US highway network. The five axles include the steering axle (underneath the driving cab) and trailer axles. Figure 1 presents the full tandem-axle FE model; only half of an axle is modeled. The axle spacing is 4.5 ft—the general spacing for a class 9 truck, based on FHWA guidelines. The length of the wheel path of the model should be at least twice the axle spacing so that maximum responses can be captured.

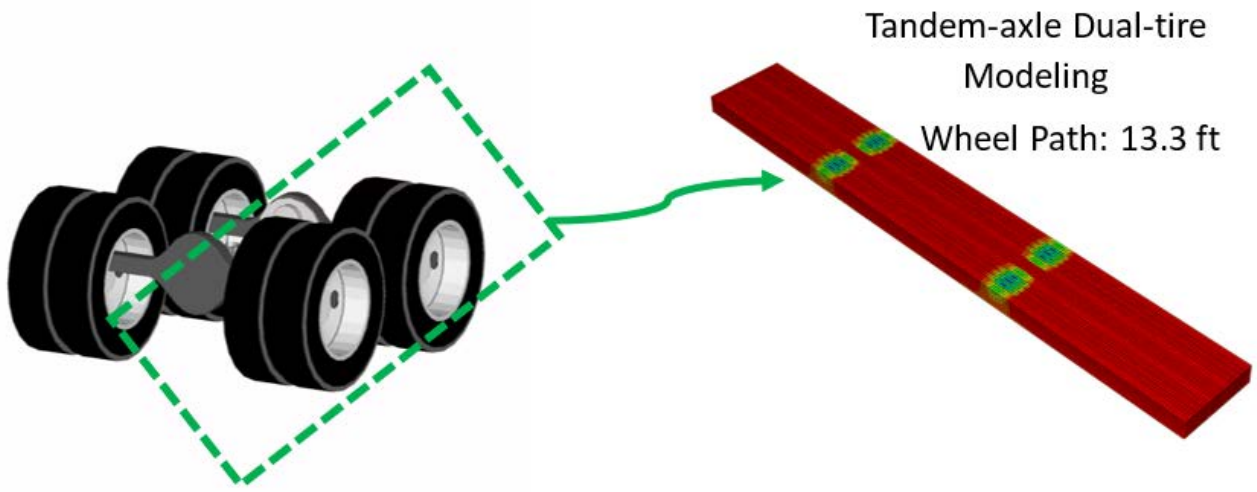

Figure 1. Illustration. FE model of a tandem-axle dual tire assembly.

Simulation Matrix

A full-pavement model requires inputs such as structure information (layer thickness and temperature), material parameters, and loading configuration (type of tire, load level, speed of

loading, and spacing). Running a full-pavement model with its complex considerations is computationally intensive and time-consuming. Therefore, it is important to select the critical factors relevant to the objective of the study. Hence, the combined effect of speed and temperature for a given spacing (4.5 ft) on pavement responses was studied. In addition, as HMA layers undergo a certain level of recovery after each load application, the shorter the rest period, the higher the rate at which damage may accumulate.

Given the VE nature of the HMA layers, loading time is critical with respect to the structural response and rest period. Two traveling speeds were considered for the truck axle configurations, representing the free flow operating conditions for interstates and thin sections (i.e., 40 mph and 70 mph). Temperature is a critical parameter that drives the behavior of VE HMA layers. As the temperature increases, the material's stiffness decreases, resulting in greater responses. Therefore, a nonlinear temperature profile along the HMA layer was utilized to account for the environmental condition as loads traverse the pavement. The nonlinear temperature profile is shown in Figure 2. Three temperature profiles were used with pavement surface temperatures of 122°F, 68°F, and 18°F to account for seasonal weather variations.

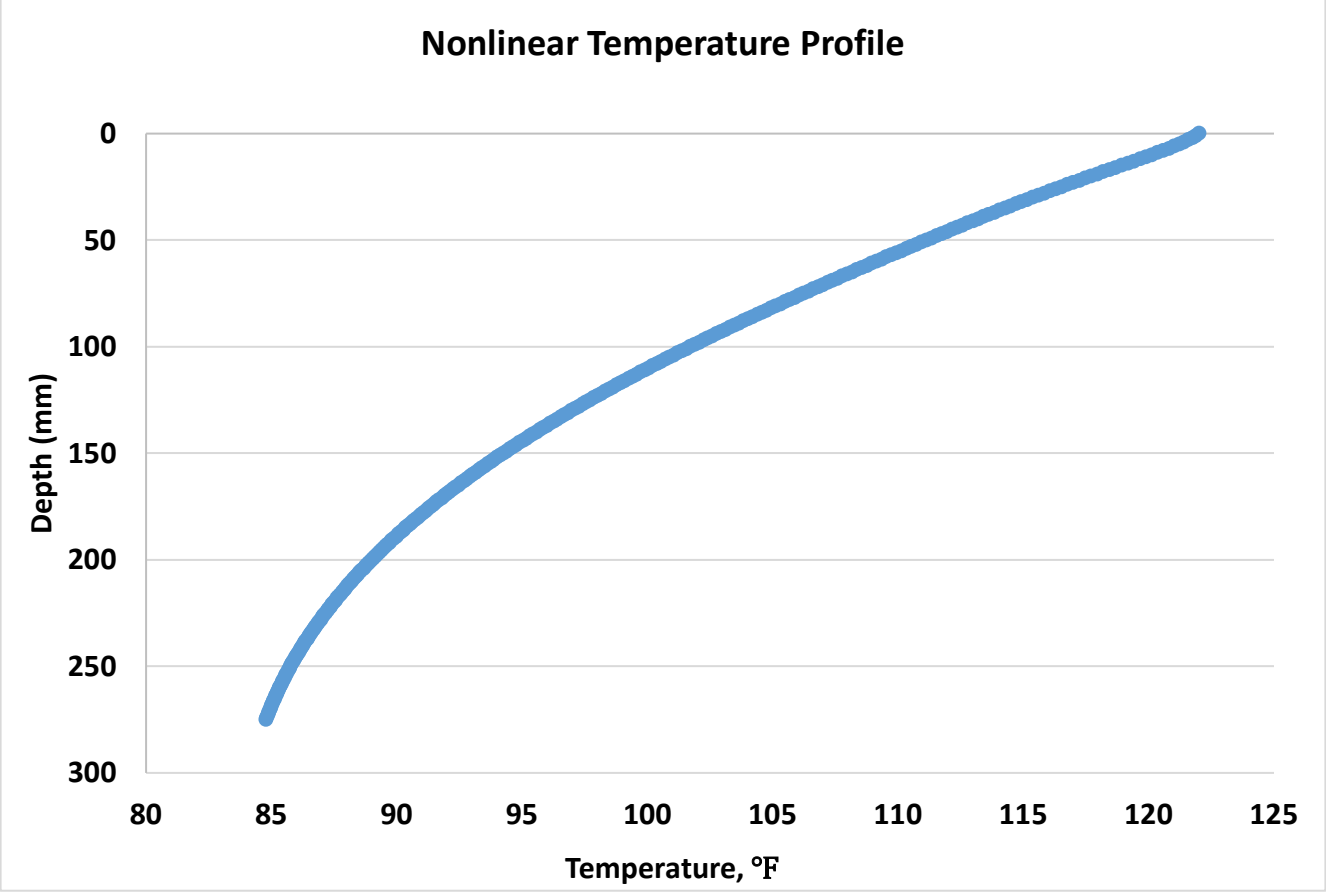

Figure 2. Plot. Nonlinear temperature profile for 122°F.

In addition to tandem-axle interaction, a single axle was also run using the same pavement model inputs. Single-axle cases would simulate the following truck's steering axle. As stated previously, FE models are computationally intensive and time-consuming. For calculation efficiency, a set of 180 cases were run initially for a single axle to create the database presented in Table 1.

Table 1. Simulation Matrix for Single and Tandem Axles

Type	Single Axle	Tandem Axle
Layer Material Type	Strong and Weak	Strong and Weak
Structure	Thick (11 in HMA, 70 mph) and Thin (4 in HMA, 40 mph)	Thick (11 in HMA, 70 mph) and Thin (4 in HMA, 40 mph)
Tire Type	DTA, WBT, and Steering	DTA and WBT
Temperature (°F)	122, 68, and 18 profiles	122, 68, and 18 profiles
Half-axle Load (kips)	6.75, 9, 11.25, 13.5, and 15.75	16.875
Total Number of Cases	**2×2×3×3×5 = 180 cases**	**2×2×2×3 = 24 cases**

Strong and weak material properties were obtained from FHWA's Long-Term Pavement Performance (LTPP) program, a nationwide database collected over the past 30 years. Using a statistical analysis and a typical HMA layer's nominal maximum aggregate size, six dynamic modulus curves were obtained from 1,000 available curves, presented in Figure 3. The approach of selecting the dynamic modulus curves is described by Hernandez et al. (2016). The thick section contains three HMA layers: the wearing surface (WS), an intermediate layer (IS), and a base layer (BS). Strong and weak represents the material modulus value at all times. Two pavement structures—thick and thin—were used at tire load speeds of 70 mph and 40 mph, respectively. In general, interstate sections are thick, and a maximum speed of 70 mph is allowed. For thin sections, the maximum speed limit is around 40 mph, although 70 mph is sometimes the limit. Finally, five loadings (6.75 to 15.75 kips) were applied to obtain the responses as a function of loading. Using the responses from FHWA's LTPP program, functions were developed in terms of loading. Therefore, any new given loading function could be used to obtain the responses without running a FE pavement model.

Tandem-axle FE models are much larger than single-axle models and, hence, are computationally intensive and time-consuming. Therefore, the maximum axle weight limit was selected. The tandem-axle weight limit cannot exceed 34 kips because of weight-limit restrictions imposed by state agencies to reduce damage. A total of 24 tandem-axle cases were generated and post-processed.

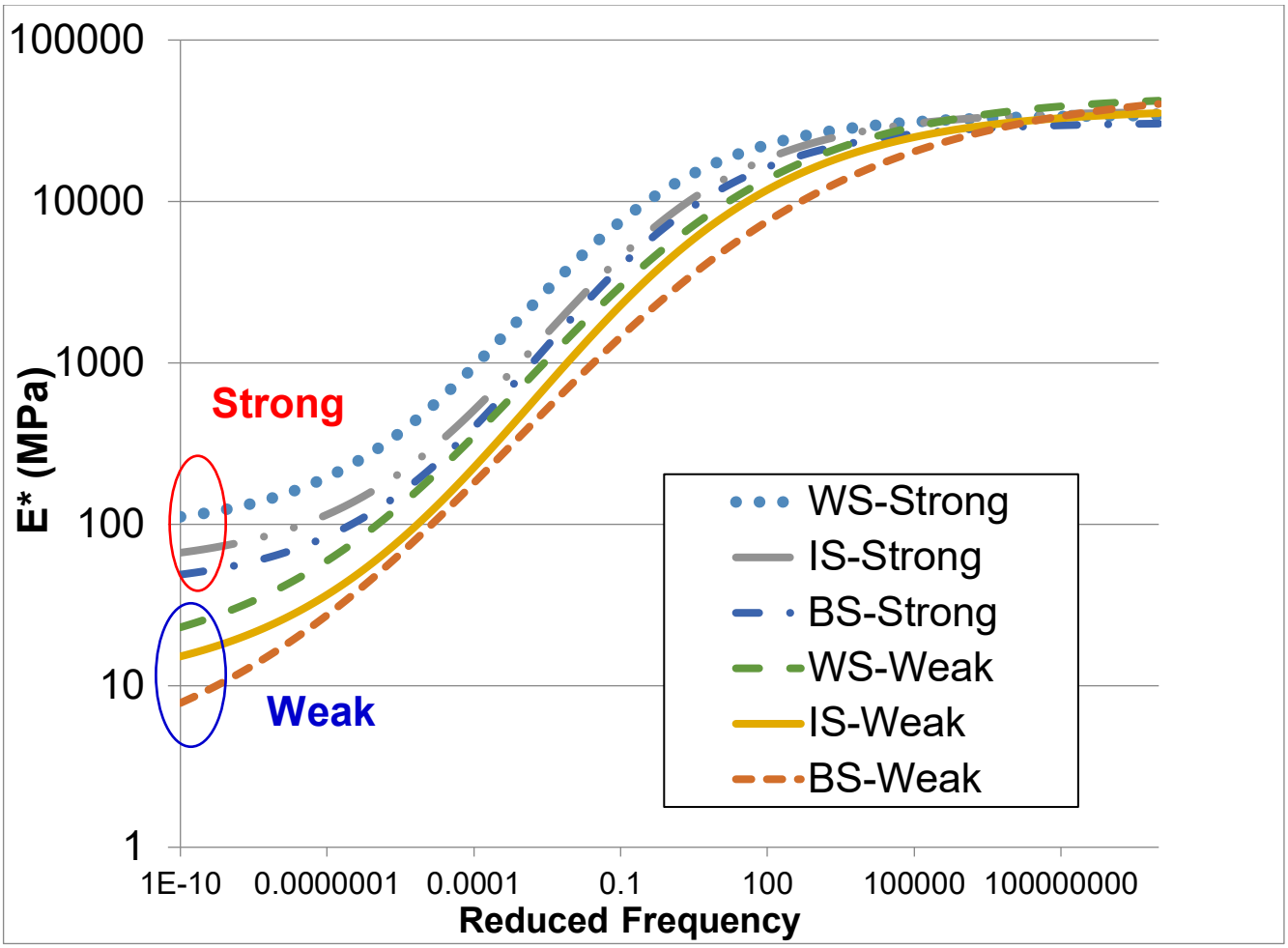

Figure 3. Plot. Strong and weak materials for hot-mix asphalt.

Source: Hernandez et al. (2016)

Post-processing

In this chapter, the following terms are used—X (along the direction of traffic), Y (through the depth), and Z (along the transverse) directions—corresponding to subscript notations 1, 2, and 3, respectively. Post-processing was carried out by taking elements in a rectangular transverse cross-section (YZ plane) in the center of the model for each layer. The responses for all elements in the section were collected as the tire moved along the model, as presented in Figure 4. Post-processing for all elements in a cross-section is more accurate than having a fixed path along the center of the tire and collecting the responses over time. For certain critical responses, the maximum usually occurs near or below the edge of the tire. Even in the case of a linear elastic analysis of pavements, some maximum responses occurred below the edge of a tire. Because the FE model is infinite, theoretically, responses across any transverse cross-section should be the same for any given loading.

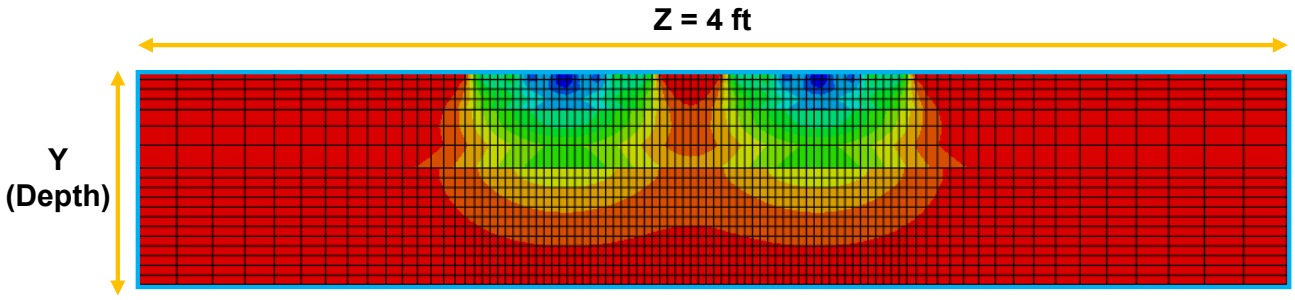

Figure 4. Illustration. Cross-sectional view of elements for post-processing.

IMPACT ON PAVEMENT DAMAGE

Gungor et al. (2019) quantified the impact of lateral position on pavement damage. The effect of rest period on pavement responses is presented below. Eventually, the responses were used in a framework based on transfer functions to compute the predicted fatigue cracking and rutting, which are the major distresses in pavement. The influence of rest period on the critical distresses are presented below. The results for a thick section (70 mph), dual-tire assembly, intermediate temperature, and strong HMA material are discussed.

Effect of Rest Period on Predicted Fatigue Cracking

Fatigue cracking typically occurs because of the presence of tensile strains. The maximum horizontal tensile strains, longitudinal and transverse (ε_{11} and ε_{33}), were collected at the surface and bottom of the HMA layer, respectively. These strains correspond to near-surface and bottom-up fatigue cracking, respectively. Two peaks in Figure 5-A represent the tandem axle. Axle interaction can be observed for the transverse strain, where strain decreases slowly for the region between the two peaks. For the longitudinal strain, most of the strain is recovered. After application of the first load, the transverse strain recovered slower than the longitudinal strain. In contrast, for a single axle (Figure 5-B), recovery of the longitudinal strain is quicker than for the transverse strain. A similar effect is observed for the tandem axle, which makes the impact greater on the predicted transverse strain. The generally slower recovery of the transverse strain, compared to the longitudinal strain, suggests that the former should be considered as the critical parameter for pavement design and analysis in this case. Earlier studies have reported that either strain could be larger, based on pavement structure and materials, as well as loading conditions (Al-Qadi et al., 2004; Garcia & Thompson, 2008), while recovery time has always been reported as larger for the transverse strain. In a study conducted by Garcia and Thompson (2008), a similar phenomenon based on accelerated pavement testing was observed. The study also mentioned that the transverse strain was about 1.5 times the longitudinal strain.

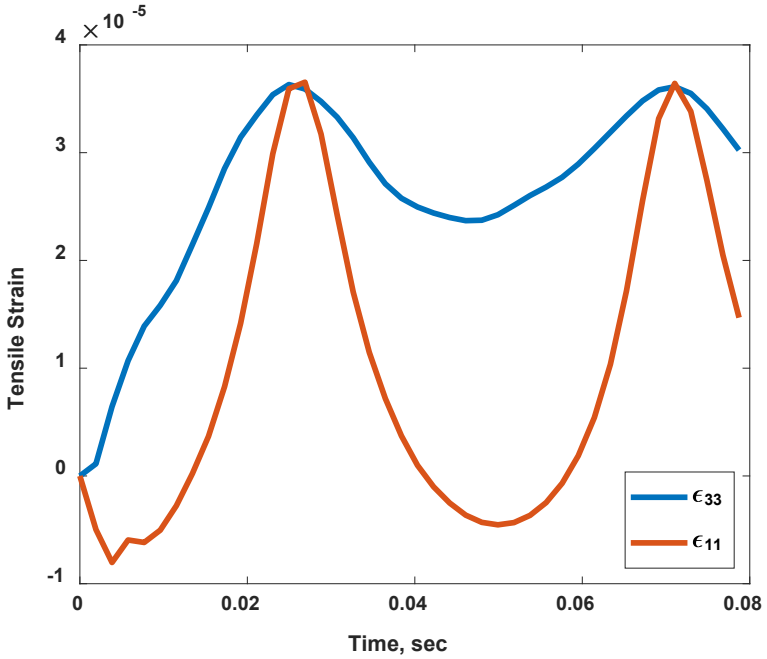

A. Tandem Axle

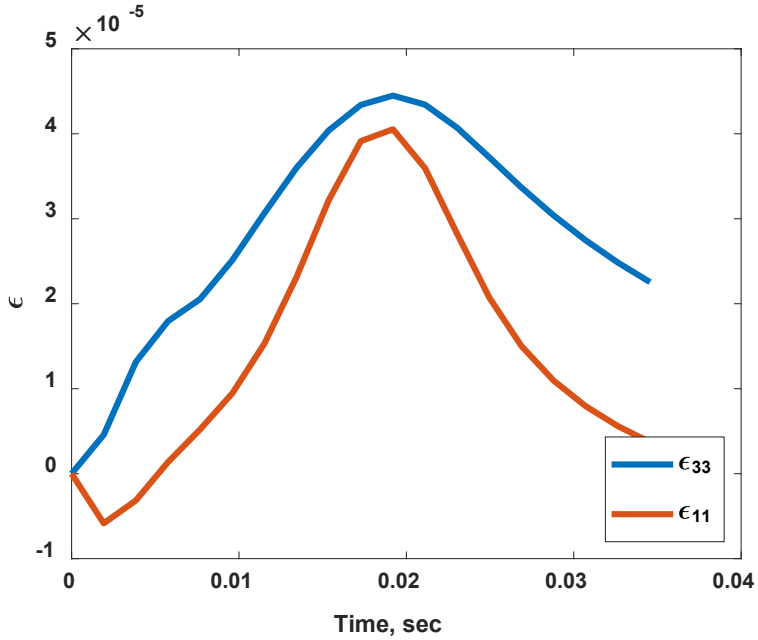

B. Single Axle

Figure 5. Plot. Transverse and longitudinal strains at the bottom of hot-mix asphalt.

As HMA transverse strain can be a critical response, it is important to quantify the percentage of strain recovery after load applications. In the field, traffic-load applications are a combination of axles with different loading magnitudes, contact stresses, axle spacings, speeds, and wander distances. The

focus herein is on the axle spacing. Obtaining the complete time history of a response requires a relatively large FE model, which is computationally intensive. Hence, an exponential function was fitted after the last peak of the strain curve. After application of the tandem axle (rear axle of the front truck), residual strain during application of the single axle (front axle of the following truck) was added to the response of the steering axle. Figure 6-A and Figure 6-B plot the transverse strain recovery of tandem and single axles, respectively.

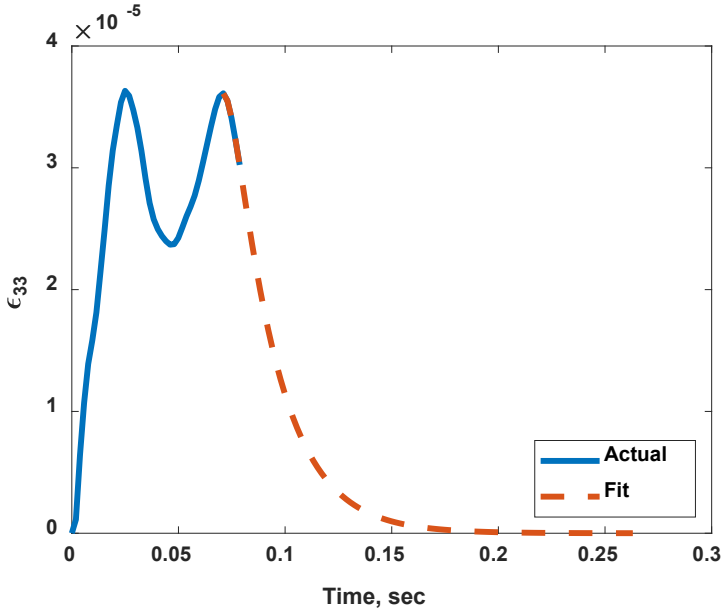

A. Tandem Axle

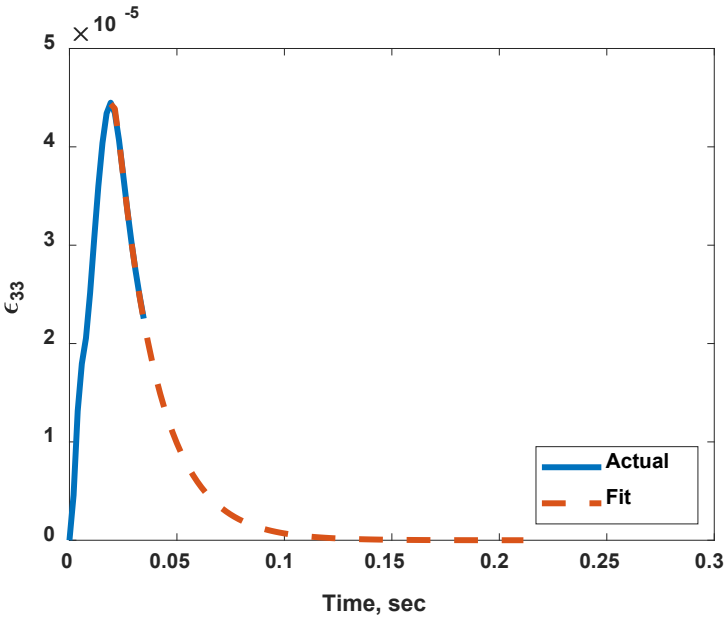

B. Single Axle

Figure 6. Plot. Percentage of transverse strain recovery.

If spacing between two trucks is 10 ft, then the rest period is approximately 0.1 sec. In Figure 6-A, the tandem-axle loading duration nearly took 0.1 sec, and the strain recovered almost fully (~99.9%) after adding rest period. A similar trend is observed for the single axle (Figure 6-B). The effect of rest period on fatigue is only significant if spacing between trucks is less than 5 ft. Practically, 5 ft or lower spacing is not viable because of safety concerns. Note that similar trends were observed for other cases in the database. Based on FE results, it is concluded that rest period did not affect fatigue cracking.

Effect of Rest Period on Predicted Rutting

Vertical compressive strains generally correspond to permanent deformation in the pavement. The maximum vertical compressive strains (ε_{22}) were collected for each sub-layer in the pavement. Strain values for the tandem axle are higher than those for the single axle in all layers. The difference between tandem- and single-axle strain values is greatest for the subgrade, followed by the granular base layer and then the HMA layer. This pattern is expected, as the tandem-loading interaction decreased with depth because of the increased area of loading influence, and ultimately converged into one loading pulse. Figure 7-A and Figure 7-B present vertical compressive strains as a function of time for three layers for tandem and single axles, respectively. The compressive strains recovered almost fully (~96%) for the HMA layer. Similarly, the HMA vertical shear strain recovered almost fully. Ultimately, strains in the unbound two layers returned to zero because both were assumed elastic for thick sections. However, in reality, both layers are stress-dependent materials. Therefore, higher and continued levels of stresses may lead to rutting in the unbound layers.

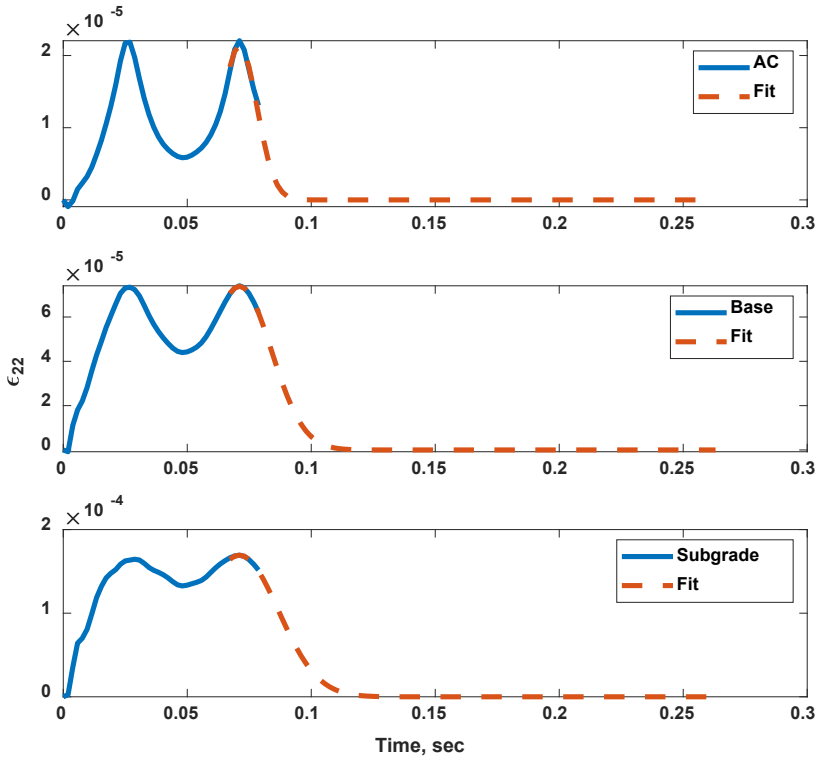

A. Tandem Axle

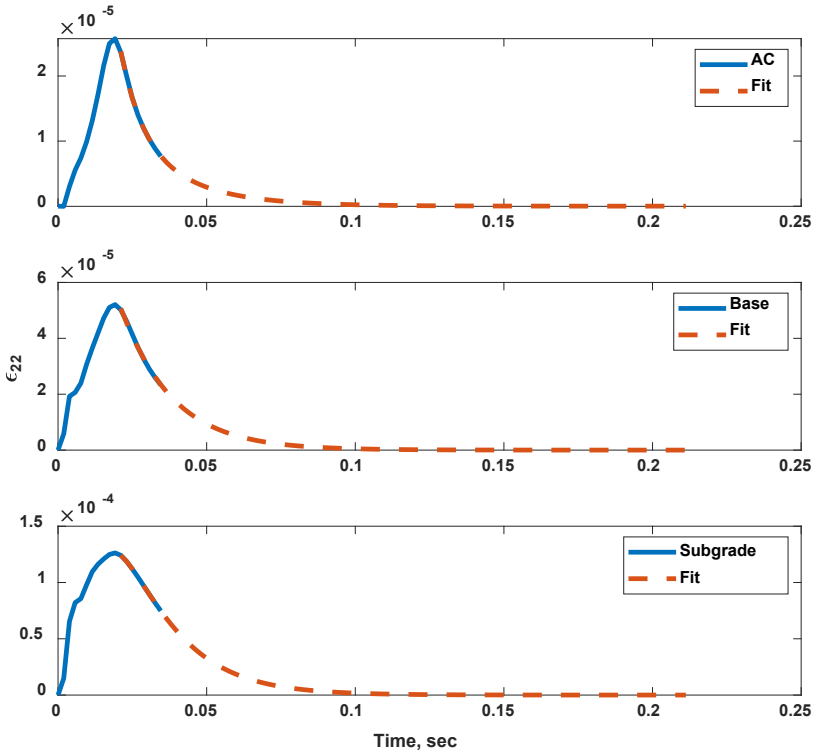

B. Single Axle

Figure 7. Plot. Vertical strain as a function of time.

Similar to fatigue cracking, an exponential family function was fitted to estimate the strain accumulation (or recovery). If there was 10 ft spacing between two trucks, like in the previous scenario, then the strain recovered almost fully (~99.5%) for both single and tandem axles. The influence of rest period on rutting distress is only substantial if spacing between trucks is less than 5 ft. From the results of the 3D FE pavement model, rutting will not be affected by rest period. If shear strain (ϵ_{23}) is used instead of vertical compressive strain (ϵ_{22}), then the rest period does not impact rutting. Similar trends were observed for other cases in the database. The main reason for the trends is the assumption of HMA as a linear viscoelastic material in the model. Therefore, the above results may be different if the HMA is modeled as viscoelastoplastic.

DETERMINATION OF MINIMUM TRUCK SPACING

The magnitude and distribution of axle loading–induced stresses depend on loading condition, axle loading, speed, tire inflation pressure, tire type, and other tire geometry conditions. Effect of distribution and magnitude of stresses on pavement responses and damage were presented in several studies (Romanoschi & Metcalf, 2001; Al-Qadi & Yoo, 2007; Wang & Al-Qadi, 2009). It is important to analyze the effect of different loading conditions for truck platooning, as there could be a potential overlap or accumulation of critical shear stresses in the case of braking, accelerating, and turning conditions. It is assumed that if trucks have a minimum spacing of 200 ft, then there would

not be any accumulation of shear strains between consecutive trucks. This might be significant, as the distance between trucks is expected to be much lower in the platoon. Like braking, turning maneuvers would result in higher transverse strain, and strain accumulation could occur. Figure 8 presents the phenomenon.

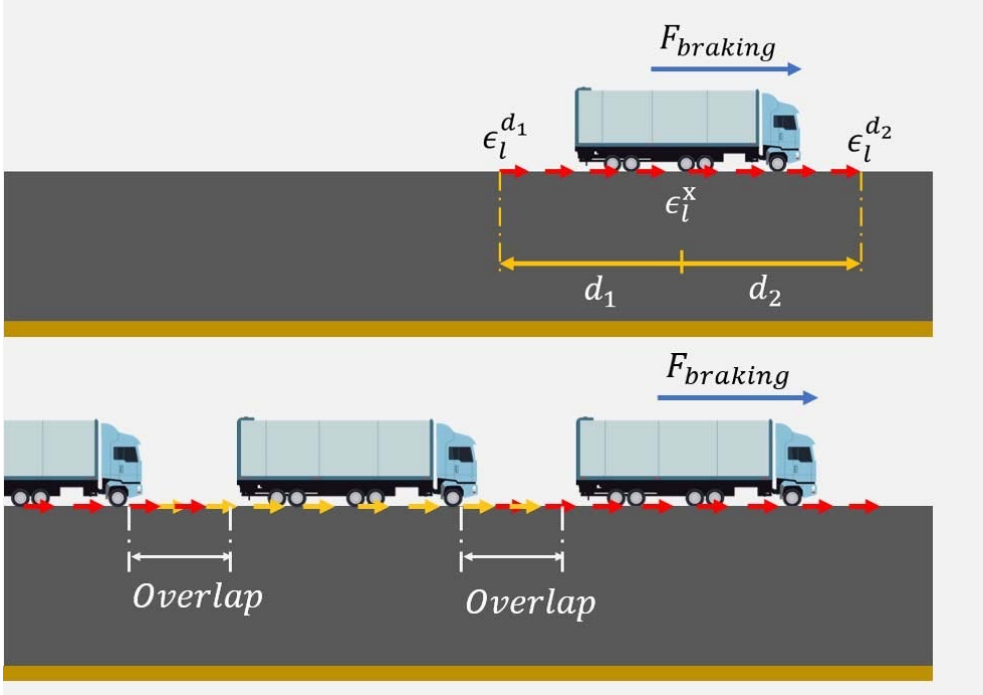

A. Longitudinal Shear Strain Overlap

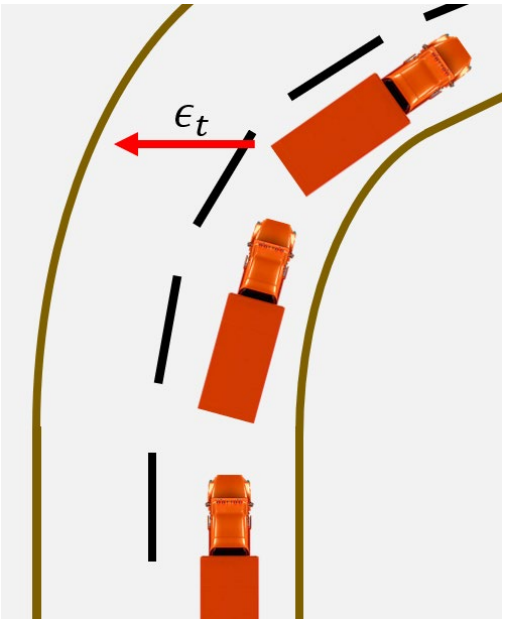

B. Transverse Shear Strain Overlap

Figure 8. Illustration. Strain overlap in longitudinal and transverse directions.

A 3D tire contact stress database was used to analyze the effect of braking and turning loading scenarios. The database was developed using a numerical approach to emulate tires using FE. The FE model was calibrated so that it matched actual contact stress measurements. The developed FE model was then used to obtain contact stresses based on loading condition, tire pressure, speed, and axle load. The details of the model and contact stresses can be found in a report by Hernandez et al. (2016). Table 2 presents the parameters chosen from the database for the analysis.

Table 2. Analysis Parameters

Parameters	Value
Tire Pressure (S3)	110 psi
Axle Loading (P3)	10 kips
Speed (V3)	70 mph
Slip Ratio (Braking, B4)	7%
Slip Angle (Turning, FR6)	6°

The values in Table 2 were selected so that the highest contact stresses were considered (the worst-case scenario). A thick, typical interstate pavement section was used for the analysis. The truck's tandem axle (FHWA, class 9) was modelled with 4.5 ft—the lowest possible spacing—as the axle spacing. A tandem axle was modelled, rather than an entire platoon, because if no significant effect is observed for the lowest possible spacing (4.5 ft), then it can be concluded that it does not affect the entire platoon.

Figure 9 and Figure 10 present the results of the braking and turning scenarios, respectively. Critical pavement strains are plotted as a function of time. For braking and turning conditions, longitudinal and transverse shear strains are critical because of the distribution and magnitude of contact stresses. Two peaks can be observed representing two axles. The influence of nonuniform 3D contact stress is significant near the pavement's surface. Therefore, strains are plotted 2, 4, and 6 inches from the pavement's surface. For the braking scenario, longitudinal and transverse shear strains did not overlap. In other words, there was no accumulation of strain as the magnitudes of the first and second peaks are close. Strains recovered immediately after the load application. There is a slightly delayed recovery at a 6 in depth in the transverse shear strain, but it is not significant enough to accumulate the response. Similar results were observed for the turning loading condition.

Braking and turning scenarios result in different pavement responses than normal loading conditions, but do not lead to significant strain accumulation between axles. As no accumulation was observed for the lowest possible spacing, it does not influence the entire platoon's loading conditions. Hence, the minimum spacing of the platoon is independent of braking and turning loading conditions. Chapter 3 presents the expected strain framework and damage calculation.

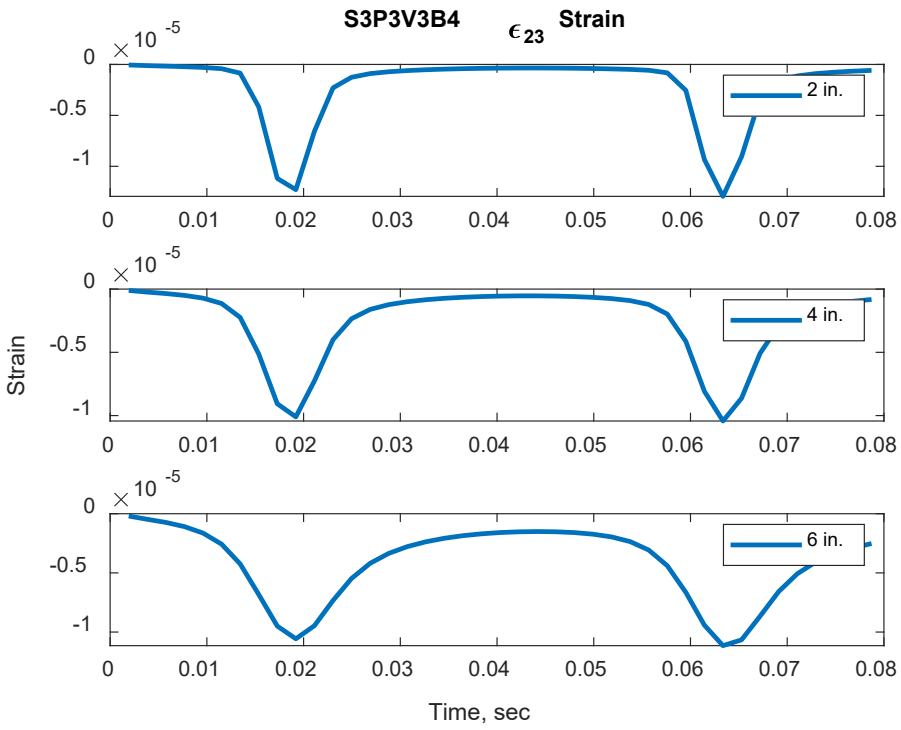

A. Transverse Shear Strain

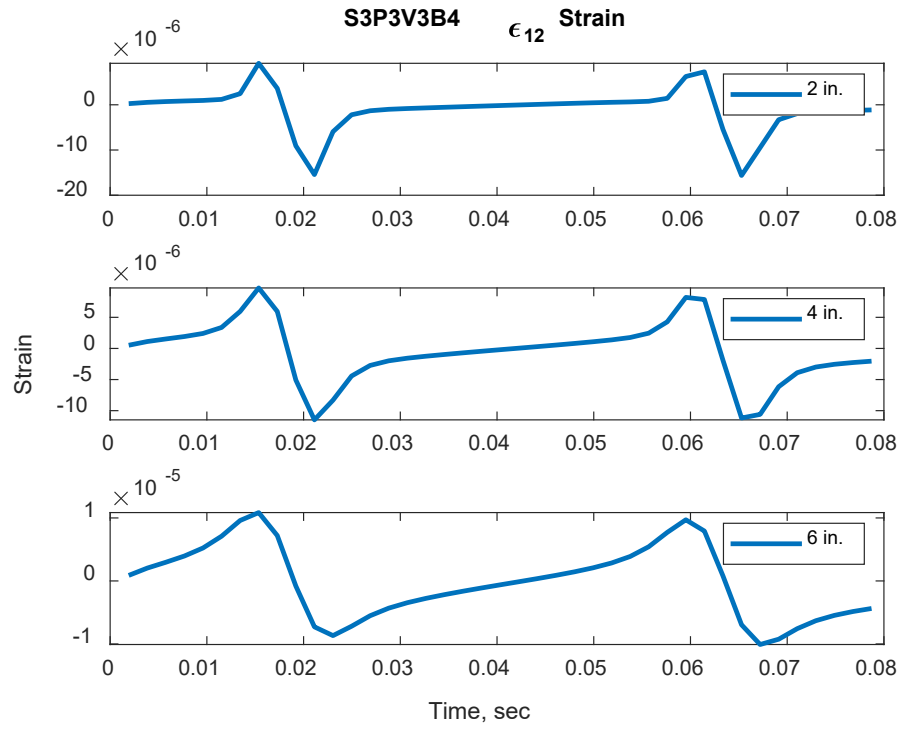

B. Longitudinal Shear Strain

Figure 9. Plot. Braking scenario for (a) transverse and (b) longitudinal shear strains.

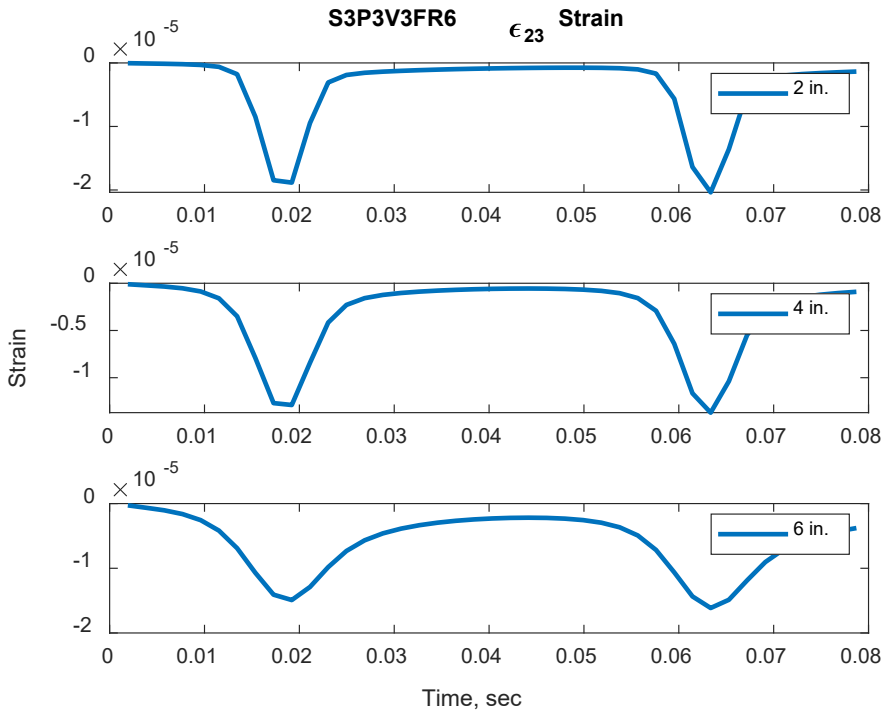

A. Transverse Shear Strain

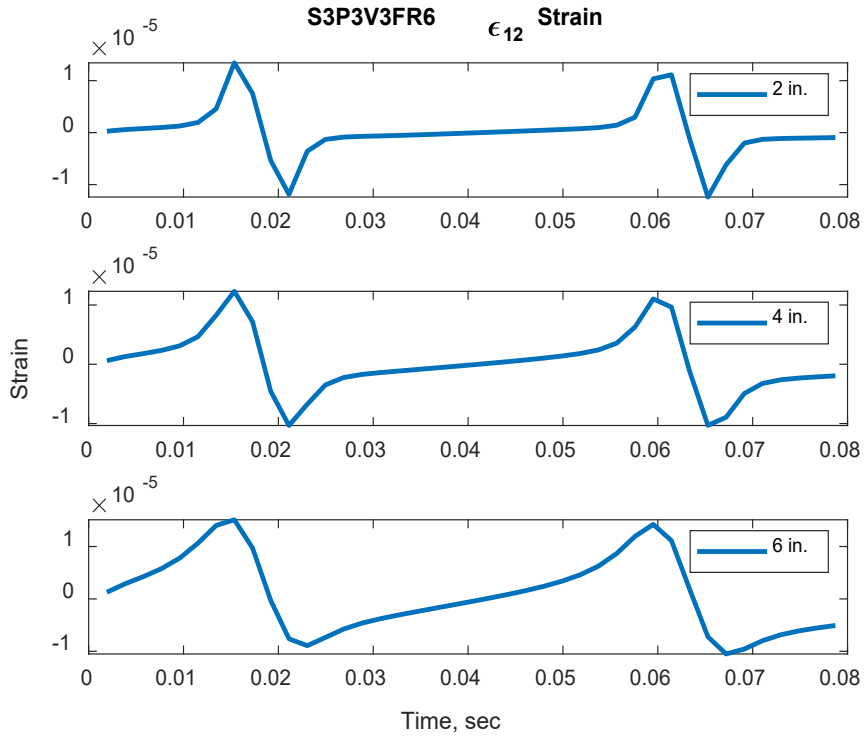

B. Longitudinal Shear Strain

Figure 10. Plot. Turning scenario for (a) transverse and (b) longitudinal shear strains.

CHAPTER 3: IMPACT OF PLATOONS ON FLEXIBLE PAVEMENTS

EXPECTED RESPONSE FRAMEWORK

Deterministic Response Profiles

To account for autonomous trucks and wheel wander, pavement responses (stresses and strains) were represented as a function of lane position, as given in Figure 11-A. Pavement response, $f(x)$, represents the strain profile along the lane width, where x represents the lane width. Assuming a typical lane width of 12 ft and a truck width of 8 ft, a truck can shift at most 2 ft to the left and right and still remain within the lane.

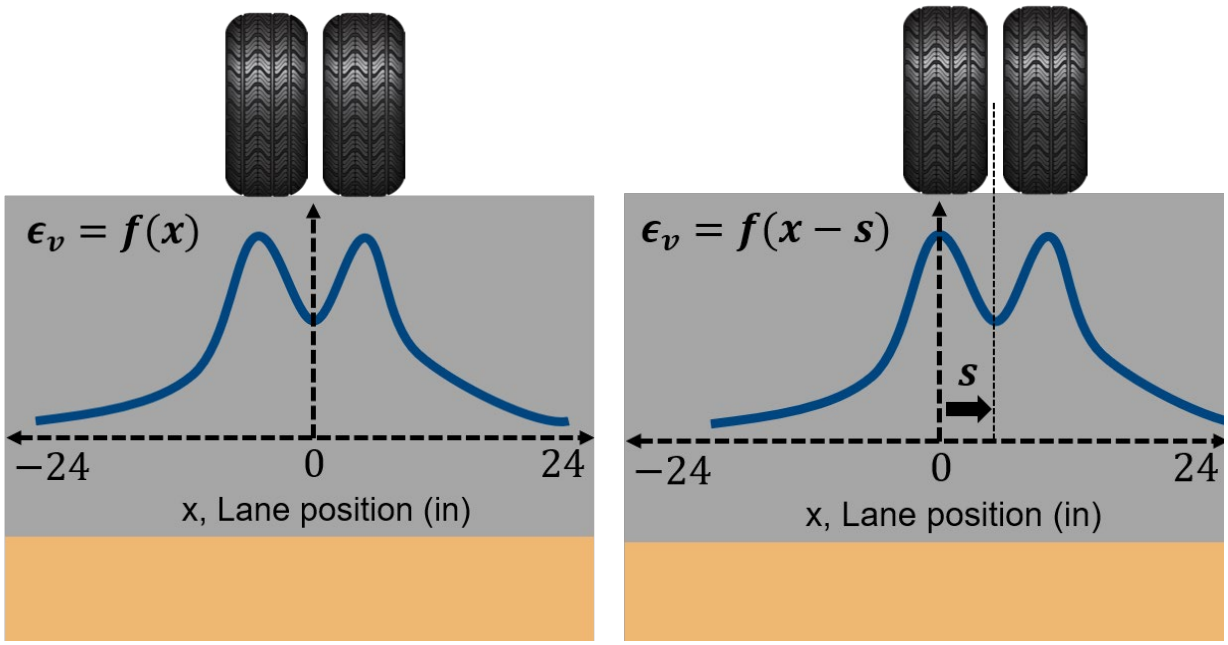

A. Deterministic strain profile when the truck is in the middle of the lane

B. Deterministic strain profile when the truck is shifted *s* to the right

Figure 11. Plot. Example of deterministic vertical strain profile at the middle of the hot-mix asphalt layer under dual-tire assembly.

Herein, $f(x)$ is referred to as the deterministic response profile and $f(x - s)$ is the deterministic response profile when the wheel is shifted by s. Gungor and Al-Qadi (2020) demonstrated that $f(x)$ can be represented with an analytical function using curve fitting, as given in Figure 12.

$$f(x) = \sum_{i=0}^{n} \alpha_i \Phi(x)^i \ , \Phi(x) = exp\left(-\left(\frac{x}{w_h \gamma}\right)^2\right)$$

Figure 12. Equation. Analytical representation of deterministic strain profile using curve fitting.

where, n is number of regression parameters, α_i is regression constants, w_h is wheel path width that is equal to 0.25 times the lane width, and γ is smoothing parameter, which can be learned alongside regression constants.

The parameters of the curve-fitting function, α_i, could be determined using regression, and the smoothing parameter, γ, could be fine-tuned with a grid search. Using curve fitting, pavement responses, which are collected at discrete points in space, could be represented as a continuous function. Figure 13 gives an example of a curve fit with nine fitting parameters.

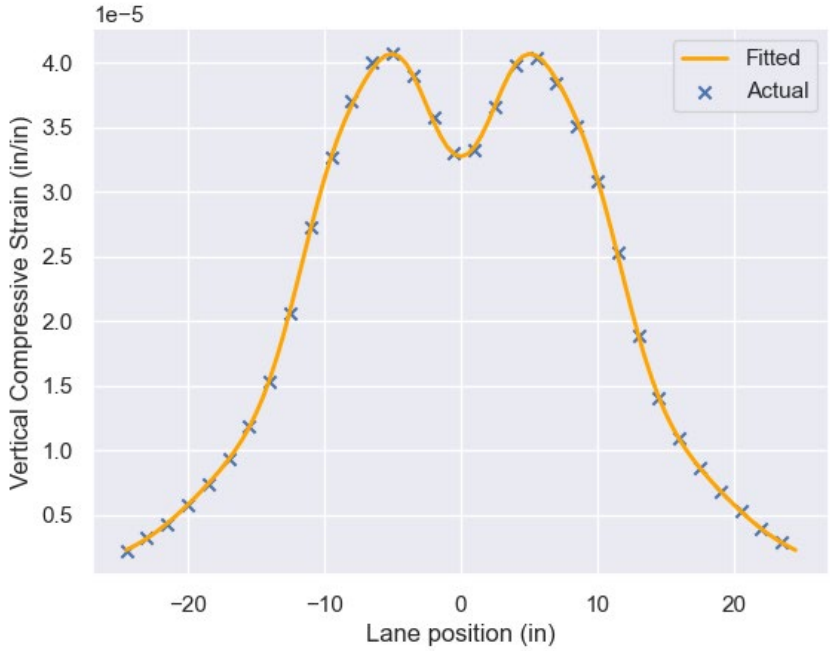

Figure 13. Plot. Curve-fitting performance for vertical compressive strain at the middle of the hot-mix asphalt layer.

Lane Position for Human-driven and Autonomous Traffic

Although human drivers tend to drive in the middle of the lane, their lane positions vary because of human perception. The National Cooperative Highway Research Program (NCHRP) recommends the use of zero mean normal variable with a standard deviation of 10 in (NCHRP, 2004) for the lane position of human-driven trucks. Because normal distribution requires infinite support and lane width is only 12 ft, this assumption is not mathematically accurate. However, it is acceptable because more than 98% of the distribution lies in the lane width, and the tail behavior is not a significant concern. Autonomous vehicles (AVs) have much more precise control over their lane positions. Zhou et al. (2019) reported that the standard deviation for AVs can be as small as 1.2 in, nearly one-tenth of the standard deviation for human-driven vehicles. Because AVs' standard deviations are so small, larger deviations can be programmed into their control systems to make them behave with a uniform distribution. Noorvand et al. (2017) also proposed this strategy to reduce pavement damage.

This study assumed that human-driven vehicles follow a normal distribution $N(0,10^2)$, where 0 is the mean and 10 in is the standard deviation, and autonomous vehicles follow a uniform distribution $U(s_l, s_u)$, where s_l, s_u are the lower and upper bounds, respectively. The range s_l, s_u is herein referred to as a sub-lane for autonomous trucks. For instance, if autonomous vehicles are forced to only use 2 ft of the available wander, then the sub-lane would be [−12 in,12 in]. With these definitions, the probability density function for wheel position $g(s)$ can be written as given in Figure 14 for all lane positions s.

$$g(s) = p_N * f_N(0, \sigma^2) + \sum_{j=1}^{m} \mathrm{p_j} * \mathrm{f_U}(s_l^j, s_u^j) * d_j \ , \ \forall \mathrm{s}$$

Figure 14. Equation. Probability density function of wheel position for a mixture of autonomous and human-driven traffic.

where, p_n is the percentage of human-driven vehicles. $f_N(0, \sigma^2)$ is the probability density function for normal distribution with a mean of 0 and a standard deviation (σ) of 10. m is the total number of sub-lanes assigned to autonomous vehicles. p_j is the percentage of autonomous vehicles at sub-lane j. $f_U(s_l^j, s_u^j)$ is the probability density function for uniform distribution. s_l^j, s_u^j are the lower and upper limits, respectively, of sub-lane *j*, and d_j is a form of the Iverson Bracket, as given in Figure 15, to determine if *s* lies in a given sub-layer.

$$d_j = \begin{cases} 1, & s_l^j \le s \le s_u^j \\ 0, & otherwise \end{cases}$$

Figure 15. Equation. Iverson bracket function to determine if *s* is in a sub-lane *j*.

The equation given in Figure 14 can be further developed by substituting the probability density functions, as demonstrated in Figure 16.

$$g(s) = \frac{p_n \exp\left(0.5\left(\frac{s}{\sigma}\right)^2\right)}{\sigma\sqrt{2\pi}} + \sum_{j=1}^{m} \frac{\mathrm{p_j} d_j}{s_u^j - s_l^j}, \ \forall \mathrm{s}$$

Figure 16. Equation. Final functional form of the probability density function for wheel position.

Writing the probability density function in this form has two advantages. First, any mixture of autonomous and human-driven vehicles can be represented by changing p_n and p_j, given that the summation equals 1. Second, the lane can be divided into as many sub-lanes as necessary by changing the total number of sub-lanes m and the range of the sub-lane $[s_l^j, s_u^j]$.

Figure 17 gives several examples of $g(s)$ under different traffic regimes. Note that even though trucks can use the entire lane width, consistently traveling near the centerline lane marker may negatively influence vehicles that occupy the left lane. In contrast, consistently traveling near the

shoulder may negatively impact structure stability, as the shoulders or lane edges have less structural capacity than the middle of the lane (Aksnes, 2002). Therefore, an ideal control strategy should not place the vehicles too close to either side of the lane. This decision could be revisited with more autonomous vehicle penetration and improved pavement design.

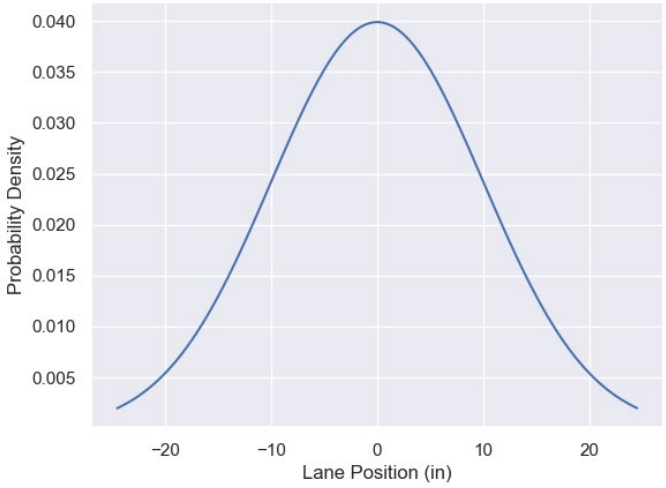

A. 100% human-driven vehicles

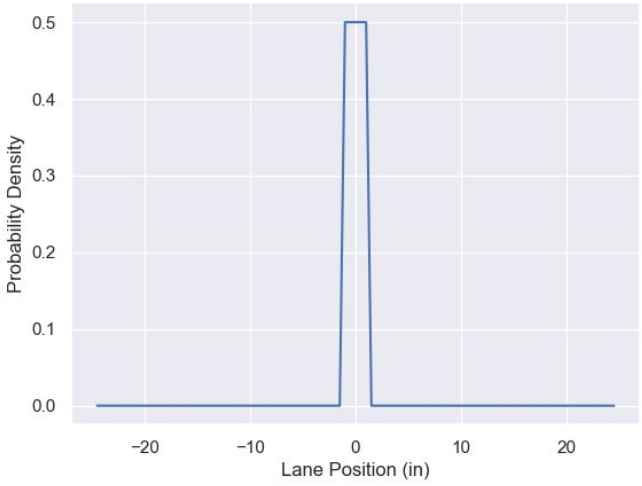

B. 100% autonomous vehicles with [−1,1] sub-lane (channelized traffic)

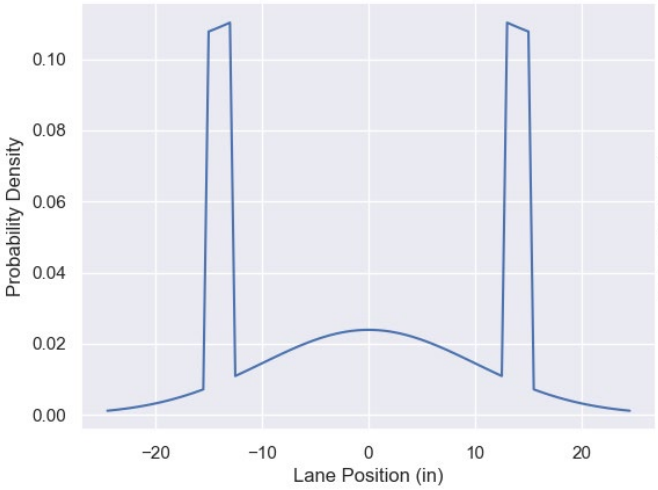

C. 40% autonomous vehicles with [−13,−15], [13,15] sub-lanes and 60% human-driven vehicles

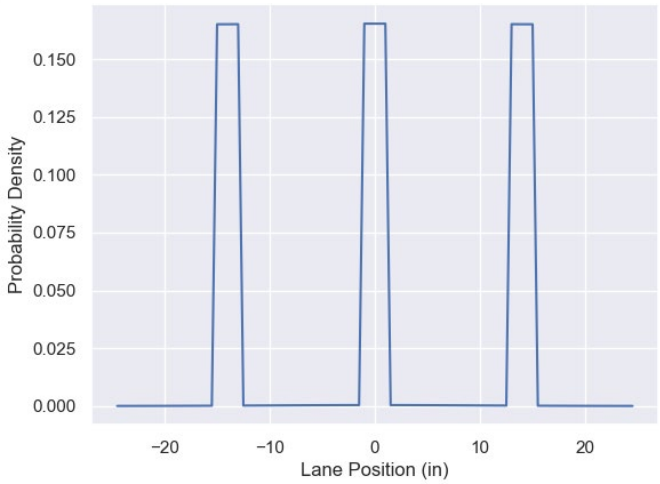

D. 100% autonomous vehicles with [−13,−15], [−1,1], [13,15] sub-lanes

Figure 17. Plot. Probability density functions for wheel position under different traffic regimes.

Response Profiles under Probabilistic Lane Position

For a truck pass, the deterministic response profile, $f(x)$, is the observed response profile only if the truck is at the center of the lane. Generally, a truck with an unknown lane position, s, will induce a response $f(x-s)$, where lane position s is a random variable that follows the probability density function $g(s)$. As s is a random variable, $f(x-s)$ is a random function. As there are tens of millions of load repetitions within the life of a pavement, it is useful to determine the expectation of

$f(x-s)$. The expectation of this function, $\mu_r(x) = E[f(x-s)]$, can be determined using the equation presented in Figure 18.

$$\mu_r(x) = E[f(x-s)] = \int_{-\infty}^{+\infty} f(x-s)g(s)ds$$

Figure 18. Equation. Expectation of response profiles.

The expectation, μ_r, can be computed in two ways. The first way is approximation by Monte Carlo simulation; $f(x-s)$ can be computed by sampling *s* from $g(s)$ many times and then averaging all $f(x-s)$. While this method is simple to implement, it is computationally inefficient. The second way of computing μ_r is to compute this integral analytically by substituting $f(x-s)$ and $g(s)$, as given in Figure 19.

$$\mu_r(x) = \int_{-\infty}^{+\infty} \sum_{i=0}^{n} \alpha_i \, exp\left(-i\left(\frac{x-s}{w_h\gamma}\right)^2\right)\left(\frac{p_n \exp\left(0.5\left(\frac{s}{\sigma}\right)^2\right)}{\sigma\sqrt{2\pi}} + \sum_{j=1}^{m} \frac{\mathrm{p_j} d_j}{s_u^j - s_l^j}\right) ds$$

Figure 19. Equation. Expectation of response profiles after substituting variables.

The full derivation of the expected response is given in the appendix. After taking the integral and simplifying the expression, the final form of $\mu_r(x)$ is presented in Figure 20, where $\mathrm{erf}\,(z)$ is the Gaussian error function.

$$\mu_r(x) = \alpha_0 + \sum_{i=1}^{n}\left[\frac{\alpha_i p_n ex\,p\left(-\frac{ix^2}{2i\sigma^2 + w_h^2\gamma^2}\right)}{\sqrt{2\sigma^2 + w_h^2\gamma^2}}\right] + \sum_{j=1}^{m}\left[\sum_{i=1}^{n}\left[\frac{\alpha_i p_j \sqrt{\pi} w_h^2\gamma^2}{2\sqrt{i}(s_u^j - s_l^j)}\left[\mathrm{erf}\left(\frac{\sqrt{i}(s_u^j - x)}{w_h^2\gamma^2}\right) - \mathrm{erf}\left(\frac{\sqrt{i}(s_l^j - x)}{w_h^2\gamma^2}\right)\right]\right]\right]$$

Figure 20. Equation. Final form of expected response expression.

The final form of the equation is a function of the percentage of autonomous vehicles as well as the number and location of sub-lanes assigned to them.

With this expression, the expected responses for any kind of traffic distribution can be computed. For example, for the distributions given in Figure 17, the expected vertical strain at the middle of an HMA layer can be plotted as presented in Figure 21. For channelized traffic, because all vehicles are in only one sub-lane, the expected response is nearly identical with the deterministic response. For human-driven traffic, the maximum of the expected response is significantly lower than the maximum of the deterministic response. It also has a much wider distribution in lane width. In the case of three sub-lanes, the maximum of the expected response is lower than that of human-driven traffic. For the mixed traffic, the maximum expected strain is nearly identical to the three-sub-layer scenario. However, human-driven traffic introduces smoothness to the overall profile.

It is evident that pavement responses can be altered using different traffic distributions. The next step was to compute pavement damage using expected responses to evaluate the impact of lateral position on pavement damage.

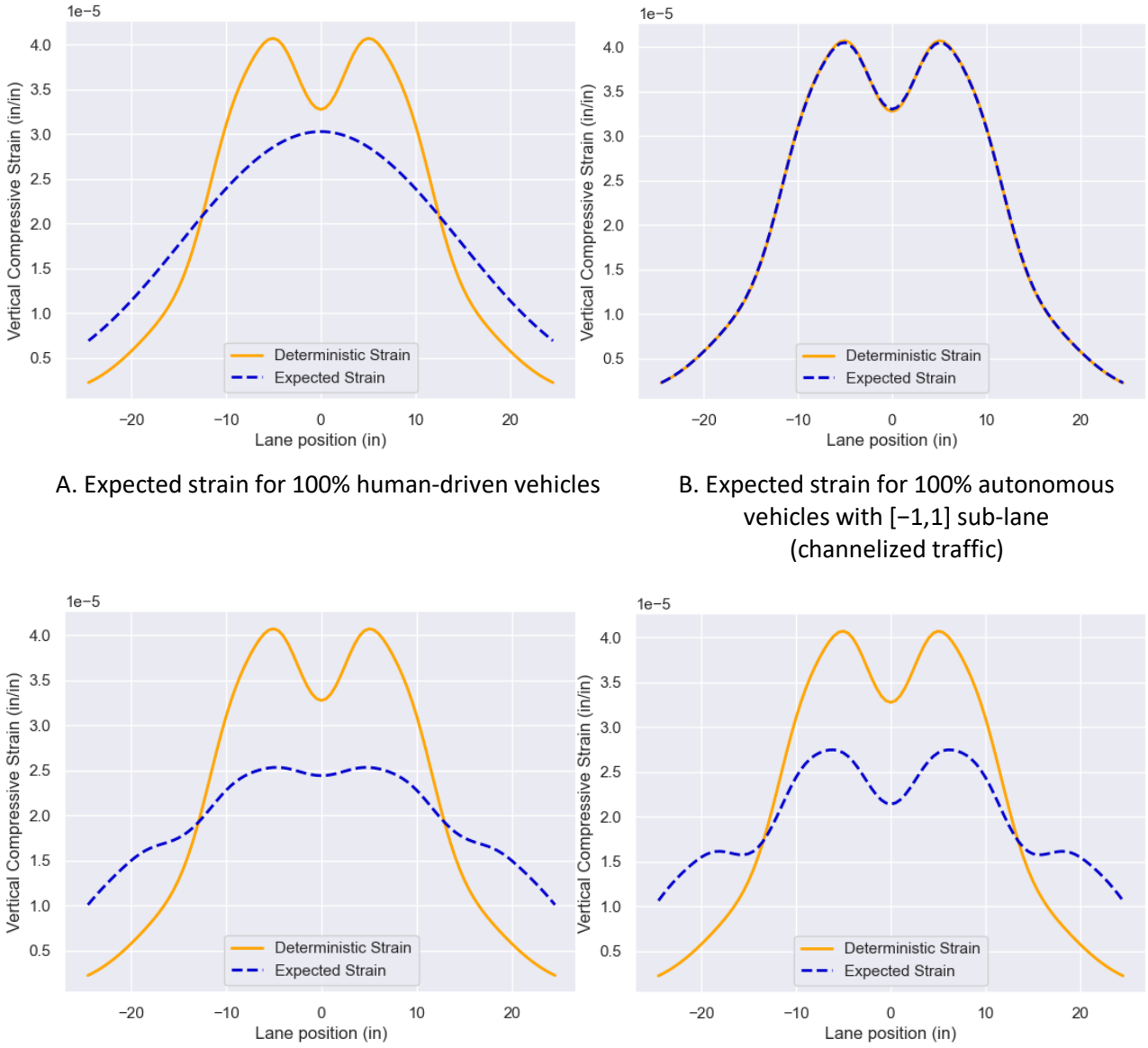

A. Expected strain for 100% human-driven vehicles

B. Expected strain for 100% autonomous vehicles with [−1,1] sub-lane (channelized traffic)

C. Expected strain for 40% autonomous vehicles with [−13,−15], [13,15] sub-lanes and 60% human-driven vehicles

D. Expected strain for 100% autonomous vehicles with [−13,−15], [−1,1], [13,15] sub-lanes

Figure 21. Plot. Expected vertical strain of the HMA layer for different traffic distributions.

PAVEMENT DAMAGE CALCULATION WITH EXPECTED RESPONSES

This study focuses on fatigue cracking and permanent deformation (rutting) of flexible pavements. The models used for cracking and rutting are adopted from AASHTOWare PMED (AASHTO, 2020).

Fatigue Cracking

Fatigue cracking is characterized by separating the damage from different load groups and axle types. Miner's Law is then applied to determine the total cumulative damage from all load groups and axle types. The damage index (*DI*) can be calculated as given in Figure 22.

$$DI = \sum_{k=1}^{K} \frac{n_k}{N_{f_k}}$$

Figure 22. Equation. Damage index definition.

where, n_i is the number of repetitions of load group *k*, and N_{f_k} is the number of allowable repetitions of load group *k*. N_{f_k} can be calculated as given in Figure 23.

$$N_{f_k} = k_{f_1} * C * C_H * B_{f_1} * \epsilon_t^{-3.9492 * B_{f_2}} E_{HMA}^{-1.281 * B_{f_3}}$$

Figure 23. Equation. Allowable number of repetitions.

where k_{f_1} is 0.007566, and $B_{f_1}, B_{f_2}, and\ B_{f_3}$ are global calibration coefficients that are set to 1. C_H is the correction for bottom-up and top-down cracking, and *C* is the correction term for HMA mixture properties. The expressions for *C* and C_H are given in the appendix. E_{HMA} is the HMA modulus in psi. ϵ_t is the tensile strain at the critical locations and should be collected at the bottom and top of the HMA layer for bottom-up and top-down cracking, respectively.

Both damage index (*DI)* and N_{f_k} are random functions of the strain because strain is a random function of wheel position. The expectation of *DI* can be computed as given in Figure 24.

$$\mu_{DI} = E[DI] = \sum_{k=1}^{K} E\left[\frac{n_k}{N_{f_k}}\right], \mu_{DI} = \sum_{k=1}^{K} n_k E\left[\frac{1}{N_{f_k}}\right]$$

Figure 24. Equation. Expectation of damage index.

The expression simplifies because the expectation of any $1/N_{f_k}$ is identical. The expectation of $1/N_{f_k}$ can be computed after calculating $1/N_{f_k}$ using Figure 23 and applying the expectation function given in Figure 20 for all load groups. Finally, fatigue cracking at the surface of HMA can be approximated with the equation given in Figure 25 as a function of lane position x.

$$FC_{\text{bottom}} = \frac{1}{60} \frac{6000}{1 + \exp(\mathrm{C}_1^* - \mathrm{C}_2^* \log 10(\mathrm{DI}_{\text{bottom}} * 100)}, \qquad FC_{\text{top}} = 10.56 \frac{2300}{1 + \exp(\mathrm{C}_1 - \mathrm{C}_2 \log 10(\mathrm{DI}_{\text{top}} * 100)}$$

Figure 25. Equation. Fatigue cracking for top-down and bottom-up cracking modes.

where, FC_{bottom} is the bottom-up fatigue cracking in % lane area; FC_{top} is the top-down fatigue cracking in ft/mi; C_1, C_2 are 7 and 3.5, respectively; and *DI* is damage index coming from both failure

modes. Note that bottom-up cracking is expressed in area, while top-down cracking is expressed in length. Expressions for C_1^*, C_2^* are provided in the appendix.

Rutting in the Hot-mix Asphalt Layer

Rutting in the HMA layer is computed by dividing the HMA layer into sub-layers and then computing the rut for each sub-layer. Sub-layering improves prediction accuracy by discretizing the pavement structure into smaller sections. The sub-layering algorithm is adopted from PMED sub-layering procedure. Rutting for a given load group is computed by the equation given in Figure 26.

$$Rut = \epsilon_p h_{HMA} = B_{1r} k_z \epsilon_v 10^{k_1} N^{k_2 B_{2r}} T^{k_3 B_{3r}}$$

Figure 26. Equation. HMA rutting prediction for a load group.

where, *Rut* is the total rutting of sub-layer in inches, ϵ_p is the plastic strain of sub-layer, and h_{HMA} is the thickness of sub-layer. $B_{1r}, B_{2r}, and\ B_{3r}$ are the global calibration coefficients and are equal to 1 by default. k_z is the depth-correction factor provided in the appendix. ϵ_v is the vertical compressive strain in middle of the HMA sub-layer. $k_1, k_2, and\ k_3$ are the calibration parameters equal to −3.35412, 0.4791, and 1.5606, respectively. N is the number of repetitions of load group, and T is the HMA temperature in Fahrenheit.

Unlike fatigue cracking, accumulation of rutting is not linear. Whenever any variable in Figure 26 changes, the number of equivalent cycles in the new loading scenario is computed. Then, the number of repetitions of the new loading scenario is added to the number of equivalent cycles. Figure 28 presents a graphical representation of this algorithm. Vertical strain ϵ_{v_1} is repeated N_1 times, resulting in plastic strain ϵ_{p_1}. When the loading scenario changes to ϵ_{v_2}, the first step is to compute N_{eq}, the number of equivalent cycles to reach ϵ_{p_1} under ϵ_{v_2}. The next step is to add N_2 on top of N_{eq} to calculate ϵ_{p_2}. To incorporate wheel position, this procedure must be repeated each time the wheel position changes. With this methodology, rutting at any step *i* can be written as given in Figure 27.

$$Rut_i = h_{HMA} B_{1r} k_z \epsilon_{v_i} 10^{k_1} (N_{eq_i} + N_i)^{k_2 B_{2r}} T^{k_3 B_{3r}}, N_{eq_i} = \frac{Rut_{i-1}}{B_{1r} k_z \epsilon_{v_i} 10^{k_1} T^{k_3 B_{3r}}}$$

Figure 27. Equation. Rutting accumulation function.

where Rut_i is the rut depth at the end of load pass *i*. ϵ_{v_i} is the vertical compressive strain in the middle of the sub-layer at step *i*. N_{eq_i} is the number of equivalent cycles to reach Rut_{i-1} with ϵ_{v_i}. N_i is the number of repetitions of ϵ_{v_i}. This algorithm makes rutting a recursive function, where rut depth at any step is a function of the previous step.

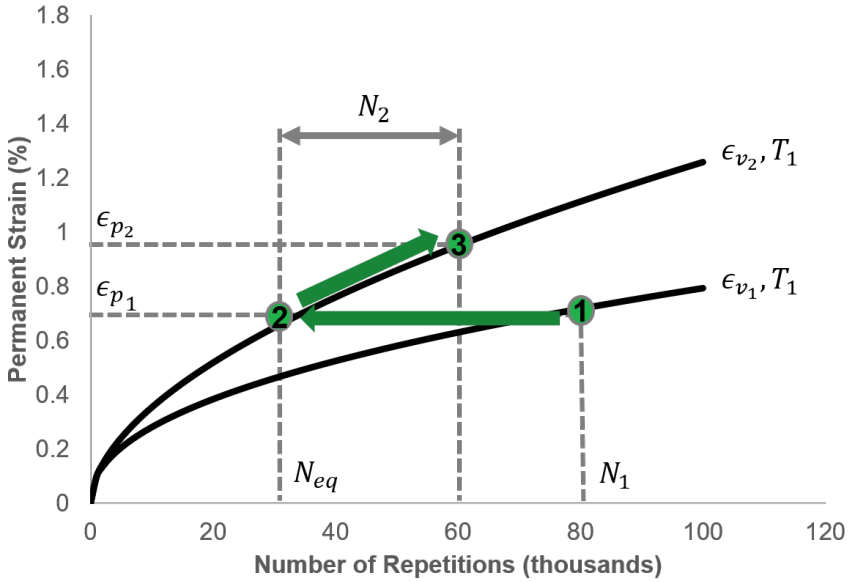

Figure 28. Plot. Rutting accumulation methodology.

Like fatigue cracking, Rut_i is a random function of wheel position. It is important to note that when rutting is computed for a platoon of trucks, s is repeated as many times as the axles pass in the platoon. While implementation of this algorithm is simple when wheel position s is known at every step, calculating the expected value of this recursive function is complicated. Alternatively, Rut_i can be calculated using the expected responses given in Figure 29.

$$Rut_i = \mathrm{k_i^{AC}Rut_i^e},\ \mathrm{Rut_i^e} = h_{HMA}B_{1r}k_z E[\epsilon_v]10^{k_1}N_{tot_i}^{k_2B_{2r}}T^{k_3B_{3r}}$$

Figure 29. Equation. Rutting accumulation using expected vertical strain at sub-layer.

where, Rut_i^e is the rut depth at step *i* computed with the expectation of vertical strain $E[\epsilon_v]$ at a sub-layer. N_{tot_i} is the total number of repetitions including load *i*. k_i^{AC} is the correction factor and ratio of Rut_i to Rut_i^e. $E[\epsilon_v]$ can be computed with the equation given in Figure 20 at every sub-layer using deterministic strains at that sub-layer.

With this new algorithm, the only required input is the correction factor k_i^{AC}. By definition, k_i^{AC} changes at each step *i*. Because rutting follows a power function, its progression starts as nonlinear and then becomes more linear with an increasing number of passes. Therefore, k_i^{AC} should converge to a constant. Figure 30 presents the evolution of k_i^{AC} vs. number of passes for human-driven traffic conditions. Rut_i^e underpredicts the total rutting of the sub-layer by 19% and can be corrected with k_i^{AC}. This trend is observed for all types of traffic distributions. k_i^{AC} oscillates during the initial number of passes but quickly converges to a number after a few hundred repetitions. Rate of convergence is a function of the platoon size and variability of the traffic distribution. The convergence of k_i^{AC} is useful because simulating all load repetitions (which can be on the order of

millions of repetitions depending on the season) is not necessary. Only a few hundred to a few thousand load repetitions are required to compute the rutting profile.

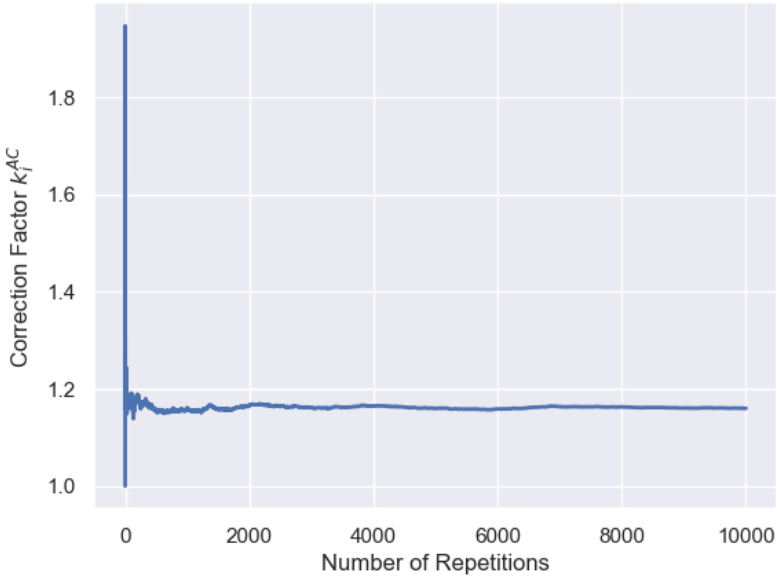

Figure 30. Plot. Convergence of HMA rutting correction factor for human-driven traffic.

Figure 31 gives an example of the rutting profile prediction for a sub-layer, and Figure 17-D gives the traffic regime used in this example. Note that the shape of the actual rutting profile obtained by simulation is closely related to the shape of the rutting profile obtained by expected strain. Correction factor k_i^{AC} was obtained after 400 repetitions at the location of maximum expected strain. For better representation, k_i^{AC} can be obtained at multiple points along the lane width. Lane position is a critical parameter because deterministic strains overpredict HMA rutting.

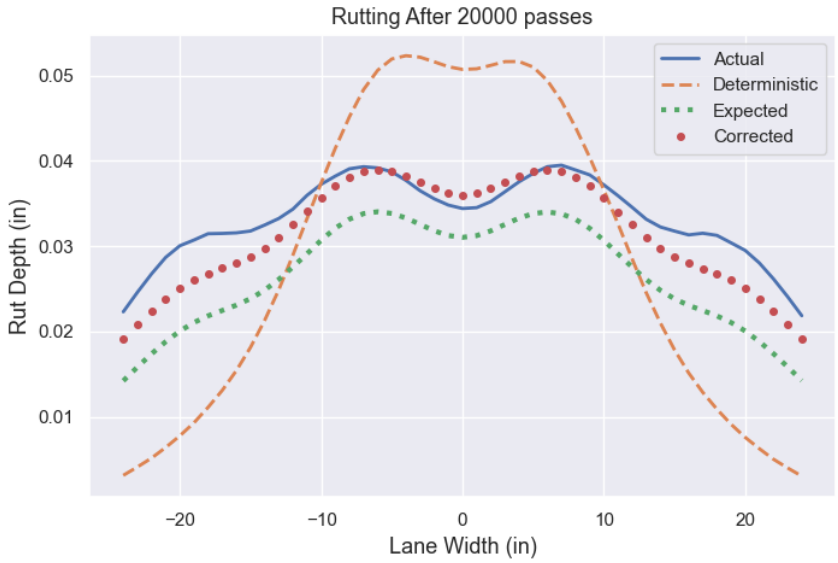

Figure 31. Plot. Comparisons of rutting profile with deterministic, expected, and corrected-expected strain profiles. Correction applied after 400 passes.

Figure 32 summarizes the HMA rutting algorithm. This procedure must be repeated for all sub-layers in the HMA layer. Operations can be vectorized for efficiency.

Algorithm Rutting

procedure RUT
  Set $k_0 = 10$, $tol = 10^{-3}$, $Rut_0 = 0$, $i = 1$
  $c = 500$ ▷ Convergence of the last c items
  while True **do**
    Sample s from $g(s)$ ▷ Sample position for truck or platoon
    Calculate $f(x-s)$ ▷ Compute deterministic strain
    Calculate Rut_i with $f(x-s)$ ▷ Accumulate rutting
    Calculate Rut_i^e with $E[f(x-s)]$ ▷ Approximate rutting
    Set $k_i = Rut_i / Rut_i^e$ ▷ Correction factor
    if $i \geq c$ **then**
      if $|\overline{k_{i-c:i}} - k_i| < tol$ **then** ▷ Test for convergence
        Break **while** loop
    Set $i = i + 1$
  Calculate Rut_N with $E[f(x-s)]$ and k_i ▷ Final rutting

Figure 32. Algorithm. Pseudocode for rutting accumulation.

Rutting for Unbound Layers

Rutting for unbound layers (subgrade and/or granular base) follows a similar procedure to rutting in the HMA layer. Unbound layers need to be sub-layered with the PMED procedure. Rutting for a sub-layer in the unbound layers is calculated in Figure 33.

$$Rut = B_{s_1} k_{s_1} \epsilon_v h_{soil} \left(\frac{\epsilon_o}{\epsilon_r}\right) \exp\left(-\left(\frac{\rho}{N}\right)^{\beta}\right)$$

Figure 33. Equation. Rutting of unbound layers for a load group.

where, *Rut* is the total rutting of the sub-layer in inches. B_{s_1} is a global calibration coefficient set to 1. k_{s_1} is 2.03 and 1.35 for granular and fine-grained materials, respectively. ϵ_v is the vertical strain in the middle of the sub-layer. h_{soil} is the sub-layer thickness in inches. *N* is number of repetitions of load group. Expressions for all other parameters are given in the appendix.

Rutting accumulation of unbound materials is similar to rutting accumulation of the HMA layer. Whenever a condition changes in Figure 33, the number of equivalent cycles in the new loading scenario is computed. Then, the number of repetitions of the new loading scenario is added to the number of equivalent cycles. Rutting at any step *i* can be written as given in Figure 34.

$$Rut_i = B_{s_1} k_{s_1} \epsilon_{v_i} h_{soil} \left(\frac{\epsilon_o}{\epsilon_r}\right) \exp\left(-\left(\frac{\rho}{N_{eq_i} + N_i}\right)^{\beta}\right), \; N_{eq_i} = \rho \left(-ln\left(\frac{Rut_{i-1}}{B_{s_1} k_{s_1} \epsilon_{v_i} h_{soil} \left(\frac{\epsilon_o}{\epsilon_r}\right)}\right)\right)^{-\frac{1}{\beta}}$$

Figure 34. Equation. Rutting accumulation for unbound materials.

where, Rut_i is the rut depth at the end of load pass *i*. ϵ_{v_i} is the vertical compressive strain in the middle of the sub-layer at step *i*. N_{eq_i} is the number of equivalent cycles to reach Rut_{i-1} with ϵ_{v_i}. N_i is the number of repetitions of ϵ_{v_i}. The expectation of this recursive function is also difficult to compute, and it was approximated as presented in Figure 35.

$$Rut_i = k_i^{UB} Rut_i^e = B_{s_1} k_{s_1} E[\epsilon_v] h_{soil} \left(\frac{\epsilon_o}{\epsilon_r}\right) \exp\left(-\left(\frac{\rho}{N_{tot_i}}\right)^{\beta}\right)$$

Figure 35. Equation. Rutting accumulation for unbound layers using expected strain at sub-layer.

where, Rut_i^e is the rut depth at step *i* computed with the expectation of vertical strain $E[\epsilon_v]$ at a sub-layer. N_{tot_i} is the total number of repetitions including load *i*. k_i^{UB} is the correction factor and ratio of Rut_i to Rut_i^e. $E[\epsilon_v]$ can be computed using the equation given in Figure 20 at every sub-layer using deterministic strains at that sub-layer. k_i^{UB} can be determined similarly by running simulations and observing convergence between Rut_i and Rut_i^e. An example of convergence for human-driven traffic is given in Figure 36. The magnitude of k_i^{UB} is observed to be smaller than k_i^{AC} for a given load group. This is due to the expansion of the response cone in deeper parts of the pavement structure. The impact of lane position diminishes for the sub-layers that are further from the surface.

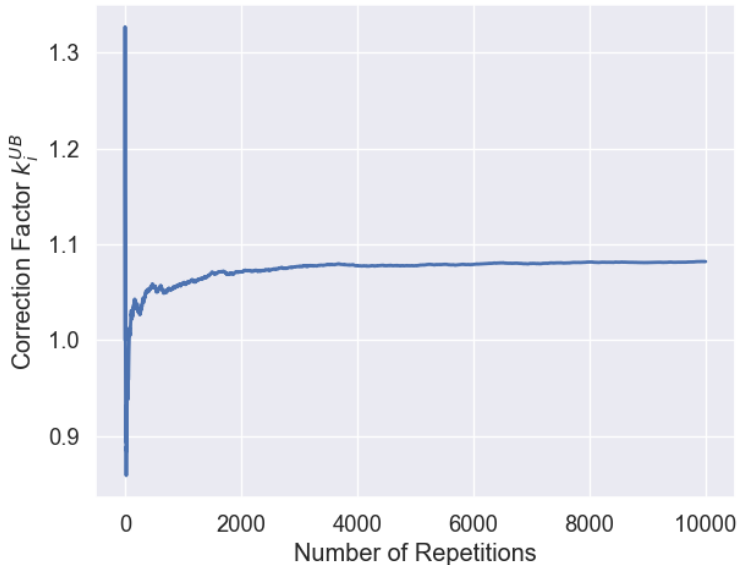

Figure 36. Plot. Convergence of unbound rutting correction factor for human-driven traffic.

Rutting in the unbound layers can be accumulated using the procedure described in Figure 32. The total rut depth of the pavement system is calculated as the summation of rutting in the unbound layers and the rutting in the HMA layers.

Example of Pavement Performance Using Expected Responses

An example pavement section is analyzed using the expected response approach. Figure 37 provides information about the pavement section and the loading. The dynamic moduli of the HMA tested at

71°F are 1,740 ksi, 1,000 ksi, and 200 ksi at 100 Hz, 1 Hz, and 0.01 Hz, respectively. The daily truck traffic is assumed to be 500 vehicles traveling at 70 mph. As provided in Figure 17, four traffic regimes are considered for the wheel position: human driven, channelized, mixed, and fully autonomous. For mixed traffic and fully autonomous traffic, sub-lanes are changed from ±[13,15] to ±[22,24] to show the full potential of lane position optimization. However, sub-lanes could be reviewed for practical application. Figure 38 presents the results for fatigue cracking and rutting after 10 years.

To compute fatigue cracking, structural responses are obtained from the bottom and top of the HMA layer. Using these responses, the expectation of $1/N_f$ is computed. Then, the expected damage index, μ_{DI}, is computed using Figure 24. To compute rutting, the structure is separated into sub-layers. Then, the total rut is computed by the algorithm given in Figure 32 using the expected strains in the middle of each sub-layer.

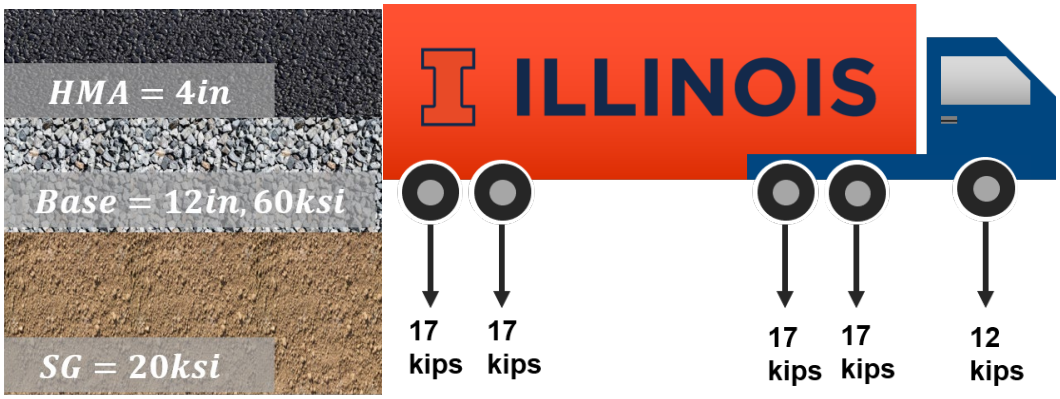

A. Example pavement structure B. Example truck

Figure 37. Illustration. Example pavement section and loading.

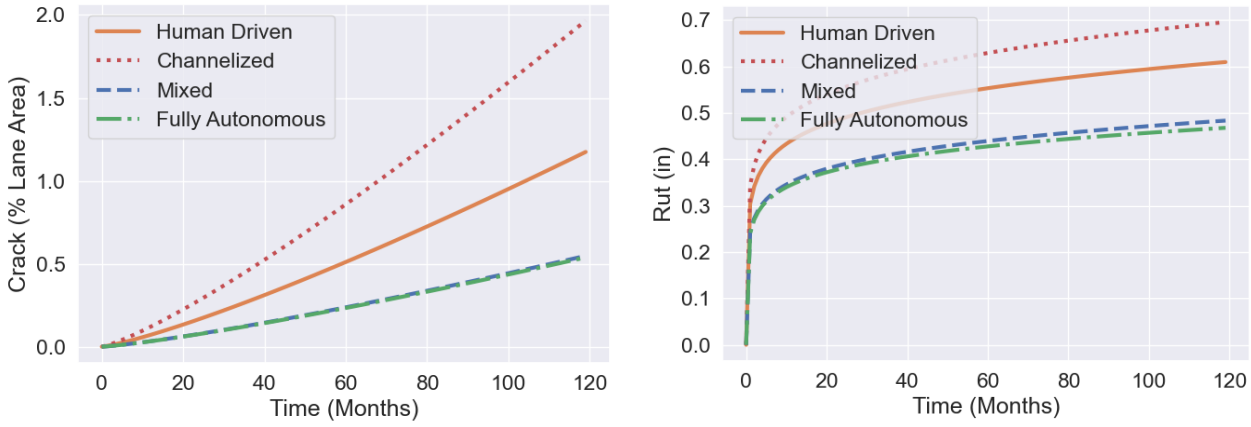

A. Fatigue cracking performance B. Rutting performance

Figure 38. Plot. Performance prediction of an example section using four traffic regimes.

From the performance predictions, channelized traffic significantly increases pavement damage. It increases cracking by 60% and rutting by 25% compared to the baseline for human-driven traffic. However, damage can be reduced by shifting the percentage of vehicles to the left and right edges of the lane. In the mixed-traffic regime, where 20% of the vehicles are on the right edge and 20% of the vehicles are on the left edge, cracking is reduced by 40% and rutting is reduced by 20% compared to the baseline. In the fully autonomous traffic regime, damage stays almost the same for cracking, and there is slight improvement for rutting. It should be noted that safety limitations were not considered in traffic simulations. This data show that CAVs can be used to improve pavement performance if lane position optimization is enforced. If the optimization is not enforced, the channelized traffic will increase pavement damage. The improvements slow down with increasing penetration levels. This relationship is presented in the upcoming chapter.

ROUGHNESS PREDICTION MODEL FOR PLATOONING VEHICLES

A change in pavement surface roughness over time is an important indicator of pavement performance. Pavement roughness, as defined by ASTM Standard E867, is “the deviations of a pavement surface from a true surface with characteristic dimensions that affect vehicle dynamics, ride quality, dynamic loads and drainage” (Newland, 2012). The international roughness index (IRI) is used to indicate pavement roughness using the average rectified slope (accumulated suspension motion to distance traveled), as derived from a mathematical model of a standard quarter car passing over a measured profile at a speed of 50 mph (Ozbay & Laub, 2001). Predicting the progression of roughness during pavement life is important for pavement management system (PMS) decision-making. However, various factors affect pavement surface roughness, such as traffic, climate, pavement structure and material type, pavement construction quality, and maintenance and rehabilitation activities. Thus, it is impractical to develop a single roughness prediction model that includes the aforementioned factors.

Because of the high prediction accuracy achieved by machine learning algorithms, artificial neural networks (ANN) have been increasingly used in pavement engineering applications (Attoh-Okine, 1994). ANN is a multilayer, fully connected neural network. It consists of an input layer, multiple hidden layers, and an output layer. Each node in one layer is connected to nodes in the next layer. The network becomes deeper by increasing the number of hidden layers. Each given node takes the weighted sum of previous nodes and passes the sum through a nonlinear activation function. An ANN is trained by learning the weights assigned to all edges between nodes. Recurrent neural networks (RNN) is a class of ANNs where nodes from a directed graph along a temporal sequence are connected. In a traditional ANN, all inputs (outputs) are independent of each other. RNNs are called recurrent because they perform the same task for every element of a sequence, with the output being dependent on the previous computations. Thus, RNN can handle time-series data because it memorizes the previous information in the hidden layers. In this study, RNN is used to predict pavement roughness.

Model Description

Figure 39 presents the profile of the recurrent structure of the RNN model in this study. The RNN repeatedly receives and processes the input data and previous data. The RNN can consider data of

different sequence lengths (SLs). Therefore, it can learn the effect of past data on subsequent data, which is analogous to predicting the next word in a sentence based on the words before it. With these characteristics, RNNs can be used to predict time-series data, such as stock prices, whose input data take the form of a time sequence.

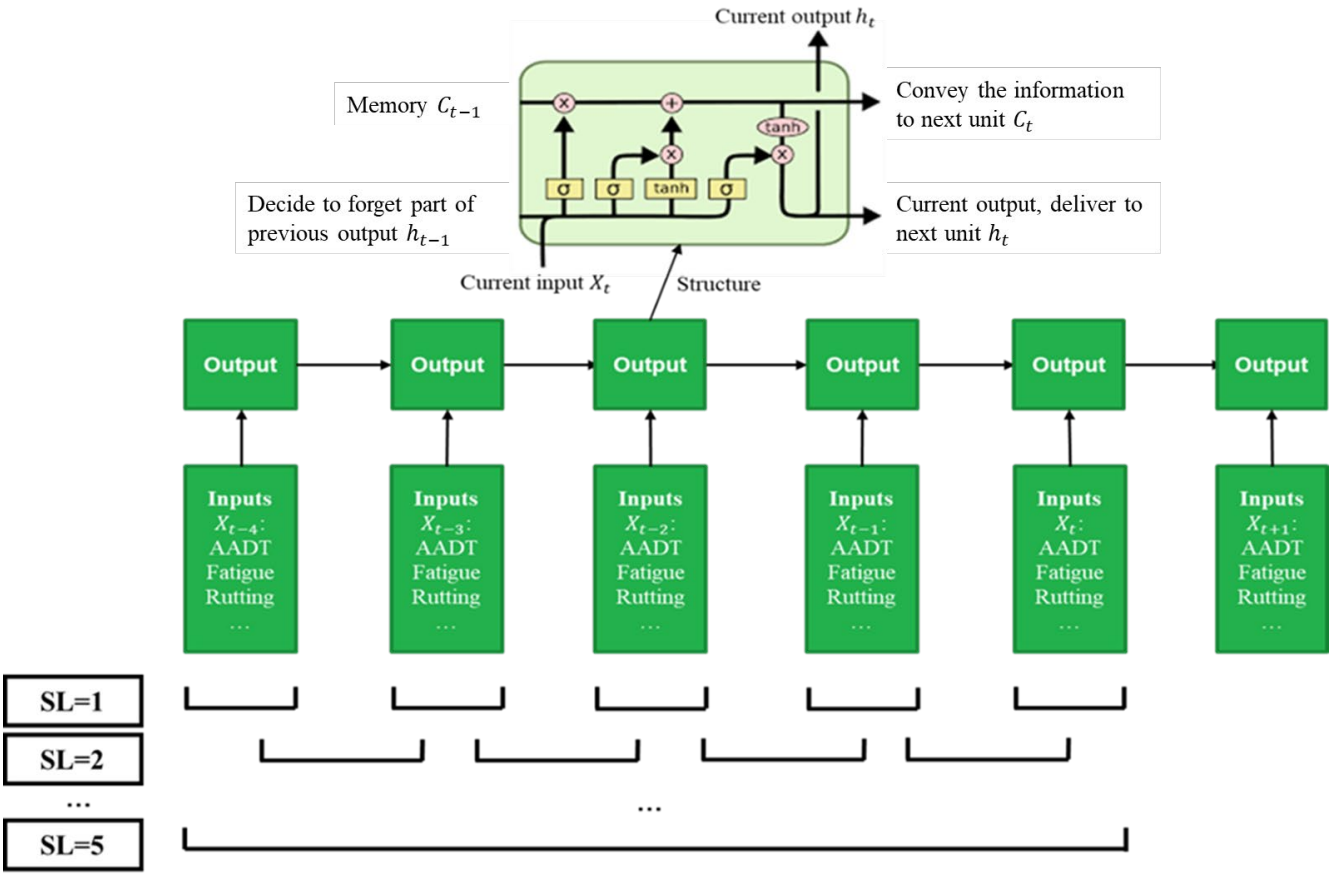

Figure 39. Flowchart. Structure of the recurrent neural network.

Long short-term memory (LSTM), shown in Figure 39, is an upgraded RNN that solves RNN's vanishing gradient problem and makes it effective in capturing long-term dependencies (Hochreiter & Schmidhuber, 1997). It is already being utilized in voice recognition, language modeling, translation, and other fields, in combination with other neural networks. It is composed of a memory movement cell that can maintain a state over time as well as three nonlinear gates that control data flow in and out of the cell. The memory cell (C_t) updates the state (h_t) at a specific time and decides whether information inside should be updated by using the status from the input at that moment. In addition, there are several gate types—input (i_t), forget (f_t), and output (o_t)—that control the flow of the cell.

The forget gate, f_t, decides which past information shall be removed (see Figure 40). The output of the previous cell (h_{t-1}) and the current input (X_t) are applied in the sigmoid function active layer to obtain a value in the range [0,1]. This value is multiplied by the current state and the elements, and the cell chooses whether to keep or eliminate this information during the process.

$$\mathrm{f_t} = \sigma(W_f \times [h_{t-1}, X_t] + b_f)$$

Figure 40. Equation. Forget gate computation.

The input gate, i_t, is used to decide which information shall be stored in the cell state, as presented in Figure 41. Two stages are categorized in this process: (i) using the sigmoid function to decide the information to be updated and (ii) creating a candidate cell ($\tilde{C}_t$) that could be added to the state using the hyperbolic tangent (*tanh*) function (see Figure 42).

$$\mathrm{i_t} = \sigma(W_i \times [h_{t-1}, X_t] + b_i)$$

Figure 41. Equation. Input gate computation.

$$\tilde{C}_t = tanh(W_c \times [h_{t-1}, X_t] + b_c)$$

Figure 42. Equation. Candidate cell computation.

where, W_i and W_c are weights of input gate and candidate cell, respectively, and b_i and b_c represent the biases of the input gate and candidate cell, respectively.

Then, the old cell state (C_{t-1}) and the candidate cell state ($\tilde{C}_t$) are used to represent the updated current cell status (C_t), as presented in Figure 43. The old cell state (C_{t-1}) is multiplied by f_t, indicating to forget the information decided in the forget gate, while the candidate cell state ($\tilde{C}_t$) is scaled by i_t, representing the extent of updating each state value.

$$\mathrm{C_t} = f_t \times C_{t-1} + i_t \times \tilde{C}_t$$

Figure 43. Equation. Current cell state computation.

In the end, the output gate (o_t) decides what should be outputted. This process is broadly categorized into two stages: (i) using the sigmoid function (see Figure 44) to decide which part of the cell state to output and (ii) putting the cell state through tanh (to push the values to be between −1 and 1) and multiplying it by the output of the sigmoid gate (see Figure 45). Finally, output h_t is updated.

$$o_\mathrm{t} = \sigma(W_o \times [h_{t-1}, X_t] + b_o)$$

Figure 44. Equation. Output gate computation.

$$\mathrm{h_t} = o_t \times \tanh(C_t)$$

Figure 45. Equation. Final output computation.

where W_o is weight of output gate and b_o is bias.

LSTM calculates the final output values through the hidden variables. Unlike a standard RNN that has the form of a chain of repeating the same modules of neural networks, LSTM adapts the information

flow by adjusting the gates appropriately during the variable calculation process of the hidden layer. Each module in LSTM has a different structure. As a result, the RNN using LSTM cells has the ability to remember information for long periods of time and handle long-term dependency problems.

LTPP Database Description

The Long-Term Pavement Performance (LTPP) program was initiated as a part of the Strategic Highway Research Program in 1987 and was expanded to a 20-year program under the coordination of the FHWA. The LTPP information management system is a pavement management database documenting historical performance data for over 2,500 in-service and monitored test sections in North America. Different types of information are stored within the database in the form of seven modules: inventory, maintenance, monitoring, rehabilitation, material testing, traffic, and climate data. The datasets extracted for this study were from the LTPP data documented for the United States and Canada. From the extracted data, sections with HMA over unbound granular layers were selected for analysis.

Various material, structural, and traffic parameters that affect a pavement's structural performance may be assessed through IRI observation over time. The World Bank developed a roughness prediction model through the Highway Development and Management program in which five factors contributed the most: cracking, rutting, potholes, environmental conditions, and structural deterioration (Odoki & Kerali, 2000). Thus, in this study, age, equivalent single axle loads (ESALs), rutting depth, fatigue cracking area, transverse cracking, evaporation, precipitation, average air temperature, and initial IRI after construction were used to relate pavement deterioration to IRI. Other possible parameters could be captured using the RNN algorithm, because RNN memorizes historical data behavior. This set of data has time-series information of 854 test sections, of which 683 were used to train the model and the remaining 171 were used to validate the model. Table 3 presents the description of the 854 sections.

Table 3. Descriptive Statistics of the Dataset

	Variable	Minimum	Maximum	Average	Median	Standard Deviation	Range
Input	Data collected year	1990	2017	2001.30	2001	0.15	27
	ESALs (million)	0.01	2.9	0.27	0.13	0.42	2.89
	Rut depth (mm)	0.00	27	5.94	5.0	3.19	27
	Fatigue cracking (m^2)	0.00	563.3	31.49	2.08	69.24	563.3
	Transverse cracking (m)	0.00	415.60	26.03	3.19	49.26	415.60
	Evaporation (mm)	48.85	1010.52	798.00	837.15	314.85	961.67
	Precipitation (mm)	32.95	4501.97	1025.05	1102.96	445.76	4469.02
	Average daily temperature (°C)	−5.70	26.70	14.46	15.20	5.75	32.40
Dependent	IRI (m/km)	0.24	4.29	1.21	1.09	0.49	4.05

IRI Progression Model

The hyperparameters of the RNN algorithms are generally the learning rate, number of epochs, and sequence length. Table 4 summarizes the data structures. The RNN algorithm was constructed to predict the IRI of pavement sections without maintenance/rehabilitation. The section data with maintenance/rehabilitation activities can be divided into pre- and post-maintenance/rehabilitation data. To prepare the learning model, 80% of the data was randomly selected, and the remaining 20% were used for validation/testing. This algorithm learned the time-series data with sequence length (SL) varying from one to four years. That is, to predict the IRI value in 2020, input data from 2020 is required if SL equals one, and input data from 2017–2020 are required if SL equals four. If SL is larger than four, then the model will always require a preparation of more than four years of historical data to predict the IRI value, which is not applicable at this time.

Table 4. Data Structures of Sequence Lengths of Number of Data Tuples

SL	No. of Data Tuples (854 sections)		
	Total	Train	Test
1	9,209	7,299	1,910
2	8,355	6,747	1,608
3	7,501	5,960	1,541
4	6,647	5,221	1,426

Table 5 summarizes the parameters of the RNN algorithm. A total of 854 sections were analyzed. The number of epochs (repetitions of learning) needs to be decided: learning should be stopped when the best prediction model has been constructed. It is important to stop learning at an early state because computing resources are limited, and learning time is restricted. The optimal number of epochs can be determined by plotting the number of epochs against the loss function results. In this study, experiments showed that the best loss function could be obtained when the number of epochs was between 40 and 50, and the loss value was almost unchanged after 50 epochs. The learning rate was maintained at 0.001.

Table 5. Parameters of the RNN Algorithm

Classification		Data
Hyperparameter	Learning rate	0.001
	No. of epochs	50
	Sequence length	1,2,3,4
	No. of LSTM layer	2
	No. of hidden states in each layer	10
Input variable	Traffic	ESALs
	Climate	Average temp, precipitation, evaporation
	Distress	Fatigue cracking, transverse cracking, rutting
Output variable		IRI

By varying SL between one and four, the value that minimized the root mean square error (RMSE) was judged to select the optimal model with an optimized SL value. Table 6 summarizes the results, and Figure 46 presents the prediction performance of the RNN algorithm with different SL values.

Table 6. Results of Analysis

Classification		Sequence Length			
		1	2	3	4
IRI (in/mi)	RMSE	0.25	0.22	0.30	0.28
	R^2	0.9258	0.9312	0.8744	0.9012

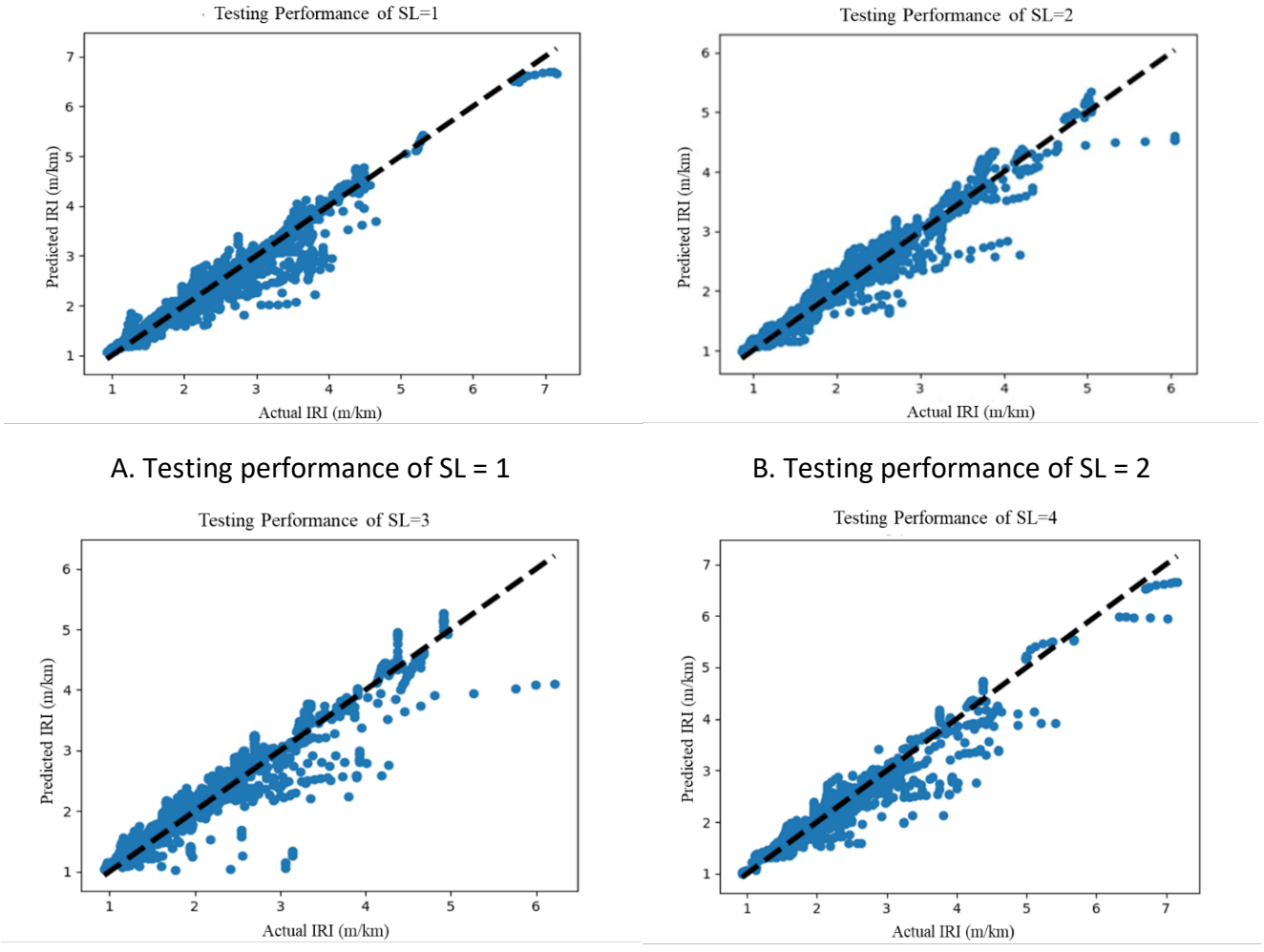

A. Testing performance of SL = 1

B. Testing performance of SL = 2

C. Testing performance of SL = 3

D. Testing performance of SL = 4

Figure 46. Graph. Testing performance of different sequence length values.

The results of the model indicated that SL played an important role in optimizing model prediction. Increasing SL does not guarantee better performance of RNN models. In this study, a SL of 2 achieved the lowest RMSE, which was 27% lower than the RMSE for SL of 3. The coefficients of determination (R^2) of the testing results reached as high as 0.93 using SL of 2, which is 6.5% higher than the lowest R^2.

CHAPTER 4: PLATOON CONFIGURATION OPTIMIZATION

OPTIMIZATION OVERVIEW

Genetic Algorithm

Optimization is a good tool to use when decision-making is involved (Chong & Zak, 2004). The closer the description of the system is to reality, the closer the optimal solution is to being practical. The mathematical model consists of an objective function (what is sought to be maximized or minimized) and constraints. Constraints describe the rules by which the system works (e.g., IRI progression equation) or force decision rules to the model (e.g., not to choose a platooning position that is out of the space designated for sub-lanes). In both cases, the model follows the given constraints to choose values of the decision variables that will maximize/minimize the objective function as needed.

Because of the complexity of the optimization model, inclusion of nonlinear components, and other considerations, the use of metaheuristics (like a genetic algorithm) is a common choice. Inspired by the theory of evolution, genetic algorithms have been applied to a broad range of problems (Whitley, 1994). A genetic algorithm is considered a useful tool in cases that do not get stuck in local optima, because of its random nature (mutations). It has been used in the context of life cycle optimization. Gungor et al. (2019) presented a similar example on the use of genetic algorithms. They worked on the optimization of truck positions in a platoon to minimize the total life cycle cost, taking into account the trade-off between fuel savings (advantage) and amplified pavement damage (disadvantage) of all trucks in the same line. Figure 47 presents the flowchart of a genetic algorithm.

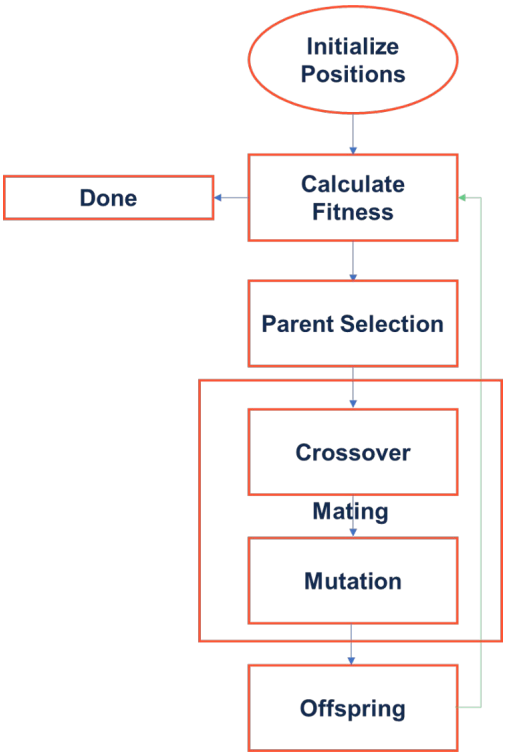

Figure 47. Chart. Flowchart of a genetic algorithm.

However, in this work, the assumption was that all trucks in the same platoon were aligned to follow each other. In other words, the reduction of damage will not come from dispersing trucks in the same platoon but might come from distributing platoons over the width of the lane. Here, optimization is focused on the minimization of damage. The two main forms of load-related damage in flexible pavement (rutting and fatigue cracking) were minimized. In addition, IRI—which is a combination of multiple forms of damage, including rutting and fatigue cracking—was also minimized by controlling the lateral position of the platoons.

Applying this algorithm in this study, Figure 48 presents the resulting algorithm. The initial population is generated randomly within the given range of decision variables (lateral position values). Then, the probability function of the expected strain (resulting from the multiplication of the strain function and the probability distribution of the truck position) is calculated. The next step was to determine the highest strain value. Substituting this in the damage estimation equations presented in Chapter 3, the estimated damage (the fitness value) was identified. For rutting and fatigue cracking, the process and equations are shown in Chapter 3. For roughness, the equation shown in Figure 49 was used.

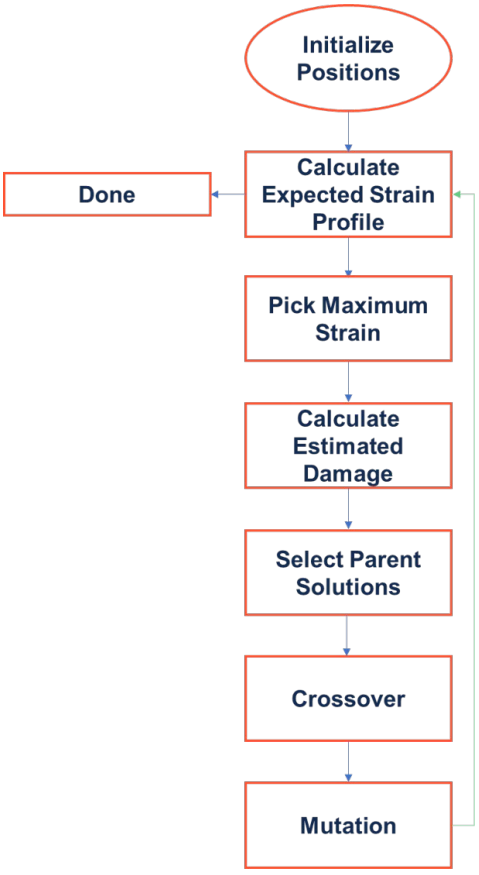

Figure 48. Chart. Flowchart of the algorithm at use.

$$IRI = IRI_0 + 0.0150(SF) + 0.400(FC_{Total}) + 0.0080(TC) + 40.0(RD)$$

Figure 49. Equation. PMED IRI progression equation.

where, IRI_0 is initial IRI in in/mi, FC_{Total} is total area of fatigue cracking in percent of the lane, *TC* is length of transverse cracking in in/mi, *RD* is rut depth in inches, and *SF* is a site factor, which can be calculated by the equation presented in Figure 50.

$$SF = Age[0.02003(PI + 1) + 0.007947(Precip + 1) + 0.000636(FI + 1)]$$

Figure 50. Equation. PMED IRI progression site factor.

where, Age is pavement age in years, *PI* is plasticity index of the soil in percentage, FI is the average annual freezing index in °F. $days$, and $Precip$ is average annual rainfall or precipitation in inches.

The remaining steps are to choose the best solutions (the parent solutions) for mating—which is the combination of crossover and mutation—and repeat the whole process until the specified number of iterations is reached.

OPTIMIZATION MODEL

Parameters

Parameters are the "constants" of the optimization model that are not decided but are fed into the model beforehand. These include any quantities other than the decision variables. The values of these parameters were chosen based on typical values to make the results and the following conclusion applicable for typical cross-sections.

In the optimization model used in this study, few parameters were used directly, but the previous steps had many constraints and assumptions needed to calculate the fitness value (the objective value). The model was solved for four varying section cases. The sections can be described using the following attributes:

- HMA thickness: Either a thick section (HMA thickness of 11 in) or a thin section (HMA thickness of 4 in).
- Strong and weak HMA sections: See Figure 3 for further explanation.

Thick and thin sections had an assumed traffic of 5,000 and 1,000 trucks per day, respectively. The truck load is described in Figure 37. The speed used in the analysis was 70 mph. Relatively low speeds may be inappropriate for truck platooning. Other corresponding parameters can be found in Table 1. The time span taken for the objective functions in all cases is five years, which is long enough to show the trend in the damage function, but not too long to consider maintenance.

Decision Variables

The decision variables are the quantities to be controlled to get the best out of the system being optimized. The decision variables are the sub-lane placements within the lane. These are called (symbolically):

- x_1: Where to place the first sub-lane.
- x_2: Where to place the second sub-lane.
- x_3: Where to place the third sub-lane.

It is worth noting that because of the assumption of symmetry in the expected damage calculation and the assumption of always utilizing a central sub-lane, a maximum of three decision variables are needed to locate the sub-lane positions. To elaborate on the second assumption (central sub-lane), it was assumed that a fixed proportion of the traffic is set to be on the center of the lane having (1/*n*) of the total traffic, where *n* is the number of sub-lanes. One, two, and three decision variables are needed in the cases of three, five, and seven sub-lanes, respectively.

Model Formulation

The description of the equations/inequalities is as follows. Figure 51 is the objective function. The objective function is what is sought to be minimized (as in this case) or maximized. The function to be minimized is a form of damage function (rutting, cracking, or IRI) of the platoons' lateral position. The inequality in Figure 52 restricts the sub-lane location variables to be within ±18 in of the center of the lane, while the inequality in Figure 53 restricts the sub-lanes to be greater than ±1 in from the center of the range. The inequality in Figure 54 is the variable-type constraints.

$$\min damage\ (x_1, x_2, x_3)$$

Figure 48. Equation. Objective function.

$$s.t. x_1, x_2, x_3 \leq 18$$

Figure 49. Inequality. Sub-lane position constraint—upper limit.

$$x_1, x_2, x_3 \geq 1$$

Figure 50. Inequality. Sub-lane position constraint—lower limit.

$$x_1, x_2, x_3 \in \mathbb{R}^+$$

Figure 51. Inequality. Variable type constraints.

RESULTS

A Python script was used to evaluate the problem based on the open source "genetic algorithm" library. This library gives the choice of whether the decision variables (variables whose values are chosen) are integers (usually binary—0 or 1) or real. As described in the "Decision Variables" section, the decision variables in this problem were all real.

The parameters used in the genetic algorithms are the default ones in the library, as follows:

- Max number of iterations: 100
- Solutions per iteration:100
- Mutation probability: 0.1
- Elite ratio: 0.01
- Crossover probability: 0.5
- Parents portion: 0.3
- Crossover type: uniform
- Maximum number of iterations without improvement: unlimited

Numerical Results

Four HMA sections were used for optimization—thick strong, thick weak, thin strong, and thin weak—referred to as cases one, two, three, and four, respectively. The results were as follows.

Thick, Strong HMA

As mentioned in the "Model Formulation" section, rutting, fatigue cracking, and IRI were minimized separately; the results of which are shown below.

Figure 55 presents the rutting results for three sub-lanes with thick and strong HMA. The genetic algorithm seems to have converged quickly in Figure 55-A. After several iterations, the algorithm reached an objective value of less than 0.238 in, which is almost the best-found solution. (There was not significant improvement achieved after that point.) Although a genetic algorithm has no guarantee on when it will reach optimality, it seems that 100 iterations are enough to approach the global optimum, so each iteration had 100 solutions.

Figure 55-B depicts the best-found solution. The probability distribution should have a probability density of 1/3 in the ranges of ([−19.73, −17.73], [−1,1], [17.73,19.73] in). In other words, for a specific long-term period, one-third of the platoon using the lane should be directed to use each of the three sub-lanes.

As to the accuracy of the sub-lanes and trucks' ability to maintain their positions within inches, Wong et al. (2019) studied the accuracy of estimating autonomous vehicle localization systems. The study used 2D geographic information to measure this localization error. They reported that 69.8% of localization error can be within 1 inch and 87.4% can be within 2 inches. According to the same study, localization in autonomous vehicles takes place as a result of a system of a positioning system—like global navigation satellite systems (GNSS)—and a few other tools and systems including light

detection and ranging (LiDAR), cameras, and other examples. Incorporating systems such as network real time kinematic (N-RTK) GPS may lead to achieving even better accuracies (Stephenson, 2016).

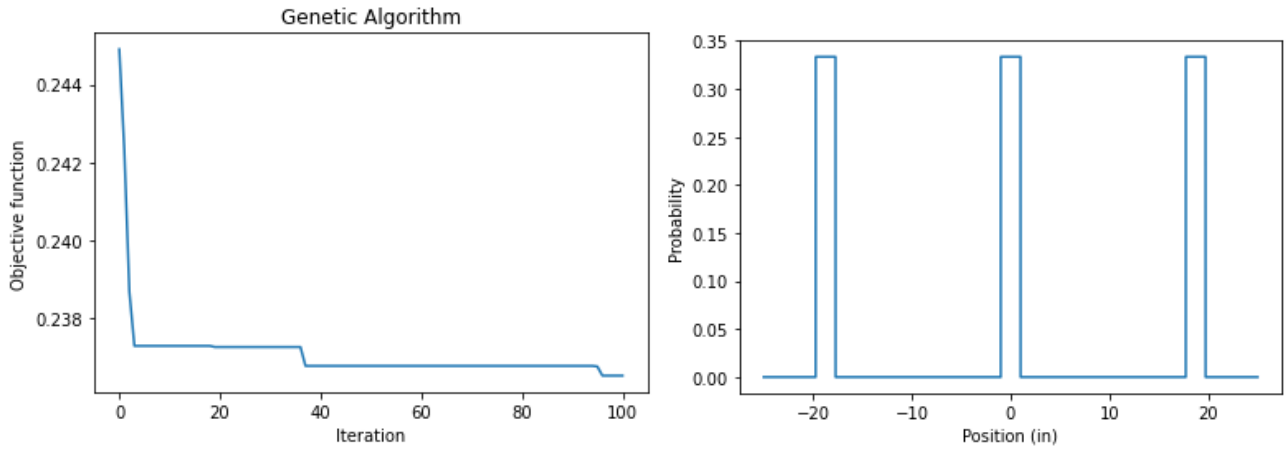

A. Convergence of rutting minimization B. Best-found distribution of the traffic

Figure 52. Graph. Rutting results for case one—three sub-lanes.

The results for cracking and IRI minimization gave the same indication and similar numerical values. Table 7 presents a summary of the results. Although the damage values vary slightly, the takeaway is the same: the left-hand and right-hand sub-lanes should be pushed to the ends of the possible range. The variabilities in the damage values may be due to one of two reasons. First, the randomness inherent in both the expected strain calculation process and the genetic algorithm may play a role in showing differences in IRI, cracking, or rutting between the cases of different objective functions. The second reason is due to the objective function, as the specific damage value may be pushed a little lower than in the other cases. However, these differences are minor and considered negligible. The three objective cases can be said to give, at least practically, the same scenario.

Table 7. Summary of the Results of Case One—Three Sub-lanes

Objective Function	Rutting (in)	Cracking (%)	IRI (in/mi)	Sub-lane 1	Sub-lane 2	Sub-lane 3
Rutting	0.24	0.08	78.9	[−19.73, −17.73]	[−1, 1]	[17.73, 19.73]
Cracking	0.24	0.08	78.6	[−19.98, −17.98]	[−1, 1]	[17.98, 19.98]
IRI	0.25	0.08	78.6	[−19.63, −17.63]	[−1, 1]	[17.63, 19.63]

For the five sub-lanes, rutting and fatigue cracking gave similar best-found distributions. However, when IRI was minimized, it gave a solution in which all the probabilities (other than that in the center) were pushed toward the end of the possible range. Table 8 summarizes the results of case one in the five sub-lane scheme.

Table 8. Summary of the Results of Case One—Five Sub-lanes

Objective Function	Rutting (in)	Cracking (%)	IRI (in/mi)	Sub-lane 1	Sub-lane 2	Sub-lane 3	Sub-lane 4	Sub-lane 5
Rutting	0.28	0.09	80.0	[−19.37, −17.37]	[−10.39, −8.39]	[−1, 1]	[8.39, 10.39]	[17.37, 19.37]
Cracking	0.24	0.09	78.9	[−19.75, −17.75]	[−11.9, −9.9]	[−1, 1]	[9.9, 11.9]	[17.75, 19.75]
IRI	0.24	0.09	78.7	[−19.93, −17.93]	[−19.62, −17.62]	[−1, 1]	[17.62, 19.62]	[17.93, 19.93]

These results can be explained as follows. It is possible that multiple optima exist for the same function. That is, many solutions give the same minimum value of the function. For example, although the distribution shown in the second row of Table 8 is believed to minimize cracking, another solution (shown in the third row) gives a very similar cracking function. This brings up the following questions: is the lateral position important, and how much does it impact damage? To answer these questions, it is important to understand the case of distributed traffic against human-driven patterns (completely normally distributed, with a somewhat large standard deviation) and channelized traffic.

In the case of human-driven traffic, the values of estimated fatigue cracking, rutting, and IRI were 0.14%, 0.28 in, and 80.4 in/mi, respectively. A cracking increase of 56% is noted. Rutting, on the other hand, has a modest increase that could be considered within the algorithm variability (Table 8). The same can be noted for IRI.

For channelized traffic (all traffic goes through the center sub-lane), the results show a major difference. Fatigue cracking reaches a value of 0.23%, approximately a 150% increase from the best-found value. Rutting reaches 0.33 in, with an expected increase because of channelization. However, IRI does not show the same trend. The value reaches 82.5 in/mi; however, it can be argued that this increase is minimal. This is because the resulting value is the IRI after five years of an initial value of 60 in/mi. The increase is 22.5 in/mi compared to around 18.7 in/mi in the best-found solution to minimize IRI. This can be attributable to the way IRI is calculated. It is a function of traffic-related damage (rutting and fatigue cracking) as well as non-load-related damage, which does not show a difference to the given loading pattern.

Table 9 presents case one's results with seven sub-lanes.

Table 9. Summary of the Results of Case One—Seven Sub-lanes

Objective Function	Rut (in)	Crack (%)	IRI (in/mi)	Sub-lane 1	Sub-lane 2	Sub-lane 3	Sub-lane 4	Sub-lane 5	Sub-lane 6	Sub-lane 7
Min Rut	0.23	0.09	78.5	[19.97, −17.97]	[19.3, −17.32]	[−11.7, −9.7]	[−1, 1]	[9.7, 11.7]	[17.32, 19.32]	[17.97, 19.97]
Min Crack	0.25	0.08	79	[−19.99, −17.99	[−19.85, −17.85]	[−7.89, −5.89]	[−1, 1]	[5.89, 7.89]	[17.85, 19.85]	[17.99, 19.99]
Min IRI	0.24	0.09	78.5	[−19.94, −17.94]	[−15.53, −13.53]	[−9.22, −7.22]	[−1, 1]	[7.22, 9.22]	[13.53, 15.53]	[17.94, 19.94]

The differences between cases with three, five, and seven sub-lanes are negligible; the variability is barely noticeable. Nevertheless, note that this case is for a thick and strong HMA section. Thus, damage values may not be sensitive to the exact location of the sub-lanes, but there is still a need to distribute the traffic by sub-lanes because it showed good improvement compared to channelized and even human-driven patterns.

The main takeaways of this case are as follows:

- The end damage values in the three cases appear to be similar, whether rutting, fatigue cracking, or IRI is minimized.
- More than one distribution pattern may give the same value.
- Although many distributions give similar results, this is not to be confused with human-driven or channelized traffic. Following a channelized scheme, the estimated cracking reaches a value approximately 150% that of optimized traffic. For human-driven traffic, the increase is around 50%. Rutting and IRI show similar, but less severe, trends.

Thick, Weak HMA

Figure 56 presents the rutting results for three sub-lanes with thick and weak HMA. The results are similar to those in case one. The sub-lanes should be pushed to the outer sides of the range ([−19.73, −17.73], [−1, 1], [17.73, 19.73] in).

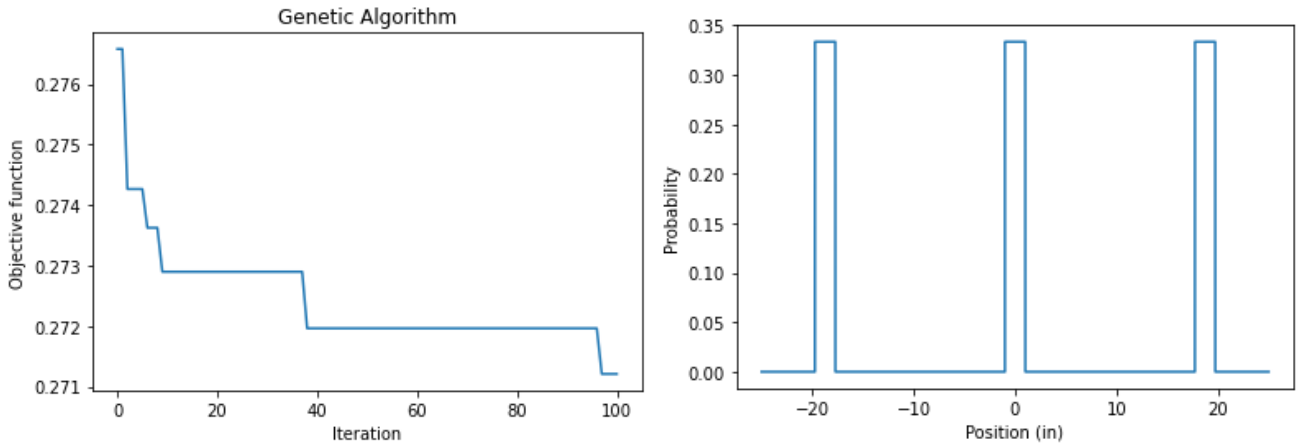

A. Convergence of rutting minimization B. Best-found distribution of the traffic

Figure 53. Graph. Rutting results for case two—three sub-lanes.

Table 10 presents case two's results for three sub-lanes. As in case one, the best-found solution pushes the sub-lanes toward the end of the lane. Minimizing any of the three objective functions still resulted in damage values similar to the other damage functions.

Table 10. Summary of the Results of Case Two—Three Sub-lanes

Objective Function	Rutting (in)	Cracking (%)	IRI (in/mi)	Sub-lane 1	Sub-lane 2	Sub-lane 3
Rutting	0.27	0.29	80.4	[−19.73, −17.73]	[−1, 1]	[17.73, 19.73]
Cracking	0.28	0.28	80.3	[−20, −18]	[−1, 1]	[18, 20]
IRI	0.28	0.29	80.0	[−19.87, −17.87]	[−1, 1]	[17.87, 19.87]

Table 11 presents case two's results for five sub-lanes.

Table 11. Summary of the Results of Case Two—Five Sub-lanes

Objective Function	Rutting (in)	Cracking (%)	IRI (in/mi)	Sub-lane 1	Sub-lane 2	Sub-lane 3	Sub-lane 4	Sub-lane 5
Rutting	0.27	0.33	80.5	[−19.61, −17.61]	[−11.1, −9.1]	[−1, 1]	[9.1, 11.1]	[17.61, 19.61]
Cracking	0.29	0.32	80.7	[−19.8, −17.8]	[−11.64, −9.64]	[−1, 1]	[9.64, 11.64]	[17.8, 19.8]
IRI	0.28	0.33	80.2	[−19.46, −17.46]	[−10.73, −8.73]	[−1, 1]	[8.73, 10.73]	[17.46, 19.46]

The damage minimization here calls for a rather dispersed distribution. Figure 57 presents an example best-found distribution of fatigue cracking.

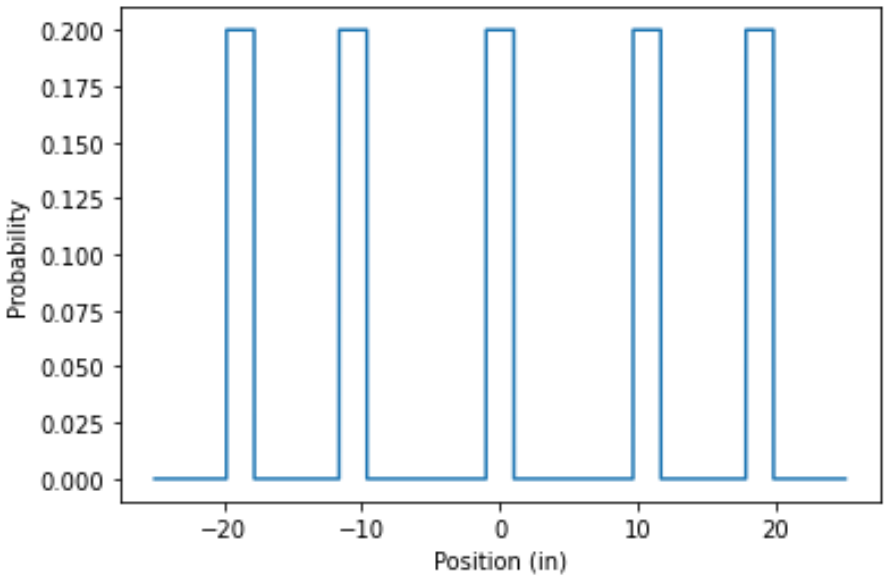

Figure 54. Graph. Best-found distribution of the traffic for fatigue cracking—five sub-lanes.

Table 12 presents case two's results for the optimization of damage with seven sub-lanes.

Table 12. Summary of the Results of Case Two—Seven Sub-lanes

Objective Function	Rut (in)	Crack (%)	IRI (in/mi)	Sub-lane 1	Sub-lane 2	Sub-lane 3	Sub-lane 4	Sub-lane 5	Sub-lane 6	Sub-lane 7
Rutting	0.26	0.33	80.0	[−19.93, −17.93]	[−19.78, −17.78]	[−13.13, −11.13]	[−1, 1]	[11.13, 13.13]	[17.78, 19.78]	[17.93, 19.93]
Cracking	0.29	0.30	80.7	[−19.6, −17.6	[−19.5, −17.5]	[−7.7, −5.7]	[−1, 1]	[5.7, 7.7]	[17.5, 19.5]	[17.6, 19.6]
IRI	0.27	0.33	79.9	[−19.96, −17.96]	[−14.87, −12.87]	[−9.15, −7.15]	[−1, 1]	[7.15, 9.15]	[12.87, 14.87]	[17.96, 19.96]

Similar to case one, differences in the individual function values are insignificant. The solutions differ a little between the three cases. For example, to minimize cracking, the last two sub-lanes from each direction should almost intersect. The probability density should be as presented in Figure 58. The probability at the two outer sub-lanes should be 2/7. The three inner sub-lanes should still have a probability of 1/7.

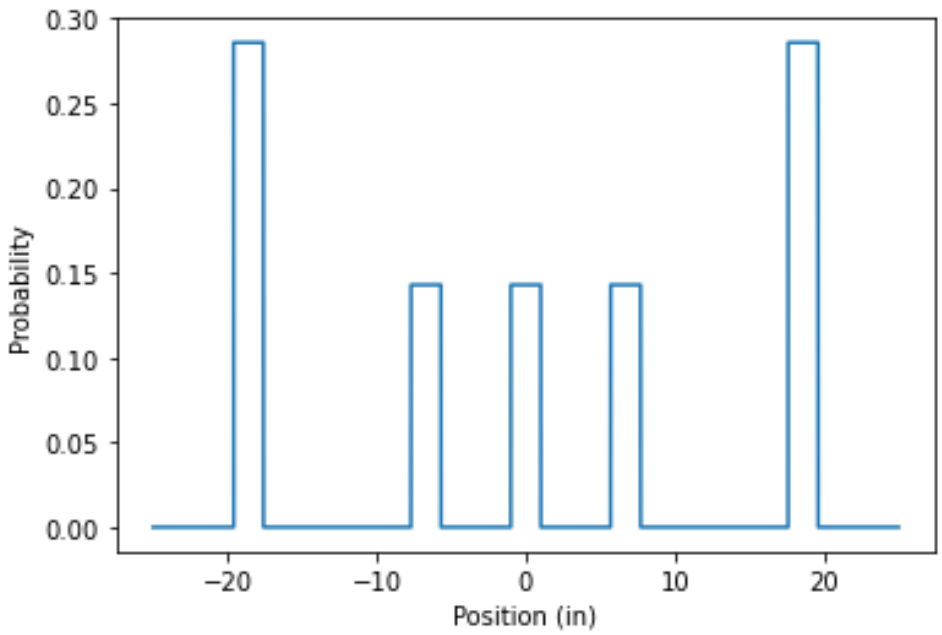

Figure 55. Graph. Best-found distribution of the traffic for fatigue cracking—seven sub-lanes.

Although not significantly different, the case with three sub-lanes shows slightly less damage than those of five and seven sub-lanes. Again, the various distributions may not produce different results because the section is thick. Nonetheless, it should have different results than that of human-driven and channelized traffic. For human-driven (normally distributed) trucks, the damage is 0.50%, 0.32 in, and 82.2 in/mi for fatigue cracking, rutting, and IRI, respectively. For channelized traffic, the results are 0.81%, 0.39 in, and 84.9 in/mi for cracking, rutting, and IRI, respectively. The outcomes were similar to those of case one. The percent increase in damage was, however, greater when the schemes of normally distributed and channelized traffic were chosen.

Thin, Strong HMA

Table 13 presents case three's damage minimization results for three sub-lanes with thin and strong HMA. The results show no difference from the two previous cases. The sub-lanes should be pushed all the way to the end of the range.

Table 13. Summary of the Results of Case Three—Three Sub-lanes

Objective Function	Rutting (in)	Cracking (%)	IRI (in/mi)	Sub-lane 1	Sub-lane 2	Sub-lane 3
Rutting	0.44	0.18	89.3	[−19.87, −17.87]	[−1, 1]	[17.87, 19.87]
Cracking	0.44	0.18	89.3	[−19.99, −17.99]	[−1, 1]	[17.99, 19.99]
IRI	0.44	0.18	89.1	[−19.85, −17.85]	[−1, 1]	[17.85, 19.85]

Table 14 presents case three's optimization results with five sub-lanes.

Table 14. Summary of the Results of Case Three—Five Sub-lanes

Objective Function	Rutting (in)	Cracking (%)	IRI (in/mi)	Sub-lane 1	Sub-lane 2	Sub-lane 3	Sub-lane 4	Sub-lane 5
Rutting	0.43	0.21	89.0	[−19.84, −17.84]	[−19.39, −17.39]	[−1, 1]	[17.39, 19.39]	[17.84, 19.84]
Cracking	0.45	0.21	89.4	[−19.98, −17.98]	[−15.64, −13.64]	[−1, 1]	[13.64, 15.64]	[17.98, 19.98]
IRI	0.44	0.21	89.1	[−19.67, −17.67]	[−19.32, −17.32]	[−1, 1]	[17.32, 19.32]	[17.67, 19.67]

Table 15 presents case three's optimization results for seven sub-lanes.

Table 15. Summary of the Results of Case Three—Seven Sub-lanes

Objective Function	Rut (in)	Crack (%)	IRI (in/mi)	Sub-lane 1	Sub-lane 2	Sub-lane 3	Sub-lane 4	Sub-lane 5	Sub-lane 6	Sub-lane 7
Rutting	0.44	0.23	89.0	[−19.59, −17.59]	[−18, −16]	[−16.13, −14.13]	[−1, 1]	[14.13, 16.13]	[16, 18]	[17.59, 19.59]
Cracking	0.46	0.2	89.8	[−19.84, −17.84]	[−19.78, −17.78]	[−7.25, −5.25]	[−1, 1]	[5.25, 7.25]	[17.78, 19.78]	[17.84, 19.84]
IRI	0.44	0.23	88.9	[−19.4, −17.4]	[−18.81, −16.81]	[−16.07, −14.07]	[−1, 1]	[14.07, 16.07]	[16.81, 18.81]	[17.4, 19.4]

It is noteworthy that five and seven sub-lane distributions show slightly more damage than those of three sub-lanes. The normally distributed traffic and channelized traffic give estimated cracking, rutting, and IRI of 0.37%, 0.52 in, 92.5 in/mi and 0.61%, 0.59 in, 95.2 in/mi, respectively. Any of the given optimal distributions would produce significantly better results.

Thin, Weak HMA

Table 16 presents case four's optimization results for three sub-lanes with thin and weak HMA.

Table 16. Summary of the Results of Case Four—Three Sub-lanes

Objective Function	Rutting (in)	Cracking (%)	IRI (in/mi)	Sub-lane 1	Sub-lane 2	Sub-lane 3
Rutting	0.50	0.59	92.2	[−19.95, −17.95]	[−1, 1]	[17.95, 19.94]
Cracking	0.51	0.59	92.0	[−20, −18]	[−1, 1]	[18, 20]
IRI	0.51	0.59	91.8	[−20, −18]	[−1, 1]	[18, 20]

Table 17 presents case four's damage optimization results when five sub-lanes are assumed.

Table 17. Summary of the Results of Case Four—Five Sub-lanes

Objective Function	Rutting (in)	Cracking (%)	IRI (in/mi)	Sub-lane 1	Sub-lane 2	Sub-lane 3	Sub-lane 4	Sub-lane 5
Rutting	0.50	0.71	92.1	[−18.71, −16.71]	[−18.17, −16.17]	[−1, 1]	[19.17, 18.17]	[16.71, 18.71]
Cracking	0.50	0.69	91.6	[−19.97, −17.97]	[−19.96, −17.96]	[−1, 1]	[17.96, 19.96]	[17.97, 19.97]
IRI	0.50	0.70	91.7	[−19.41, −17.41]	[−18.84, −16.84]	[−1, 1]	[16.84, 18.84]	[17.41, 19.41]

Table 18 presents case four's optimization results for seven sub-lanes.

Table 18. Summary of the Results of Case Four—Seven Sub-lanes

Objective Function	Rut (in)	Crack (%)	IRI (in/mi)	Sub-lane 1	Sub-lane 2	Sub-lane 3	Sub-lane 4	Sub-lane 5	Sub-lane 6	Sub-lane 7
Rutting	0.50	0.75	91.9	[−19.49, −17.49]	[−18.73, −16.73]	[−14.36, −12.36]	[−1, 1]	[14.13, 16.13]	[16, 18]	[17.59, 19.59]
Cracking	0.53	0.68	92.9	[−19.75, −17.75]	[−19.66, −17.66]	[−6.83, −4.83]	[−1, 1]	[4.83, 6.83]	[17.66, 19.66]	[17.75, 19.75]
IRI	0.50	0.75	91.7	[−18.92, −16.92]	[−18.78, −16.78]	[−16.24, −14.24]	[−1, 1]	[14.24, 16.24]	[16.78, 18.78]	[16.92, 18.92]

Again, the results of three sub-lanes were better than those in the cases of five and seven sub-lanes. The damage results in normally distributed (human-driven) traffic were 1.18% cracking, 0.61 in rutting, and 96.3 in/mi IRI. For channelized traffic, the results were 1.99% cracking, 0.70 in rutting, and 100.2 in/mi IRI. The difference from optimized damage is formidable and calls for dispersion of the traffic.

The outcome of the above cases can be summarized as follows:

- Different optimized configurations give close damage results for all the sections. In other words, multiple configurations can be described as (near) optimal. However, this is not to be

confused with either channelized or normally distributed (human-driven) traffic. For all four cases, optimized traffic was better (and sometimes much better) than both channelized and normally distributed traffic. This may suggest that the damage is not sensitive to specific values of distribution as long as the traffic is being distributed in intervals. Any of the optima schemes may be used interchangeably.

- The less stiff the section (either thinner or weaker), the higher the impact of optimized traffic on damage compared to a nonoptimized traffic pattern. Figure 59 depicts these variations for rutting, cracking, and IRI. The trend shows that the optimized scenario is better than human driven, which, in turn, is better than channelized. The differences are more subtle in case one because of its stiffness but are clearer in case four.

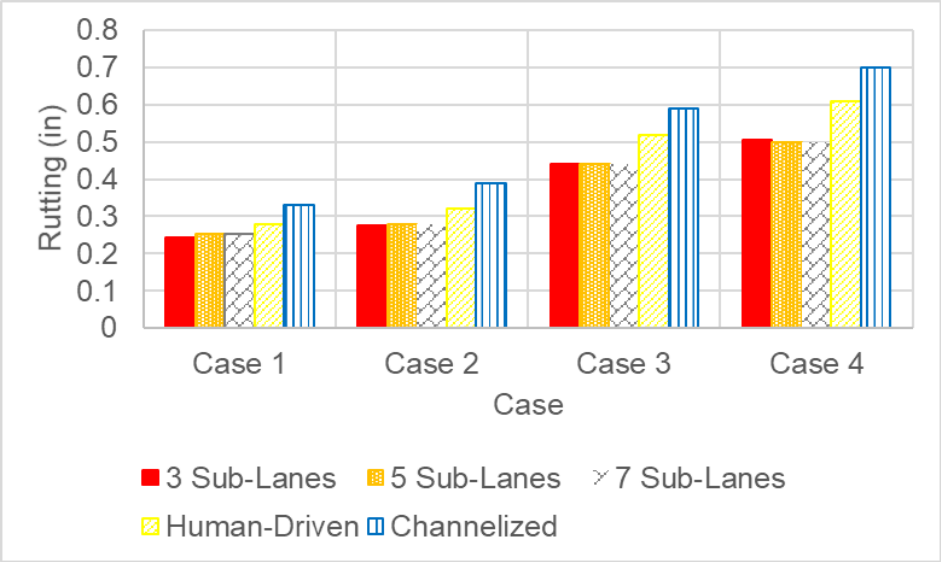

A. Rutting of the four cases under five schemes

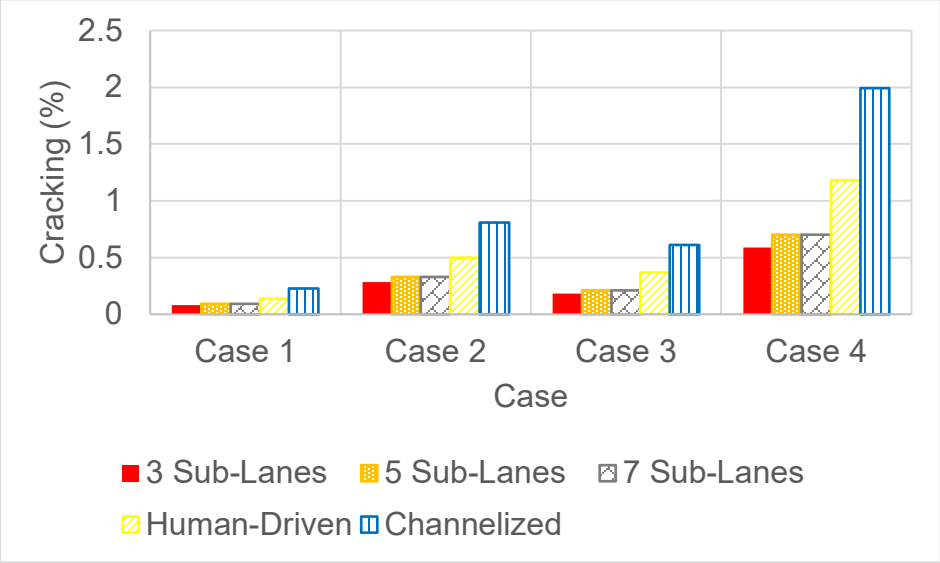

B. Fatigue cracking of the four cases under five schemes

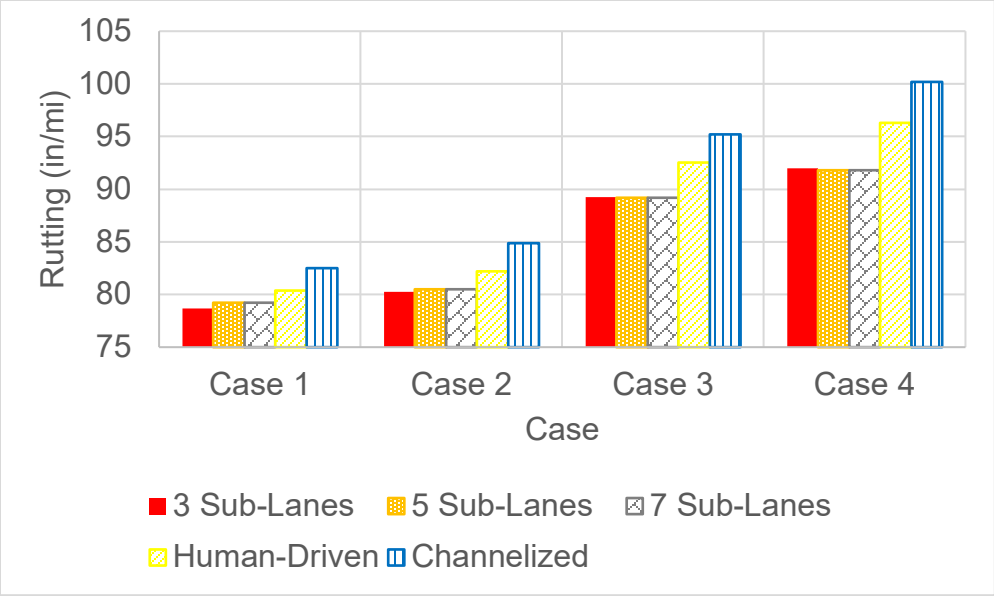

C. IRI of the four cases under five schemes

Figure 56. Chart. Five-year (a) rutting, (b) fatigue cracking, and (c) IRI of the four sections under five schemes.

In summary, channelized traffic, for example, may have adverse effects on damage—especially for thinner and weaker sections (see the impact on case four, which is even more stressed out in cracking). In the less stiff sections, the three sub-lane configuration shows better results than those for five and seven sub-lanes. In contrast, for stiffer sections, the impact appears to be small enough to be negligible. There is no assertive trend in the distribution of sub-lanes based on the specific damage to be minimized.

CHAPTER 5: ECONOMIC AND ENVIRONMENTAL IMPACT OF PLATOONING

LIFE CYCLE COST ANALYSIS

Life cycle cost analysis (LCCA) is an analysis technique to evaluate the long-term economic benefits of different alternatives (USDOT, 2002). Agency and user costs are two main types of costs considered in pavement LCCA. In this study, agency and user costs were computed using the cost analysis database developed by the Illinois Center for Transportation.

Agency costs are the costs incurred by the owner agency and include the initial construction and maintenance costs. Material-, labor-, and equipment-related costs are part of agency costs, and they directly affect the owner agency. Quantification of these costs are rather straightforward because these costs are usually well documented in contracts as unit processes or pay items, and their cost are listed. The uncertainty in the agency costs are due to future maintenance and rehabilitation activities.

User costs are costs to the traveling public on the pavement section that the owner agency is responsible for maintaining. In general, user costs include vehicle-operating costs, travel delays, crashes, and emissions. There are also some other items difficult to monetize such as the comfort of the user, local economic impacts of a specific project, and noise. These costs are usually ignored because they are difficult to quantify.

Agency Costs

In this study, agency costs include material- and equipment-related costs resulting from the initial pavement construction and pavement maintenance. Four types of pavement structures are applied on a 12 ft wide and 1 mi long lane section (see Figure 60). Structures I and II are considered thick pavements, while structures III and IV are considered thin pavements. Stone-matrix asphalt (SMA) is used in the surface layer of structures II and IV. The initial construction costs of the four pavement sections are computed by multiplying the unit cost of related pay items and the quantity of each pay item (Okte et al., 2019). Table 19 presents the initial construction costs.

Pavement sections of structures I and II are assumed to load 5,000 trucks daily, while sections of structures III and IV are assumed to load 1,000 trucks daily. Four traffic schemes are applied for each section (see Figure 61). In scheme A (channelized truck platooning), all trucks are in a platoon and are traveling at the lane's center. In scheme B (human-driven trucks), all trucks are driven by humans and are not in a platoon. In scheme C (mixed trucks), half of the trucks are driven by humans and half are in a platoon. The centerline of the trucks is between [−1, 1] (in). In scheme D (optimized platoon design), all trucks are in a platoon. The centerline of 34% of the trucks is between [−18, −16] (in), 12% is between [−10, −8] (in), 8% is between [−1, 1] (in), 12% is between [8, 10] (in), and 34% is between [16, 18] (in).

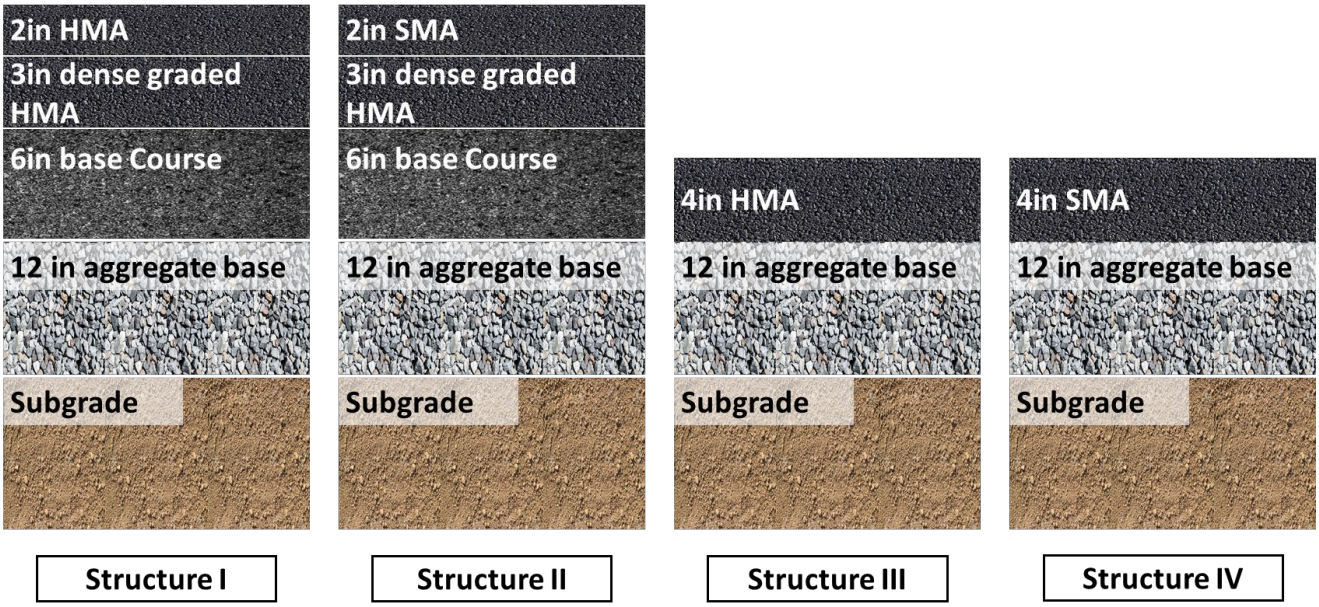

Figure 57. Illustration. Four types of pavement structures.

Table 19. Initial Construction Costs of Four Pavement Sections

Pay Item	Cost per unit	Structure I	Structure II	Structure III	Structure IV
		Cost (2020$)	Cost (2020$)	Cost (2020$)	Cost (2020$)
12 in aggregate base layer	30 (2006$/CUYD)	91,604	91,604	91,604	91,604
6 in HMA base course layer	20 (2006$/SQYD)	183,205	183,205	–	–
3 in dense-graded HMA layer	70 (2006$/TON)	109,380	109,380	–	–
2 in HMA layer	70 (2011$/TON)	65,354	–	–	–
2 in SMA layer	93 (2006$/TON)	–	96,880	–	–
4 in HMA layer	70 (2011$/TON)	–	–	130,708	–
4 in SMA layer	93 (2006$/TON)	–	–	–	193,759
Total cost		**449,543**	**481,069**	**222,312**	**285,363**

The maintenance activities were conducted under three scenarios. In scenario I, cold milling and HMA overlay were applied when fatigue cracking, rut depth, or roughness values reached their corresponding thresholds. The HMA overlay thickness was the same as the initial HMA surface layer thickness. The threshold values to apply pavement maintenance activities are 20% for fatigue cracking, 0.5 in for rutting depth in structures I and II, 0.75 in for rutting depth in structures III and IV, and 150 in/mi for roughness (USDOT, 2013). In scenario II, the same maintenance schedule was applied to each structure. The cold milling and HMA overlay would be applied at years 10, 20, 30, and 40. In scenario III, only the channelized scheme (scheme A) was considered for each structure. Instead of applying cold milling and HMA overlay, wheelpath repair was applied to solve damage caused by channelized platoons. Although such remediation has been successfully applied in some European countries, it is expected to be difficult to apply in Illinois. However, it was included for analysis purposes.

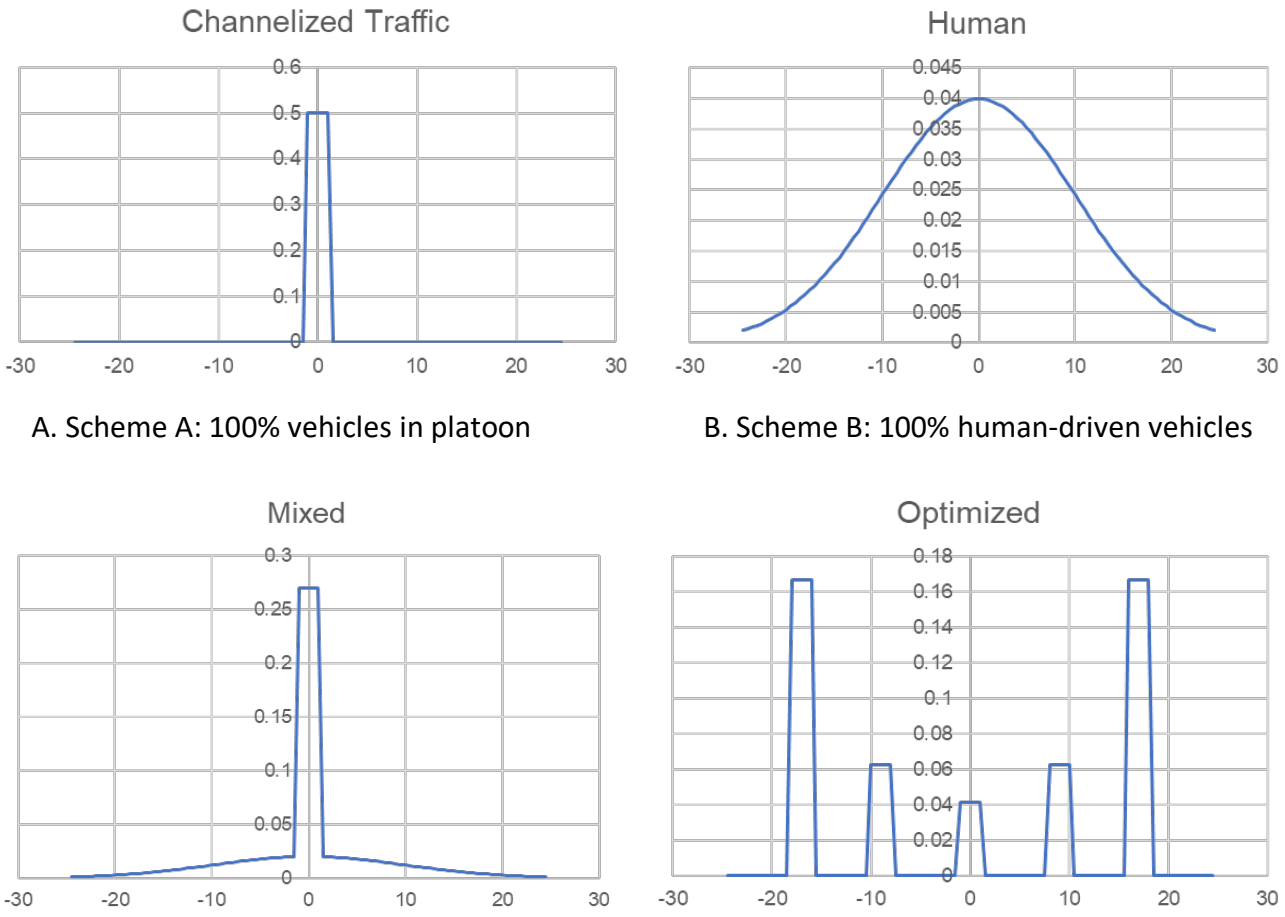

A. Scheme A: 100% vehicles in platoon

B. Scheme B: 100% human-driven vehicles

C. Scheme C: Mix of human driven and platoon

D. Scheme D: Optimized design of platoon trucks

Figure 58. Graph. Four traffic schemes.

Under these four traffic schemes, maintenance costs and user costs are computed for each scenario.

Scenario I

Cold milling and HMA overlay were applied in scenario I when fatigue cracking, rutting, or roughness reached the corresponding thresholds. Note that the rut depth threshold is 0.5 in and 0.75 in for structures I and II and structures III and IV, respectively. As illustrated in Chapters 2 and 3, fatigue cracking and rutting of the four pavement sections can be simulated under four traffic schemes. Figure 62 and Figure 63 present fatigue cracking and rutting results, respectively. The IRI progression of each structure can also be computed using the recurrent neural network explained in Chapter 3. However, the fatigue cracking and IRI values were relatively low, and the threshold was reached after a relatively long service time. The maintenance schedule was determined by the rut depth progression. Tables 20 and 21 present the maintenance schedule and maintenance costs, respectively, of scenario I.

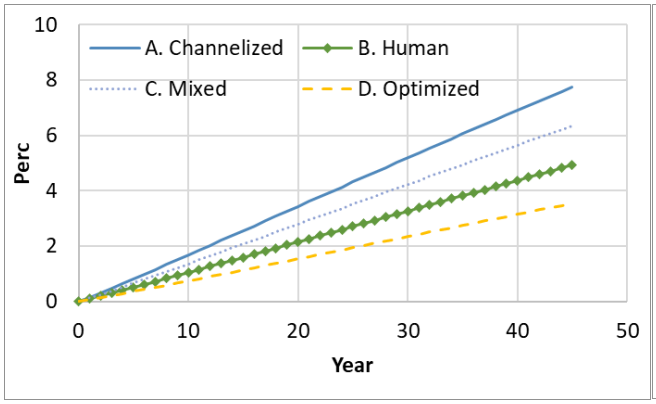

A. Fatigue cracking (%) for structure I

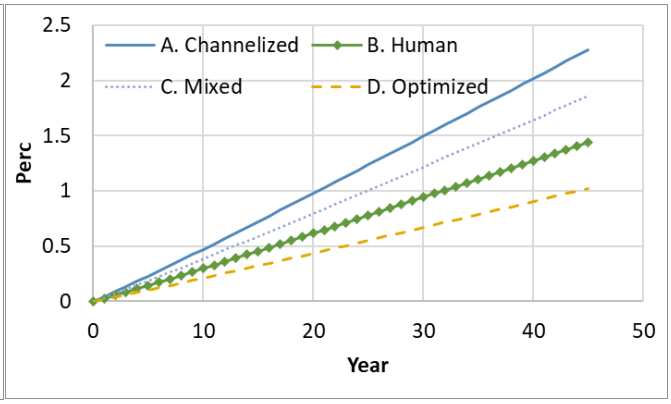

B. Fatigue cracking (%) for structure II

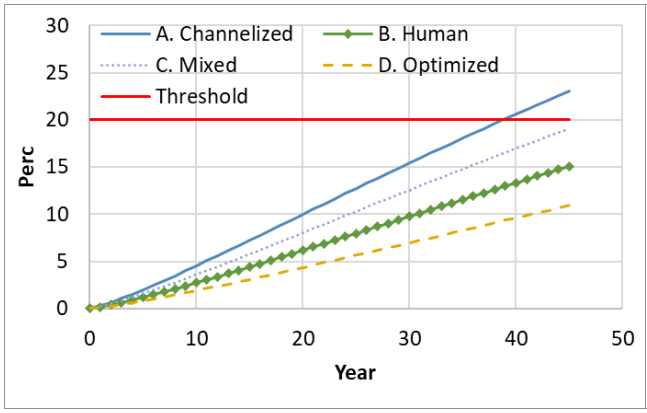

C. Fatigue cracking (%) for structure III

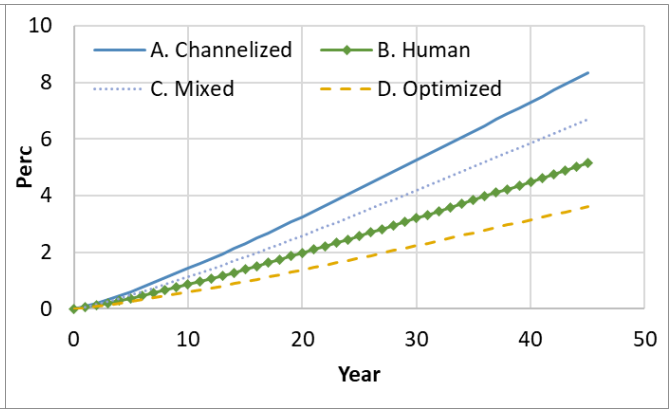

D. Fatigue cracking (%) for structure IV

Figure 59. Graph. Fatigue cracking (%) for each structure under four traffic schemes.

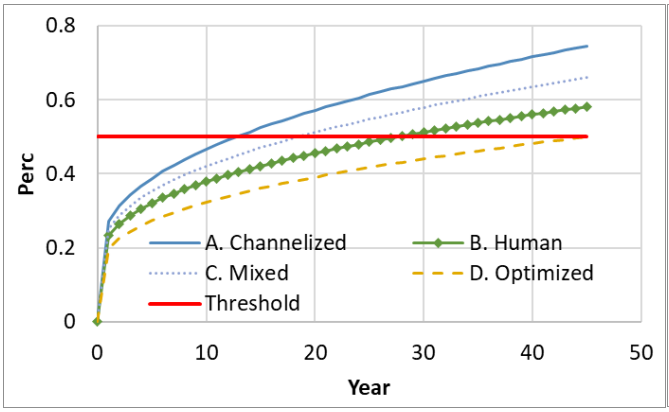

A. Rut depth (in) for structure I

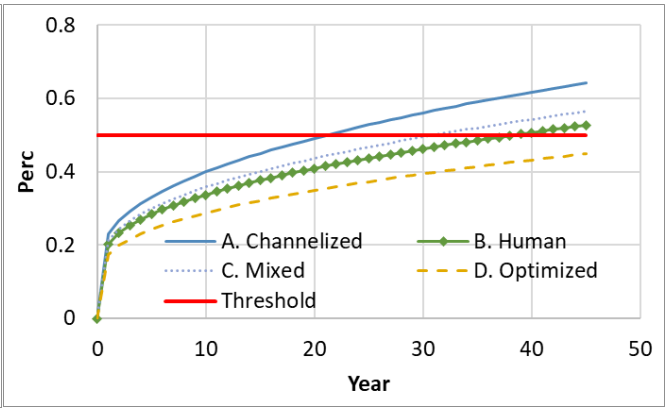

B. Rut depth (in) for structure II

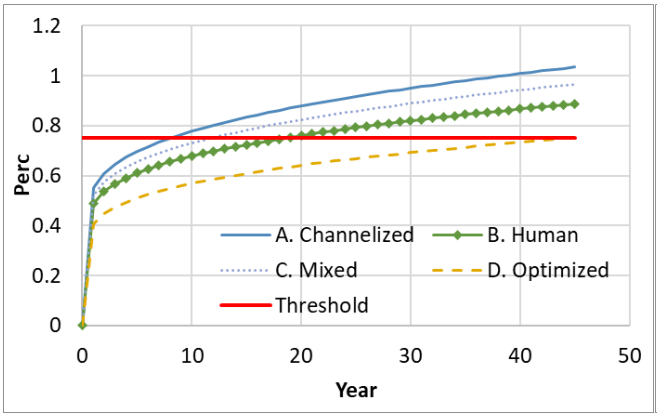

C. Rut depth (in) for structure III

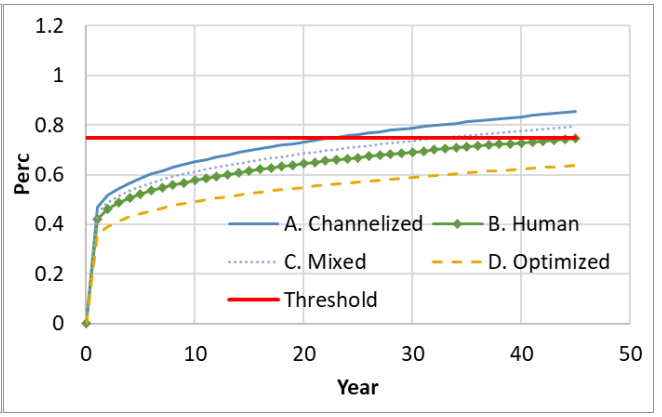

D. Rut depth (in) for structure IV

Figure 60. Graph. Rut depth (in) for each structure under four traffic schemes.

Table 20. Maintenance Schedule of Four Structures Sections under Four Traffic Schemes

Structure Type	Structure I				Structure II				Structure III				Structure IV			
Traffic Scheme	**A**	**B**	**C**	**D**	**A**	**B**	**C**	**D**	**A**	**B**	**C**	**D**	**A**	**B**	**C**	**D**
Maintenance Year	13, 26, 39	28	19, 38	–	22, 44	39	31	–	9, 18, 27, 36	19, 38	12, 24, 36	–	23	–	34	–

Table 21. Maintenance Costs (2020$) of Scenario I

Structure Type	Scheme A	Scheme B	Scheme C	Scheme D
Structure I	142,042	56,290	145,625	0
Structure II	74,338	40,665	65,045	0
Structure III	209,020	115,331	250,160	0
Structure IV	49,282	0	59,525	0

Scenario II

The same maintenance schedule is applied to each structure. Therefore, the maintenance costs for each traffic scheme (schemes A, B, C, and D in Figure 61) of the same structure would be the same. Cold milling and HMA overlay were applied at years 10, 20, 30, and 40. Table 22 presents the maintenance costs.

Table 22. Maintenance Costs (2020$) of Scenario II

Traffic Scheme	Structure I	Structure II	Structure III	Structure IV
Traffic Scheme A/B/C/D	196,294	259,859	328,069	455,199

Scenario III

For this hypothetical scenario, for the channelized traffic scheme (scheme A), 2 ft wide wheelpath repair was applied to solve the channelized distresses instead of applying cold milling and HMA overlay. The maintenance schedule is the same as scenario I. Table 23 presents the maintenance costs.

Table 23. Maintenance Costs (2020$) of Scenario III

Traffic Scheme	Structure I	Structure II	Structure III	Structure IV
Traffic Scheme A	59,184	30,974	87,092	20,534

User Costs

Two components are considered in computing user costs. The first component is the fuel savings of trucks because of the air drag force reduction when trucks are platooning. The second component is the extra fuel consumption of trucks because of increased pavement roughness.

Fuel Savings of Platooning Trucks

According to the study by Gungor et al. (2020), the energy savings of platooning trucks can be simulated using the function presented in Figure 64. The cross-sectional area of simulated truck is assumed to be 9.49 m^2.

$$cost_{drag}\left(\frac{\$}{VMT}\right) = c_a * \frac{1}{2} * \rho * C_{D,\infty} * v^2 * \sum_{i=1}^{N} R_i$$

Figure 61. Equation. Monetary value per vehicle miles travelled of platooning trucks.

where:

- VMT is the vehicle miles travelled.
- ρ is the air density at 1.225 kg/m^3.

- v is the cruising velocity at 26.8 m/s.
- c_a is a unit converting factor 2.743e-8 L/J based on an engine efficiency of 40% and a typical diesel price of $0.74 per L.
- $C_{D,\infty}$ is the drag coefficient of an isolated truck computed from a developed computational fluid dynamics (CFD) solver.
- R_i is the drag ratio of vehicle *i* in a truck platoon, see Figure 65.

$$R_i(s, \Delta x) = R_L(s) - \sum_{j=1, j\neq i}^{i} \frac{R_L(s) - \hat{R}_{j+1}(\Delta_{j-i}, s)}{R_L(s) - R_T(S)} \Delta R_j$$

Figure 62. Equation. Drag ratio of vehicle *i* in a truck platoon (Gungor et al., 2020).

where:

- $R_L(s)$ and $R_T(S)$ are the field drag coefficients for leading and trailing trucks, respectively, for a two-truck platoon given intervehicle spacing (Zabat et al., 1995).
- $\hat{R}_{j+1}(\Delta_j, s)$ is the drag coefficient of $(j+1)^{th}$ truck obtained from CFD simulations.
- Δ_{j-i} is the lateral distance between the j^{th} and i^{th} trucks.
- *s* is the intervehicle distance between trucks in a platoon.
- ΔR_j is the drag coefficient difference between the $j^{th}$and $(j+1)^{th}$, computed from Zabat et al. (1995), which stays the same after the fourth truck.

The fuel savings of platooning trucks are resulted from the platoon design (the number of trucks in a platoon, the spacing between trucks, and truck volume), as presented in the aforementioned models (Figure 64 and Figure 65). Four types of platoon designs were considered, and the analyses were conducted under two levels of truck volume (1,000 and 5,000 daily trucks), as presented in Table 24. The results demonstrate that platoon design two performed the best. Hence, design two was used in this LCCA and in the life cycle assessment (LCA).

Table 24. Fuel Savings of Platooning Trucks

	Design One	Design Two	Design Three	Design Four
1,000 truck per day				
Spacing (ft)	20	20	60	60
# of truck in a platoon	3	6	3	6
Fuel savings (2020$), $M	0.20	0.27	0.17	0.22
5,000 truck per day				
Spacing (ft)	20	20	60	60
# of truck in a platoon	3	6	3	6
Fuel savings (2020$), $M	1.01	1.37	0.83	1.12

Extra Fuel Cost because of Increased Roughness

In this section, the equation developed by Ziyadi et al. (2018) is used to compute the additional energy consumption because of pavement roughness. The equation presented in Figure 66 computes the energy consumption as a function of other variables (e.g., speed) as well as IRI. To isolate the effect of IRI, this equation should be executed twice with IRI_0 (initial IRI) and IRI_t (IRI at time t). The difference between these two executions provided the additional energy consumption due to the IRI change.

$$E = \frac{p}{v} + (k_a IRI + d_a) + bv + (k_c IRI + d_c)v^2$$

Figure 63. Equation. Estimated energy consumption per mile.

where:

- *E* is estimated energy consumption per mi (KJ/mi).
- *v* is speed (mph).
- k_a, k_c, d_a, d_c, b and p are model coefficients.

Because this computation is only impacted by IRI progression and traffic volume, the results could be summarized for all four structures in Table 25. For scenarios I and III, cases with less frequent maintenance activities resulted in greater extra fuel cost due to higher roughness progression. When the same maintenance schedule is applied for each case, as in scenario II, the optimized traffic scheme (scheme D) always consumes less extra fuel in the use stage.

Table 25. Extra Fuel Cost in Millions of 2020$ Due to Roughness

	Structure I	Structure II	Structure III	Structure IV
Scenario I/III				
Traffic Scheme A	4.46	4.69	1.40	1.43
Traffic Scheme B	4.09	4.26	1.26	1.41
Traffic Scheme C	4.32	3.98	1.20	1.17
Traffic Scheme D	4.72	4.63	1.41	1.24
Scenario II				
Traffic Scheme A	4.11	3.57	1.39	1.16
Traffic Scheme B	3.32	3.04	1.22	1.04
Traffic Scheme C	3.75	3.22	1.30	1.09
Traffic Scheme D	2.86	2.59	1.02	0.88

Life Cycle Cost Analysis Results

The total cost of scenarios I and II was computed by summing up the initial construction, maintenance, and extra fuel costs, and then subtracting the fuel savings due to platoons. Figure 67 and Figure 68 present the cost results. In both scenarios, the user costs of platoon trucks or mixed traffic are lower than those of human-driven trucks for each structure. The major reduction results from fuel savings when trucks are platooning. The benefits of platooning are more significant in scenario II because the same maintenance schedule is applied on each structure. The roughness progression on the same structure is the same under different traffic schemes, which means the reductions in user costs are from the fuel savings of different traffic schemes. In scenario I, platoon scheme D has less agency cost because it does not apply any maintenance activities, while platoon scheme A has the highest agency cost because of its frequent maintenance activities. However, scheme D had more fuel savings because of pavement roughness progression. This trade-off would be balanced for structures III and IV, because they were carrying less traffic and the additional fuel costs due to roughness were less than those of structures I and II. In conclusion, the decision for maintenance schedule is highly impacted by both agency and user costs, while traffic level would have more impact on user cost.

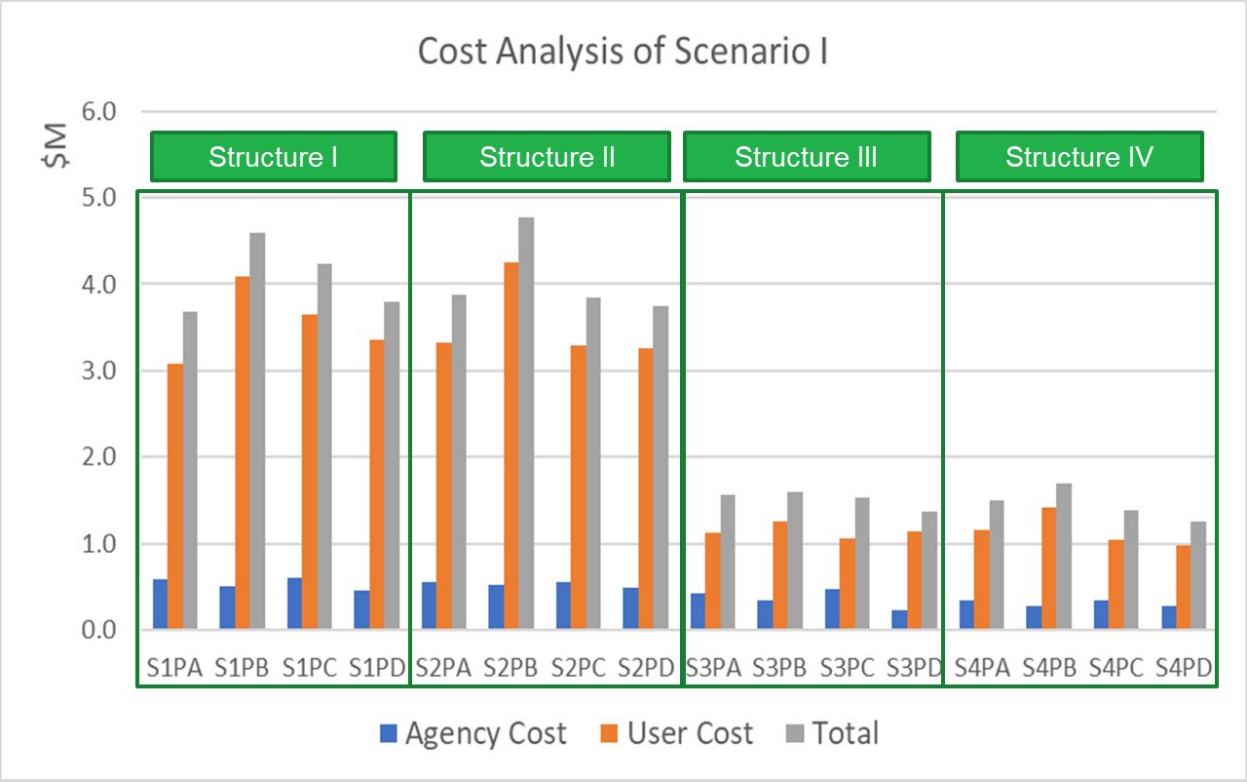

Figure 64. Graph. LCCA of four pavement structures under four platoon schemes (scenario I) (S: structure number I, II, III, and IV; PX: traffic scheme A, B, C, and D).

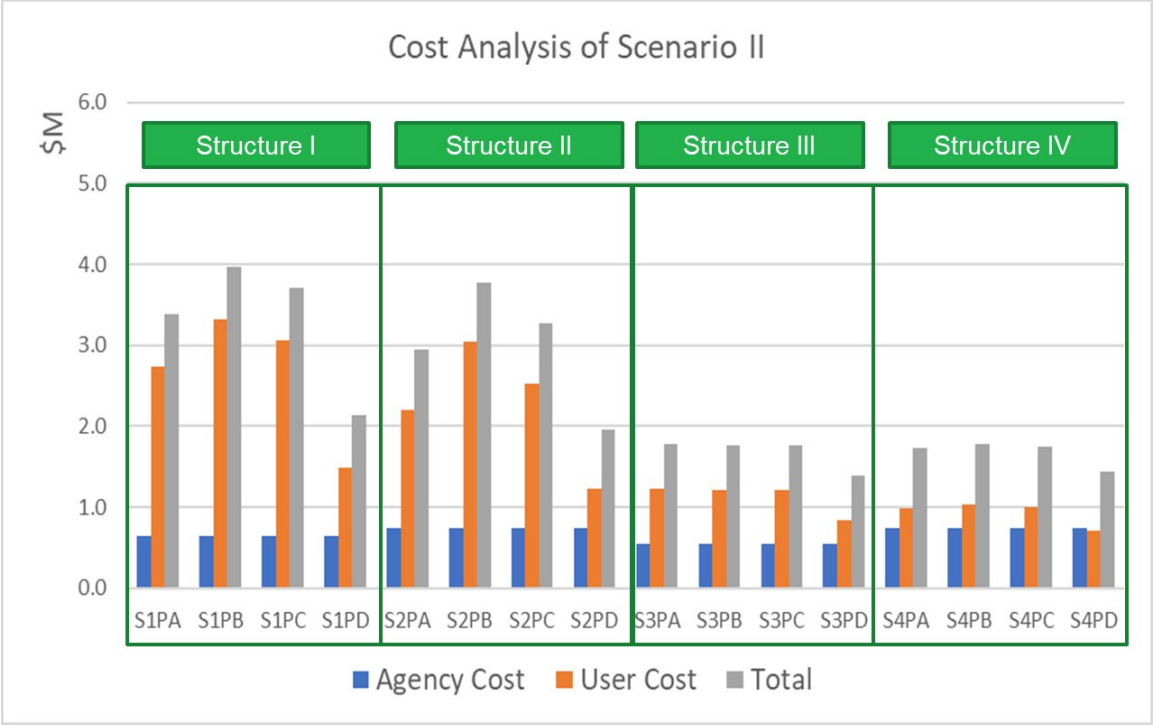

Figure 65. Graph. LCCA of four pavement structures under four platoon schemes (scenario II) (S: structure number I, II, III, and IV; PX: traffic scheme A, B, C, and D).

In scenario III, the major difference is wheelpath repair, which was applied instead of cold milling and HMA overlay for platoon scheme A. The pavement performance after these two maintenance treatments were considered the same. Thus, only the agency cost of scenario III is presented in Figure 69. Channelized traffic can be mitigated by wheelpath repair and reduce the agency cost by 15% compared with cold milling and HMA overlay.

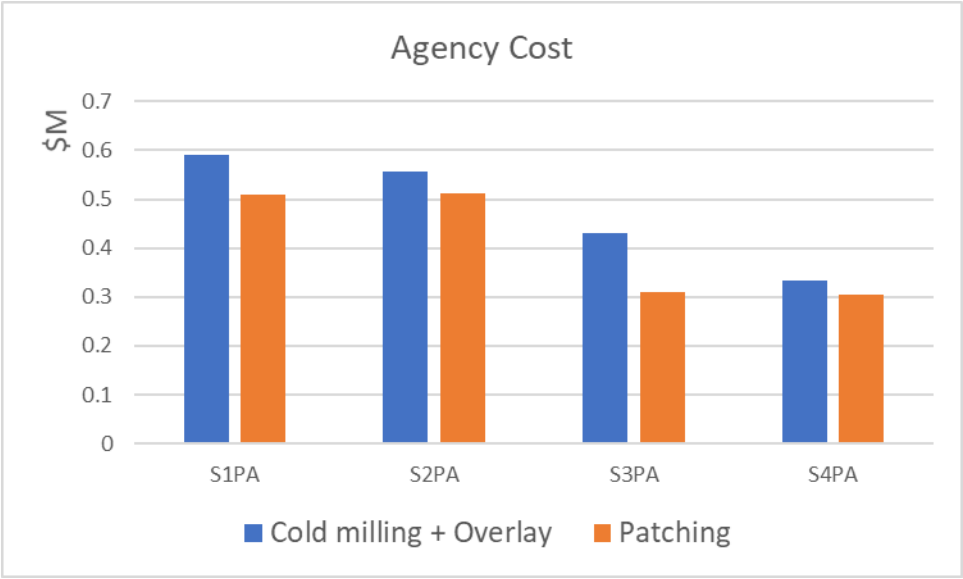

Figure 66. Graph. Agency cost in scenario III.

LIFE CYCLE ASSESSMENT

Life cycle assessment is a widely used approach to analyze and quantify environmental impact flows throughout the life cycle of products and systems. A product's life cycle begins with raw material acquisition and moves through production, use, end-of-life recycling, and final disposal. Life cycle assessment is used to identify the significance of environmental impacts and potential environmental impacts through four phases: goal and scope definition, life cycle inventory analysis, impact assessment, and interpretation. The goal of this sub-section of the study was to quantify the environmental impacts and energy consumption of four types of asphalt pavement structures under four truck platooning schemes. The scope of this sub-section is explained in Table 26.

Table 26. Scope of Life Cycle Assessment

Geography	United States
System boundary	This sub-section considers the material usage in the materials stage, the energy inputs in the construction stage, the treatments applied within the maintenance stage, as well as the fuel savings of truck platoons and additional fuel consumption due to pavement roughness in the use stage.
Functional Unit	Lane-mile section
Analysis period	45 years
Data assumptions	The study uses a combination of primary and secondary data from various sources, including local surveys, governmental reports and databases, industry reports, peer-reviewed papers, and commercial inventory databases.
Impact categorization	This study uses the US Environmental Protection Agency's (EPA) Tool for Reduction and Assessment of Chemicals and Other Environmental Impacts (TRACI 2.1). Four quantitative outcomes from the LCA study were analyzed: global warming potential (GWP), total energy, total energy with feedstock, and single score (SS). Single score represents a weighted score of 10 TRACI environmental impact categories and the weighting factors determined by the National Institute of Standards and Technology is specific to the United States (Bare et al., 2006).

Material and Construction Stage

In this study, pay items were used to quantity material and construction stage impacts. Material extraction and production impacts of each pay item are the summation of the quantity of each type of material included in the pay item multiplied by its unit impact (Figure 70).

$$E_{PItem_j\_mat_i} = unit\ process\ E_{mat\ i} * Q_{PItem_j\_mat_i}$$

Figure 67. Equation. Energy consumption/environmental impacts of material *i* in pay item *j*.

where:

- E_{mat_i} is the energy consumption (EC)/environmental impacts (EI) of a unit of material *i*.
- $Q_{PItem_j\_mat_i}$ is the quantity of material *i* included in pay item *j*.

- $E_{PItem_{j\_mat_i}}$ is the EC /EI of material *i* in pay item *j*.

If mix design is considered, then the EC/EI of mixture *k* in pay item *j* are $E_{PItem_{j\_mix_k}}$, and it is calculated using the equation presented in Figure 71.

$$E_{PItem_{j\_mix_k}} = \sum_{i=1}^{m} E_{PItem_{j\_mixmat_i}} * Q_{PItem_{j\_mix_{k\_mat_i}}}$$

Figure 68. Equation. Energy consumption/environmental impacts of mixture *k* in pay item *j*.

where:

- $E_{PItem_{j\_mixmat_i}}$ is the EC/EI of material *i* used in mixture *k*.
- *m* is the total number of material types used in mixture *k*.
- $Q_{PItem_{j\_mix_{k\_}mat_i}}$ is the quantity of material *i* used in mixture *k* of pay item *j*.

The impacts of construction processes are described in the equation presented in Figure 72:

$$E_{PItem_{i\_Constr_j}} = \sum_j E_{Unit\_Constr_j} * \frac{Fuel\ Efficiency_j}{Equipment\ Speed_i} * Passes_j$$

Figure 69. Equation. Energy consumption/environmental impacts of construction process in pay item *j*.

where:

- $E_{Unit\_Constr_j}$ is the unit impacts/energy consumption of using equipment *j* in pay item *i*.
- $Fuel\ Efficiency_j$ is the fuel efficiency of equipment *j*.
- $Equipment\ Speed_i$ is the speed of equipment *j*.
- $Passes_j$ is the number of passes of equipment *j*.

As shown in Figure 60, the mixture design of SMA was assumed to be 7% asphalt binder and 4% air voids, with a maximum specific gravity of 2.53 $\mathrm{g/cm^3}$. The mixture designs of the binder and base courses were assumed to be the same: 5% asphalt binder, 4% air voids, and a maximum specific gravity of 2.53 $\mathrm{g/cm^3}$. Table 27 presents the energy consumption and GWP impacts of materials and construction stages.

Table 27. Energy Consumption and GWP of Material and Construction Stages

Scenario I	Structure I	Structure II	Structure III	Structure IV
Material stage: Energy (J)	5.89E+06	5.97E+06	3.16E+06	3.75E+06
Material stage: GWP (kg CO2 eq)	2.39E+05	2.46E+05	1.09E+05	1.20E+05
Construction stage: Energy (J)	1.90E+05	1.90E+05	8.72E+04	8.72E+04
Construction stage: GWP (kg CO2 eq)	1.38E+04	1.38E+04	6.54E+03	6.54E+03

Maintenance Stage

As presented in Table 20, the maintenance activities of scenario I were applied when fatigue cracking, rutting, or IRI reached the thresholds. Thus, Table 28 presents the environmental impacts and energy consumption of each structure under each platoon scheme. For scenario II, the same maintenance schedule was applied for each structure and under each platoon scheme. Thus, the energy consumption and environmental impacts were the same for each structure and each platoon scheme in scenario II (see Table 29).

Table 28. Energy Consumption and GWP of Maintenance Stage in Scenario I

	Platoon Scheme	Structure I	Structure II	Structure III	Structure IV
Maintenance stage: Energy (J)	A	3.42E+06	2.28E+06	4.56E+06	1.14E+06
	B	1.14E+06	1.14E+06	2.28E+06	0.00E+00
	C	2.28E+06	1.14E+06	3.42E+06	1.14E+06
	D	0.00E+00	0.00E+00	0.00E+00	0.00E+00
Maintenance stage: GWP (kg CO2 eq)	A	2.22E+05	1.48E+05	2.96E+05	7.40E+04
	B	7.40E+04	7.40E+04	1.48E+05	0.00E+00
	C	1.48E+05	7.40E+04	2.22E+05	7.40E+04
	D	0.00E+00	0.00E+00	0.00E+00	0.00E+00

Table 29. Energy Consumption and GWP of Maintenance Stage in Scenario II

	Platoon Scheme	Structure I/II/III/IV
Maintenance stage: Energy (J)	A/B/C/D	4.56E+06
Maintenance stage: GWP (kg CO2 eq)	A/B/C/D	2.96E+05

Use Stage

Similar to the user costs computation, two major components are considered in the LCA use stage: energy savings resulting from truck platooning design and additional fuel consumption due to pavement roughness. Given the equations from Figure 64, Figure 65, and Figure 66, the monetary results can be converted to gallons of fuel and then used to compute the energy and GWP. Table 30 and Table 31 present the use stage under scenario I and scenario II, respectively.

Table 30. Energy Consumption and GWP of Use Stage in Scenario I

	Structure I	Structure II	Structure III	Structure IV
Extra Energy Consumption due to Roughness (J)				
Platoon Scheme A	2.34E+07	2.38E+07	7.01E+06	7.17E+06
Platoon Scheme B	2.27E+07	2.30E+07	6.31E+06	7.07E+06
Platoon Scheme C	2.31E+07	2.25E+07	6.01E+06	5.86E+06
Platoon Scheme D	2.41E+07	2.40E+07	7.07E+06	6.21E+06
Energy Savings (J)	7.20E+06	7.20E+06	1.42E+05	1.42E+05
Extra GWP due to Roughness (kg CO2 eq)				
Platoon Scheme A	1.84E+06	1.87E+06	5.52E+05	5.63E+05
Platoon Scheme B	1.78E+06	1.81E+06	4.96E+05	5.56E+05
Platoon Scheme C	1.82E+06	1.77E+06	4.73E+05	4.61E+05
Platoon Scheme D	1.89E+06	1.88E+06	5.56E+05	4.89E+05
GWP savings (kg CO2 eq)	5.66E+04	5.66E+04	1.09E+04	1.09E+04

Table 31. Energy Consumption and GWP of Use Stage in Scenario II

	Structure I	Structure II	Structure III	Structure IV
Extra Energy Consumption due to Roughness (J)				
Platoon Scheme A	2.06E+07	1.79E+07	6.99E+06	5.82E+06
Platoon Scheme B	1.67E+07	1.52E+07	6.09E+06	5.19E+06
Platoon Scheme C	1.88E+07	1.61E+07	6.54E+06	5.46E+06
Platoon Scheme D	1.43E+07	1.30E+07	5.11E+06	4.39E+06
Energy Savings (J)	1.04E+06	1.04E+06	2.06E+05	2.06E+05
Extra GWP due to Roughness (kg CO2 eq)				
Platoon Scheme A	1.62E+06	1.41E+06	5.49E+05	4.58E+05
Platoon Scheme B	1.31E+06	1.20E+06	4.79E+05	4.09E+05
Platoon Scheme C	1.48E+06	1.27E+06	5.14E+05	4.30E+05
Platoon Scheme D	1.13E+06	1.02E+06	4.01E+05	3.45E+05
GWP savings (kg CO2 eq)	9.23E+04	9.23E+04	1.85E+04	1.85E+04

Life Cycle Assessment Results

The final LCA results for each structure under each platoon scheme were computed by summing up all the results in each stage and subtracting the fuel savings due to platoon operation. Figure 73 and Figure 74 present the LCA results of scenario I and II, respectively.

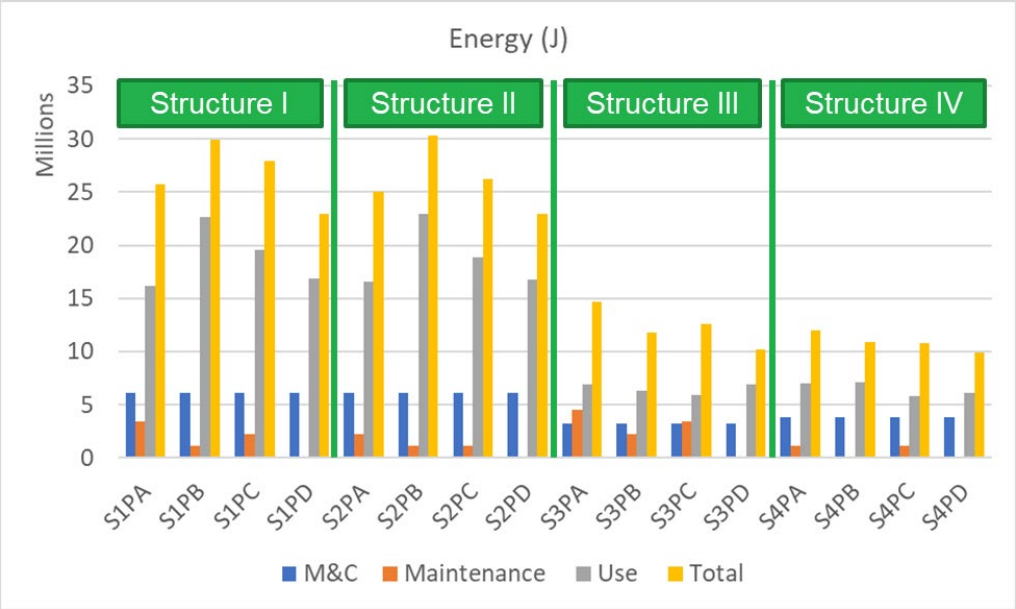

A. Energy consumption of scenario I

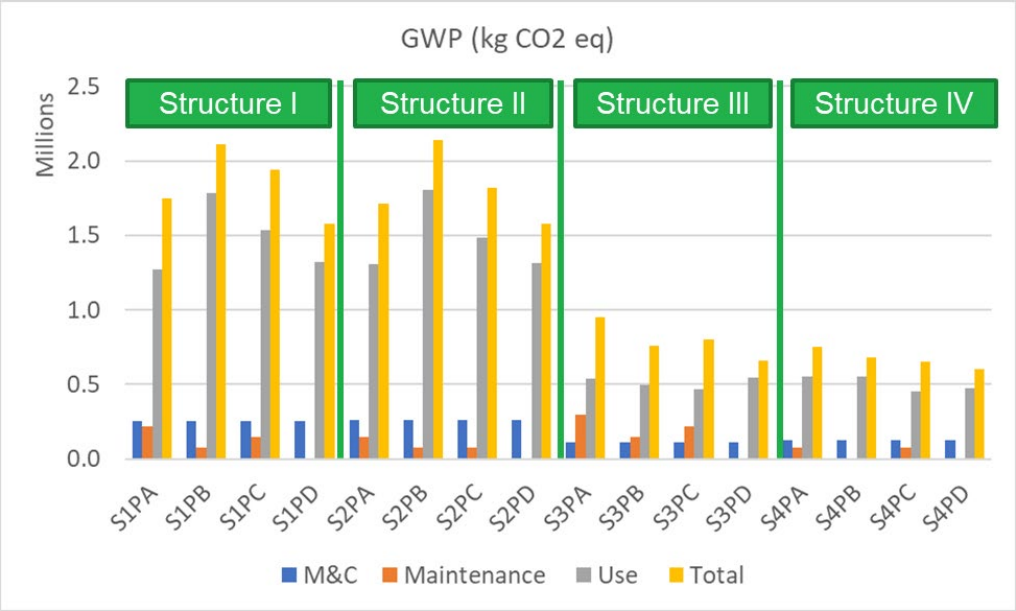

B. GWP of scenario I

Figure 70. Graph. LCA results of scenario I
(S: structure number I, II, III, and IV; PX: traffic scheme A, B, C, and D).

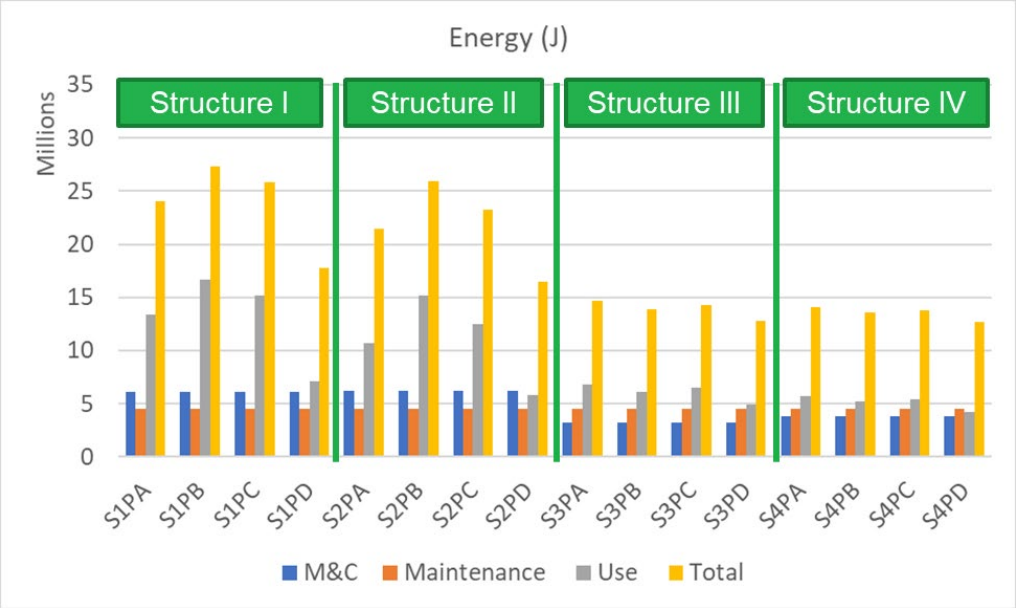

A. Energy consumption of scenario II

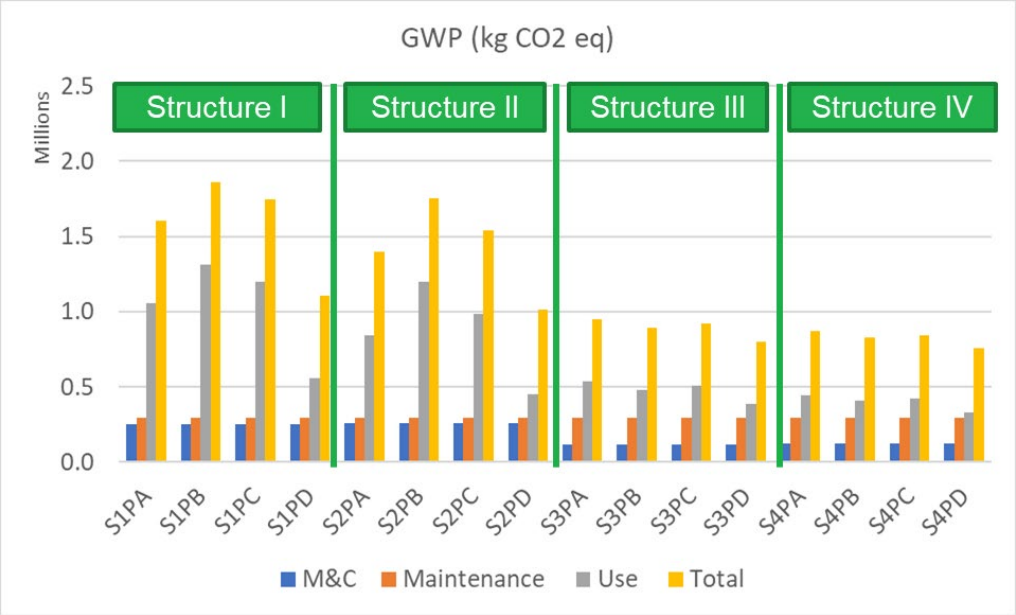

B. GWP of scenario II

Figure 71. Graph. LCA results of scenario II
(S: structure number I, II, III, and IV; PX: traffic scheme A, B, C, and D).

The results of scenarios I and II demonstrated that the platoon traffic always consumes less fuel and produced less emissions, which impacted the use stage. The energy consumption of platoon trucks in structures I and II can save up to 36% compared to human-driven trucks, and the emissions could be reduced by 40%. Because the use stage impacts are dominated by traffic volume, the benefits for structures III and IV were much smaller compared to structures I and II.

As mentioned above, the assumption was made that the performance of wheelpath repair and cold milling and HMA overlay were the same. Thus, scenario III only focused on the benefits of wheelpath repair in the maintenance stage, and new maintenance activity could reduce environmental impacts and energy consumption by 34% and 42%, respectively (Figure 75).

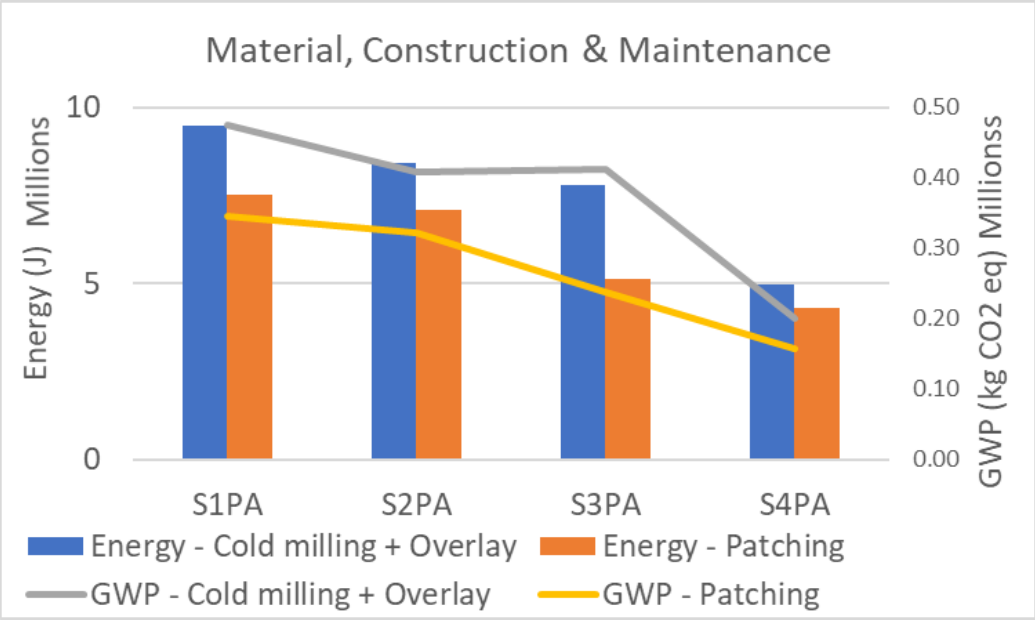

Figure 72. Graph. The benefits of applying wheelpath repair.

CHAPTER 6: SUMMARY AND CONCLUSION

Truck platoons have the potential to improve safety and reduce fuel consumption between 5% and 15%, based on platoon configuration. In Illinois, trucks carry more than 50% of freight tonnage and constitute 25% of the traffic on interstates. Therefore, expected fuel savings would be significant for the trucking industry. Deployment of truck platoons within interstate highways may have a direct effect on flexible pavement performance because of reduced truck spacing and trucks' channelized position. This could lead to decreased pavement service life and increased maintenance and rehabilitation costs as well as have corresponding environmental impacts.

An FE model was utilized for thin and thick pavement structures that incorporated complex characteristics, including HMA as a linear viscoelastic material, nonuniform 3D tire-contact stresses, layer-interface friction, moving load, and implicit dynamic analysis. A tandem axle with 4.5 ft spacing (the standard tandem-axle spacing for class 9 trucks) was applied in the FE model at a loading of 34 kips. To assess the effect of rest period on pavement responses, a database was created containing 180 and 24 cases for single and tandem axles, respectively.

In general, the maximum value of pavement responses was higher for tandem axles than single axles. Axle interaction was not manifested in the HMA layer, including longitudinal strain at the bottom of the HMA, and vertical compression and shear strains in the HMA layer. These strains recovered immediately after load application. The transverse strain at the bottom of the HMA, however, was found to be critical because of relatively slow recovery compared to other strains. In addition, the recovery of the single axle was greater than that of the tandem axle. To understand the impact of rest period, an exponential function was fitted for the recovery strain. The transverse strain recovers almost fully for spacing greater than 5 ft. Similarly, for rutting, the vertical compressive strain recovered fully for all layers in the pavement. In addition, because of the tandem axle's interaction, the impact on the subgrade was significant, followed by that of the granular base at approximately 1.4 times that of the single axle's response. Therefore, the results of the FE model indicate that rest period does not impact rutting and fatigue cracking in the HMA.

To calculate the impact of lateral position of platoon trucks, an expected response methodology was introduced. This methodology considers lane position of a vehicle as a random variable. Human-driven trucks were assumed to follow a normal distribution, with the mean location at the lane center and a standard deviation of 10 in. Autonomous trucks were assumed to follow a uniform distribution with variable start and end points, which created sub-lanes within the lane. Therefore, the lateral position of all trucks, human-driven or autonomous, could be described as a mixed probability density function. Using this probability density function, the expectation of pavement responses was calculated by integrating deterministic response profiles over probabilistic load locations. Finally, pavement damage was computed using expected responses and damage transfer functions. Because the percentage of autonomous vehicles and their position on the lane could be direct inputs, pavement damage could be calculated at any level of autonomous truck penetration and at any load location.

Distributing the traffic across the lane is a good policy for reducing pavement damage. To optimize the impact on pavement response, a genetic algorithm was used to determine the optimum CAT sub-lane positions. The optimal traffic pattern decreased pavement damage by up to 60% for fatigue and 33% for rutting. Three sub-lanes reduced pavement damage just as effectively as five and seven sub-lanes. When autonomous traffic is distributed across the lane, pavement damage could be reduced significantly. Channelized traffic could increase rutting and cracking by 38% and 212%, respectively, when compared to optimized platoons. These increases could be affected by truck load and speed, number of trucks in the platoon, pavement structure, or environment conditions.

Finally, based on the LCCA and LCA results of four structures (two for thick pavements and two for thin pavements) under four platoon schemes (all channelized platoons, all human-driven trucks, mix of platooning and human-driven vehicles, and optimized platoons), optimally distributed truck platooning was found to significantly reduce life cycle impacts. Compared to human-driven traffic, optimally distributed platooning could reduce life cycle cost, energy consumption, and emissions by 46%, 36%, and 42%, respectively, for the case studies. The reduction is a result of reduced air drag of platoon trucks and optimized pavement damage. However, these benefits can only be achieved when coupled with optimized maintenance timing. The maintenance schedule design can greatly impact the total cost and total impacts. Applying frequent maintenance activities can significantly reduce LCCA user costs and LCA use stage impacts, but it can also increase agency costs. This trade-off is more prominent for high-volume roads because of high user costs. Channelized traffic is not recommended as a platooning configuration, as it induces accelerated pavement damage.

Truck platoons reduce the life cycle costs and environmental impacts when combined with a predetermined distributed lane position for the trucks and regular maintenance scheduling. Optimized lane position could reduce pavement damage by up to 60% and corresponding timely maintenance could reduce the life cycle costs and environmental impacts by 48% and 26%, respectively. It is recommended that an optimized lane position strategy be implemented on pavement sections prior to allowing truck platoons.

Given that truck platoons are expected to be only connected in the first phase, no actions are required by the agency. However, in the second phase when truck platoons are expected to also be autonomous, a protocol for driving trends should be established per the recommendation of this study.

RECOMMENDATIONS FOR FUTURE WORK

Platooning implementation is dependent on many factors such as autonomous vehicle safety, public acceptance, policy decisions, and additional capital needed to upgrade the infrastructure network. Based on the findings of this project, platoonable sections and minimum spacing between autonomous trucks could be analyzed for safety by running traffic simulations on selected corridors. Protocols on connecting with platoons to implement optimized driving pattern is needed. The long-term impact of connectivity should be investigated and connected to pavement data collection and rehabilitation strategies.

REFERENCES

Aksnes, J. (2002). *A study of load responses towards the pavement edge*. Norwegian University of Science and Technology.

Al-Qadi, I. L., Gungor, O. E., She, R., & Yanfeng, O. (2020). *Optimization of lateral position of autonomous trucks* (Report No. CCAT-ICT-20-009). Illinois Center for Transportation. https://doi.org/10.36501/0197-9191/20-009

Al-Qadi, I. L., Loulizi, A., Elseifi, M., & Lahouar, S. (2004). The Virginia Smart Road: The impact of pavement instrumentation on understanding pavement performance. *Journal of the Association of Asphalt Paving Technologists*, *73*(3), 427–465.

Al-Qadi, I. L., & Nassar, W. N. (2003). Fatigue shift factors to predict HMA performance. *International Journal of Pavement Engineering*, *4*(2), 69–76. https://doi.org/10.1080/10298430310001593254

Al-Qadi, I. L., Okte, E., Ramakrishnan, A., Zhou, Q., & Sayeh, W. (2021). *Truck-platoonable pavement sections in Illinois' network* (Report No. FHWA-ICT-21-002). Illinois Center for Transportation. https://doi.org/10.36501/0197-9191/21-002

Al-Qadi, I. L., & Yoo, P.J. (2007). Effect of surface tangential contact stresses on flexible pavement response (with discussion). *Journal of the Association of Asphalt Paving Technologists*, *76(8):* 663–92.

American Association of State Highway and Transportation Officials. (2020). *Mechanistic-empirical pavement design guide: A manual of practice*, 3rd ed. AASHTO.

Attoh-Okine, N. O. (1994). Predicting roughness progression in flexible pavements using artificial neural networks. In *Transportation Research Board Conference Proceedings*, 1(1).

Bare, J., Gloria, T., & Norris, G. (2006). Development of the method and U.S. normalization database for life cycle impact assessment and sustainability metrics. *Environmental Science and Technology*, *40*(16): 5108–5115. https://doi.org/10.1021/es052494b

Beranek, S., & Carpenter, S. H. (2009). *Fatigue failure testing in section F* (Report No. ICT-09-058). Illinois Center for Transportation.

Bureau of Transportation Statistics. (2020). *Transportation statistics annual report April 2020 North American Freight Numbers*. US Department of Transportation.

Campbell, S., & Tawil, N. (2019). *Federal Investment, 1962 to 2018*. Congressional Budget Office.

Chong, E. K., & Zak, S. H. (2004). *An introduction to optimization*. John Wiley & Sons.

Chottani, A., Hastings, G., Murnane, J., & Neuhaus, F. (2018). *Distraction or disruption? Autonomous trucks gain ground in US logistics*. McKinsey & Company Report.

Costello, B., & Suarez, R. (2019). *Truck driver shortage analysis 2019*. The American Trucking Associations.

Daniel, J. S., & Kim, Y. R. (2001). Laboratory evaluation of fatigue damage and healing of asphalt mixtures. *Journal of Materials in Civil Engineering*, *13*(6), 434–440. https://doi.org/10.1061/(ASCE)0899-1561(2001)13:6(434)

Elseifi, M. A., Al-Qadi I. L., & Yoo P. J. (2006). Viscoelastic modeling and field validation of flexible pavements. *Journal of Engineering Mechanics*, *132*(2), 172–78.

Garcia, G., & Thompson, M. (2008). Strain and pulse duration considerations for extended-life hot-mix asphalt pavement design. *Transportation Research Record*, *2087*(1): 3–11. https://doi.org/10.3141%2F2087-01

Gungor, O. E., & Al-Qadi, I. L. (2020). Wander 2D: A flexible pavement design framework for autonomous and connected trucks. *International Journal of Pavement Engineering*, 1–16. https://doi.org/10.1080/10298436.2020.1735636

Gungor, O. E., She, R., Al-Qadi, I. L., & Ouyang, Y. (2019). Optimization of lateral position of autonomous trucks (OPLAT). Presentation at the Transportation Research Board 98th Annual Meeting, Washington, DC, January 13–17, 2019.

Gungor, O. E., She, R., Al-Qadi, I. L., & Ouyang, Y. (2020). One for all: Decentralized optimization of lateral position of autonomous trucks in a platoon to improve roadway infrastructure sustainability. *Transportation Research Part C: Emerging Technologies*, *120*, 102783. https://doi.org/10.1016/j.trc.2020.102783

Hernandez, J. A., Gamez, A., & Al-Qadi, I. L. (2016). Effect of wide-base tires on nationwide flexible pavement systems: Numerical modeling. *Transportation Research Record*, *2590*(1), 104–112. https://doi.org/10.3141%2F2590-12

Hochreiter, S., & Schmidhuber, J. (1997). Long short-term memory. *Neural computation*, *9*(8).

Illinois Department of Transportation (IDOT). (2018). *FY 2019–2024 proposed highway improvement program* [Technical Report]. Illinois Department of Transportation.

Kim, D., & Kim, Y. R. (2017). Development of stress sweep rutting (SSR) test for permanent deformation characterization of asphalt mixture. *Construction and Building Materials*, *154*, 373–383. https://doi.org/10.1016/j.conbuildmat.2017.07.172

Mansourkhaki, A., Sarkar, A., & Ameri, M. (2015). Impact of different loading patterns with short duration on the permanent strain of asphalt mixture. *Journal of Testing and Evaluation*, *43*(4), 853–866. https://doi.org/10.1520/JTE20130222

McAuliffe, B., Lammert, M., Lu, X. Y., Shladover, S., Surcel, M. D., & Kailas, A. (2018). Influences on energy savings of heavy trucks using cooperative adaptive cruise control. *SAE Technical Paper*, 2018-01-1181. https://doi.org/10.4271/2018-01-1181

Motevalizadeh, S. M., Ayar, P., Motevalizadeh, S. H., Yeganeh, S., & Ameri, M. (2018). Investigating the impact of different loading patterns on the permanent deformation behaviour in hot mix asphalt. *Construction and Building Materials*, *167*, 707–715. https://doi.org/10.1016/j.conbuildmat.2018.02.049

National Cooperative Highway Research Program (NCHRP). (2004). *Guide for mechanistic–empirical design of new and rehabilitated pavement structures* (Final Report). NCHRP Project 1-37A.

Nejad, F. M., Sorkhabi, H., & Karimi, M. M. (2016). Experimental investigation of rest time effect on permanent deformation of asphalt concrete. *Journal of Materials in Civil Engineering*, *28*(5),

06015016. https://doi.org/10.1061/(ASCE)MT.1943-5533.0001498

Newland, D. E. (2012). *An introduction to random vibrations, spectral & wavelet analysis*. Courier Corporation.

Noorvand, H., Karnati, G., & Underwood, B. S. (2017). Autonomous vehicles: Assessment of the implications of truck positioning on flexible pavement performance and design. *Transportation Research Record*, *2640*(1), 21–28. https://doi.org/10.3141%2F2640-03

Odoki, J. B., & Kerali, H. G. R. (2000). *HDM-4 analytical framework and model descriptions*. World Bank Association.

Okte, E., Al-Qadi, I. L., & Ozer H. (2019). Effects of pavement condition on LCCA user costs. *Transportation Research Record*, *2673*(5): 339–50. https://doi.org/10.1177%2F0361198119836776

Ozbay, K., & Laub, R. (2001). *Models for pavement deterioration using LTPP* (Report No. FHWA-NJ-1999-030). New Jersey Department of Transportation.

Romanoschi, S. A., & Metcalf, J. B. (2001). Effects of interface condition and horizontal wheel loads on the life of flexible pavement structures. *Transportation Research Record*, *1778*(1), 123–131.

Shen, S., Lu, X., Zhang, Y., & Lytton, R. (2013). Fracture and viscoelastic properties of asphalt binders during fatigue and rest periods. *Journal of Testing and Evaluation*, *42*(1), 109–117. https://doi.org/10.1520/JTE20130030

Siddharthan, R. V., Nasimifar, M., Tan, X., & Hajj, E. Y. (2017). Investigation of impact of wheel wander on pavement performance. *Road Materials and Pavement Design*, *18*(2), 390–407. https://doi.org/10.1080/14680629.2016.1162730

Stephenson, S. (2016). Automotive applications of high precision GNSS (Doctoral dissertation, University of Nottingham).

Underwood, B. S., & Zeiada, W. A. (2014). Characterization of microdamage healing in asphalt concrete with a smeared continuum damage approach. *Transportation Research Record*, *2447*(1), 126–135. https://doi.org/10.3141%2F2447-14

US Department of Transportation (USDOT). (2002). *Life-cycle cost analysis primer*. US Department of Transportation. https://www.fhwa.dot.gov/asset/lcca/010621.pdf.

US Department of Transportation (USDOT). (2013). *Pavement remaining service interval implementation guidelines* (Report No. FHWA-HRT-13-050). AMEC Environment and Infrastructure, Inc. https://www.fhwa.dot.gov/publications/research/infrastructure/pavements/13050/13050.pdf.

Wang, H., & Al-Qadi, I. L. (2009). Combined effect of moving wheel loading and three-dimensional contact stresses on perpetual pavement responses. *Transportation Research Record*, *2095*(1), 53–61.

Whitley, D. (1994). A genetic algorithm tutorial. *Statistics and Computing*, *4*(2), 65–85.

Wong, K., Javanmardi, E., Javanmardi, M., & Kamijo, S. (2019). Estimating autonomous vehicle localization error using 2D geographic information. *ISPRS International Journal of Geo-Information*, *8*(6), 288.

Wu, R., & Harvey, J. T. (2008, February). Evaluation of the effect of wander on rutting performance in HVS tests. In *Proceedings of the 3rd International Conference on Accelerated Pavement Testing*.

Yoo, P. J., & Al-Qadi, I. L. (2007). Effect of transient dynamic loading on flexible pavements. *Transportation Research Record*, *1990*(1), 129–140. https://doi.org/10.3141%2F1990-15

Yoo, P., Al-Qadi I. L., Elseifi, M., & Janajreh I. (2006). Flexible pavement responses to different loading amplitudes considering layer interface condition and lateral shear forces. *International Journal of Pavement Engineering*, *7*(1), 73–86.

Zabat, M., Stabile, N., Farascaroli, S., & Browand, F. (1995). *The aerodynamic performance of platoons: A final report* (Report No. UCB-ITS-PRR-95-35). California PATH Program, Institute of Transportation Studies.

Zeiada, W. A., Gudipudi, P. P., Underwood, B. S., & Souliman, M. I. (2018). Effect of loading waveform pattern and rest period on fatigue life of asphalt concrete using viscoelastic continuum damage model. *Transportation Research Record*, *2672*(28), 451–461. https://doi.org/10.1177%2F0361198118773892

Zhang, L., Chen, F., Ma, X., & Pan, X. (2020). Fuel economy in truck platooning: A literature overview and directions for future research. *Journal of Advanced Transportation*, 2604012. https://doi.org/10.1155/2020/2604012

Zhou, F., Hu, S., Chrysler, S. T., Kim, Y., Damnjanovic, I., Talebpour, A., & Espejo, A. (2019). Optimization of lateral wandering of automated vehicles to reduce hydroplaning potential and to improve pavement life. *Transportation Research Record*, *2673*(11), 81–89. https://doi.org/10.1177%2F0361198119853560

Ziyadi, M., Ozer, H., Kang, S., & Al-Qadi, I. L. (2018). Vehicle energy consumption and an environmental impact calculation model for the transportation infrastructure systems. *Journal of Cleaner Production*, *174*, 424–436. https://doi.org/10.1016/j.jclepro.2017.10.292

APPENDIX

EXPECTED DAMAGE CALCULATION

Derivation of Expected Response Profile

The definition of the equation is given in Figure 76.

$$\mu_r(x) = E[f(x-s)] = \int_{-\infty}^{+\infty} f(x-s)g(s)ds$$

Figure 73. Equation. Derivation of expected response profile—part one.

Variables $f(x-s)$ and $g(s)$ can be placed in the equation as given in Figure 77.

$$\mu_r(x) = \int_{-\infty}^{+\infty} \sum_{i=0}^{n} \alpha_i \, exp\left(-i\left(\frac{x-s}{w_h\gamma}\right)^2\right)\left(\frac{p_n \exp\left(0.5\left(\frac{s}{\sigma}\right)^2\right)}{\sigma\sqrt{2\pi}} + \sum_{j=1}^{m} \frac{\mathrm{p_j} d_j}{s_u^j - s_l^j}\right) ds$$

Figure 74. Equation. Derivation of expected response profile—part two.

After distributing the first term inside the parentheses, the equation becomes what is presented in Figure 78.

$$\mu_r(x) = \int_{-\infty}^{+\infty} \sum_{i=0}^{n} \frac{\alpha_i p_n exp\left(-i\left(\frac{x-s}{w_h\gamma}\right)^2 + 0.5\left(\frac{s}{\sigma}\right)^2\right)}{\sigma\sqrt{2\pi}} + \sum_{i=0}^{n}\sum_{j=1}^{m} \frac{\alpha_i \mathrm{p_j} exp\left(-i\left(\frac{x-s}{w_h\gamma}\right)^2\right) d_j}{s_u^j - s_l^j} ds$$

Figure 75. Equation. Derivation of expected response profile—part three.

The integral can be moved into the summation as given in Figure 79.

$$\mu_r(x) = \sum_{i=0}^{n} \int_{-\infty}^{+\infty} \frac{\alpha_i p_n exp\left(-i\left(\frac{x-s}{w_h\gamma}\right)^2 + 0.5\left(\frac{s}{\sigma}\right)^2\right)}{\sigma\sqrt{2\pi}} ds + \sum_{i=0}^{n}\sum_{j=1}^{m} \int_{-\infty}^{+\infty} \frac{\alpha_i \mathrm{p_j} exp\left(-i\left(\frac{x-s}{w_h\gamma}\right)^2\right) d_j}{s_u^j - s_l^j} ds$$

Figure 76. Equation. Derivation of expected response profile—part four.

The integral can be computed as given in Figure 80. Please note that the terms where *i* = 0 require special attention.

$$\mu_r(x) = \sum_{i=0}^{n} \frac{\alpha_i p_n ex\,p\left(-\frac{ix^2}{2i\sigma^2 + w_h^2\gamma^2}\right)}{2\sqrt{2\sigma^2 + w_h^2\gamma^2}} \operatorname{erf}\left(\frac{2i\sigma^2(s-x) + w_h^2\gamma^2 s}{\sqrt{2}w_h^2\gamma^2\sigma\sqrt{2\sigma^2 + w_h^2\gamma^2}}\right)\Bigg|_{-\infty}^{+\infty} + \sum_{i=0}^{n}\sum_{j=1}^{m} \frac{\alpha_i p_j \sqrt{\pi} w_h^2\gamma^2}{2\sqrt{i}(s_u^j - s_l^j)} \operatorname{erf}\left(\frac{\sqrt{i}(s-x)}{w_h^2\gamma^2}\right)\Bigg|_{s_l^j}^{s_u^j}$$

Figure 77. Equation. Derivation of expected response profile—part five.

Terms where *i* = 0 can be taken out of the summation and simplified further, as given in Figure 81.

$$\mu_r(x) = \alpha_0 p_n + \sum_{i=1}^{n}\left[\frac{\alpha_i p_n ex\,p\left(-\frac{ix^2}{2i\sigma^2 + w_h^2\gamma^2}\right)}{\sqrt{2\sigma^2 + w_h^2\gamma^2}}\right] + \sum_{j=1}^{m}\left[\alpha_0 p_j + \sum_{i=1}^{n} \frac{\alpha_i p_j \sqrt{\pi} w_h^2\gamma^2}{2\sqrt{i}(s_u^j - s_l^j)}\left[\operatorname{erf}\left(\frac{\sqrt{i}(s_u^j - x)}{w_h^2\gamma^2}\right) - \operatorname{erf}\left(\frac{\sqrt{i}(s_l^j - x)}{w_h^2\gamma^2}\right)\right]\right]$$

Figure 78. Equation. Derivation of expected response profile—part six.

Finally, because p_n and sum of all p_j equals to 1, a_0 term can be left by itself, as given in Figure 82.

$$\mu_r(x) = \alpha_0 + \sum_{i=1}^{n}\left[\frac{\alpha_i p_n ex\,p\left(-\frac{ix^2}{2i\sigma^2 + w_h^2\gamma^2}\right)}{\sqrt{2\sigma^2 + w_h^2\gamma^2}}\right] + \sum_{j=1}^{m}\left[\sum_{i=1}^{n}\left[\frac{\alpha_i p_j \sqrt{\pi} w_h^2\gamma^2}{2\sqrt{i}(s_u^j - s_l^j)}\left[\operatorname{erf}\left(\frac{\sqrt{i}(s_u^j - x)}{w_h^2\gamma^2}\right) - \operatorname{erf}\left(\frac{\sqrt{i}(s_l^j - x)}{w_h^2\gamma^2}\right)\right]\right]\right]$$

Figure 79. Equation. Derivation of expected response profile—part seven.

HMA Fatigue Cracking Equations

The *C* coefficient is defined as given in Figure 83.

$$C = 10^M, M = 4.84\left(\frac{V_{be}}{V_{be} + V_a} - 0.69\right)$$

Figure 80. Equation. C coefficient expression.

Where V_{be} is the effective asphalt content by volume and V_a is the percentage of air voids in the mix. C_h term for top-down and bottom-up cracking is defined as given in Figure 84.

$$C_{H_{bot}} = \frac{1}{0.000398 + \frac{0.003602}{1 + \exp(11.02 - H_{HMA})}}, C_{H_{top}} = \frac{1}{0.01 + \frac{12}{1 + \exp(15.676 - 2.8286 * H_{HMA})}}$$

Figure 81. Equation. Type of cracking.

Where H_{HMA} is the thickness of the HMA layer in inches. Expressions for C_1^*, C_2^* are given in Figure 85.

$$C_1^* = -2, C_2^* = -2.480874 - 39.748(1 + H_{HMA})^{-2.856}$$

Figure 82. Equation. Coefficients for bottom-up and top-down cracking.

HMA Rutting Equations

For rutting, depth correction k_z is given in Figure 86.

$$k_z = (C_1 + C_2 D)0.328196^D$$

Figure 83. Equation. Depth correction coefficient.

Where D is the mid-depth of the sub-layer in inches. C_1, C_2 are defined as given in Figure 87.

$$C_1 = -0.1039(H_{HMA})^2 + 2.4868(H_{HMA}) - 17.342, C_2 = 0.0172(H_{HMA})^2 - 1.7331(H_{HMA}) + 27.428$$

Figure 84. Equation. Coefficients for depth correction.

Unbound Materials Rutting Equations

Parameter β can be defined as given in Figure 88.

$$log10(\beta) = -0.61119 - 0.017638W_c$$

Figure 85. Equation. β coefficient.

Where, W_c is the water content in percentage. Parameter ρ is defined as given in Figure 89.

$$\rho = 10^9 \left(\frac{C_o}{1 - 10^{9\beta}}\right)^{\frac{1}{\beta}}, C_o = \ln\left(\frac{a_1 M_r^{b_1}}{a_9 M_r^{b_9}}\right)$$

Figure 86. Equation. ρ parameter.

Where, M_r is the resilient modulus of unbound layer in psi, a_1, a_9, b_1, b_9 are 0.15,20,0,0 respectively. Finally, ϵ_0/ϵ_r is defined as given in Figure 90.

$$\frac{\epsilon_o}{\epsilon_r} = \frac{\exp(\rho^\beta)\, a_1 + \exp\left(\frac{\rho}{10^9}\right)^\beta a_9}{2}$$

Figure 87. Equation. e_o/ϵ_r parameter.


Illinois Department
of Transportation


ILLINOIS